ABSTRACT

Title of Document: ALD PROCESSES AND APPLICATIONS TO NANOSTRUCTURED ELECTROCHEMICAL ENERGY STORAGE DEVECES

Xinyi CHEN, Doctor of Philosophy, 2013

Directed By: Professor Gary W. Rubloff
Minta Martin Professor of Engineering,
Department of Materials Science and Engineering and the Institute for Systems Research

Next generation Li-ion batteries (LIB) are expected to display high power densities (i.e. high rate performance, or fast energy storage) while maintaining high energy densities and stable cycling performance. The key to fast energy storage is the efficient management of electron conduction, Li diffusion, and Li-ion migration in the electrode systems, which requires tailored material and structural engineering in nanometer scale. Atomic layer deposition (ALD) is a unique technique for nanostructure fabrications due to its precise thickness control, unprecedented conformality, and wide variety of available materials. This research aims at using ALD to fabricate materials, electrodes, and devices for fast electrochemical energy storage.

First, we performed a detailed study of ALD V_2O_5 as a high capacity cathode material, using vanadium tri-isopropoxide (VTOP) precursor with both O_3 and H_2O as oxidant. The new O_3-based process produces polycrystalline films with generally

higher storage capacity than the amorphous films resulting from the traditional H_2O-based process. We identified the crucial tradeoff between higher gravimetric capacity with thinner films and higher material mass with thicker films. For the thickness regime 10–120 nm, we chose areal energy and power density as a useful metric for this tradeoff and found that it is optimized at 60 nm for the O_3-VTOP ALD V_2O_5 films.

In order to increase material loading on fixed footprint area, we explored various 3-dimentional (3D) substrates. In the first example, we used multiwall carbon nanotube (MWCNT) sponge as scaffold and current collector. The core/shell MWCNT/V_2O_5 sponge delivers a stable high areal capacity of 816 μAh/cm^2 for 2 Li/V_2O_5 voltage range (4.0-2.1 V) at 1C rate (nC means charge/discharge in 1/n hour), 450 times that of a planar V_2O_5 thin film cathode. Due to low density of MWCNT and thin V_2O_5 layer, the sponge cathode also delivers high gravimetric power density in device level that shows 5X higher power density than commercial LIBs.

In the other example, Li-storage paper cathodes, functionalized of conductivity from CNT and Li-storage capability from V_2O_5, presented remarkably high rate performance due to the hierarchical porosity in paper for Li^+ migration. The specific capacity of V_2O_5 is as high as 410 mAh/g at 1C rate, and retained 116 mAh/g at high rate of 100C. We found V_2O_5 capacities decreased by about 30% at high rates of 5C-100C after blocking the mesopores in cellulose fiber, which serves to be the first confirmative evidence of the critical role of mesoporosity in paper fibers for high-rate electrochemical devices.

Finally, we made high density well-aligned nanoporous electrodes (2 billion/cm^2) using anodic alumina template (AAO). ALD materials were deposited into the nanopores sequentially – Ru or TiN for current collection, and V_2O_5 for Li-storage. Ru metal by ALD shows high conductivity and conformality, and serves best as the current collector for V_2O_5. The capacity of V_2O_5 reaches about 88% of its theoretic value at high rate of 50C. Such electrodes can be cycled for 1000 times with 78% capacity retention.

ALD PROCESSES AND APPLICATIONS TO NANOSTRUCTURED ELECTROCHEMICAL ENERGY STORAGE DEVECES

By

Xinyi CHEN

Dissertation submitted to the Faculty of the Graduate School of the
University of Maryland, College Park, in partial fulfillment
of the requirements for the degree of
Doctor of Philosophy
2013

Advisory Committee:
Professor Gary W. Rubloff, Chair
Professor Sang Bok Lee
Professor Chunsheng Wang
Professor Raymond Adomaitis
Professor Liangbing Hu

Dedication

To my grandmother
Guanglian Zhu (朱广莲)

Acknowledgements

I am sincerely thankful to my advisor, Prof. Gary Rubloff, for his support and guidance throughout my PHD career. Thanks for trusting me and encouraging me to explore collaboration opportunities and crazy ideas, some of which actually turned out successful. His enthusiasm and creativity for research and management have truly been inspiring to me.

I would like to acknowledge my colleagues for their support, discussions, and collaborations. To my group mates Laurent Lecordier, Parag Banerjee, Keith Gregorczyk, Marshall Schroeder, Alex Kozen, Yi Cheng, Jordon Bentz, Xiaolong Luo. Special thanks to Chanyuan Liu for carrying on a lot of experiments during my last semester. To Prof. Sangbok Lee and his group for their support and inspiring discussions over the years. To Prof. Liangbing Hu as my unofficial co-advisor for his continued encouragement and guidance. To Prof. Wangsheng Wang for providing glovebox for battery assembly. To Ekaterina Pomerantseva from Prof. Reza Ghodssi’s group for teaching me basic skills for electrochemical characterizations.

I would also like to give many thanks to my collaborators outside our group. To Prof. Anyuan Cao in Beijing University for providing high quality carbon nanotube sponges. To Xuan Liu and Prof. Stanislav Stoliarov for the collaboration in the ALD for fire protection project. To Iris Rauda and Prof. Sarah Tolbert from UCLA for the collaboration in the V_2O_5-porous ITO supercapacitor project.

I sincerely thank my family and my friends for their consistent support. Special thanks to my wife and my parents for supporting my research over the years and being patient with me. Last but not least, I thank my grandmother for her unconditional love. She passed away from a stomach cancer during my PHD years, which has been the biggest loss in my life. She didn’t receive any formal education, but taught me the most important lesson – love. This dissertation is in memory of the greatest grandmother – Mrs Guanglian Zhu.

This work has been supported by Nanostructures for Electrical Energy Storage (NEES), an Energy Frontier Research Center funded by the U.S. Department of Energy, Office of Science, Office of Basic Energy Sciences under Award Number DESC0001160. I would like to acknowledge the University of Maryland NanoCenter and give thanks to the NanoCenter Staff. None of this work would be possible without funding support from NSF’s support of the NispLab as a MRSEC Shared Experimental Facility.

Table of Contents

Chapter 1: Introduction

1.1 Background and motivation

1.1.1 Fast energy storage

With the increasing worldwide need for energy, fossil fuels as our main energy source are rapidly being running out, while their combustion is still bringing environmental problems such as greenhouse gases and other pollutants. Clean energy sources, including solar and wind, are very attractive principle alternatives. However, the use of either one has limitations from geographical and temporal distributions.[1] Therefore, energy storage is in great demand to support the extensive applications of the clean energy sources. Desired energy storage devices should simultaneously collect high power and energy densities while displaying stable cycling performance.[2, 3] In particular, high rate energy storage is in high demand in order to efficiently manage the imbalances between energy consumption and clean energy supply. Fast energy storage is also critical to the development of hybrid or electric vehicles that can switch the utilization of combustion engines. Li-ion batteries (LIB) now are the dominant type of electric energy storage devices for various consumer electronic applications. Their applications for transportation and smart grid are expected to boost in the coming decent if the storage rate can be significantly improved.[4]

1.1.2 Nanostructures for energy storage devices

Techniques with precise control of nano-sized materials have been maturing over the past twenty years, allowing one to grow structures of a precise thickness, size, and shape.[5] These same techniques have been adapted to make more complicated heterostructure nanomaterials and have recently been able to show significant improvement in energy storage. Figure 1 shows a Ragone plot of different electrical energy storage (EES) devices. This plot shows the fundamental limitations of traditional EES's. Due to differences in storage mechanisms of capacitors, which store energy as surface charge, and batteries, which store ionized species, we typically see a trade-off between high power density and high energy density. Also, we see that by using heterostructured nanomaterials, significant improvements can be

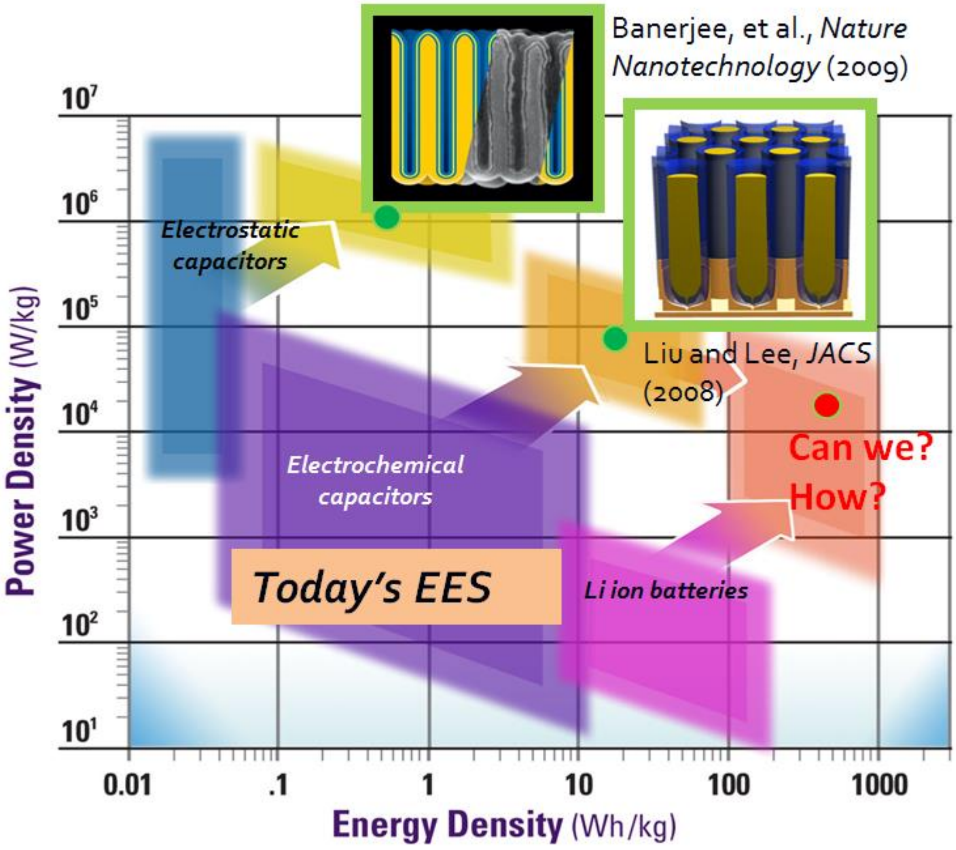

Figure 1. Ragone plot for electrochemical energy storage devices. Showing the energy and power density for traditional devices, and the dramatic improvements possible by using nanostructured materials.

made, as was shown by Banerjee et al for electrostatic capacitors,[6] and Liu and Lee for electrochemical capacitors.[7] Currently, it is the endeavor of many researchers to improve Li-ion batteries into higher power and energy region.

A conventional LIB cell consists of an anode (negative electrode, e.g., graphite), a cathode (positive electrode, e.g., $LiCoO_2$), an electronically insulating separator, and

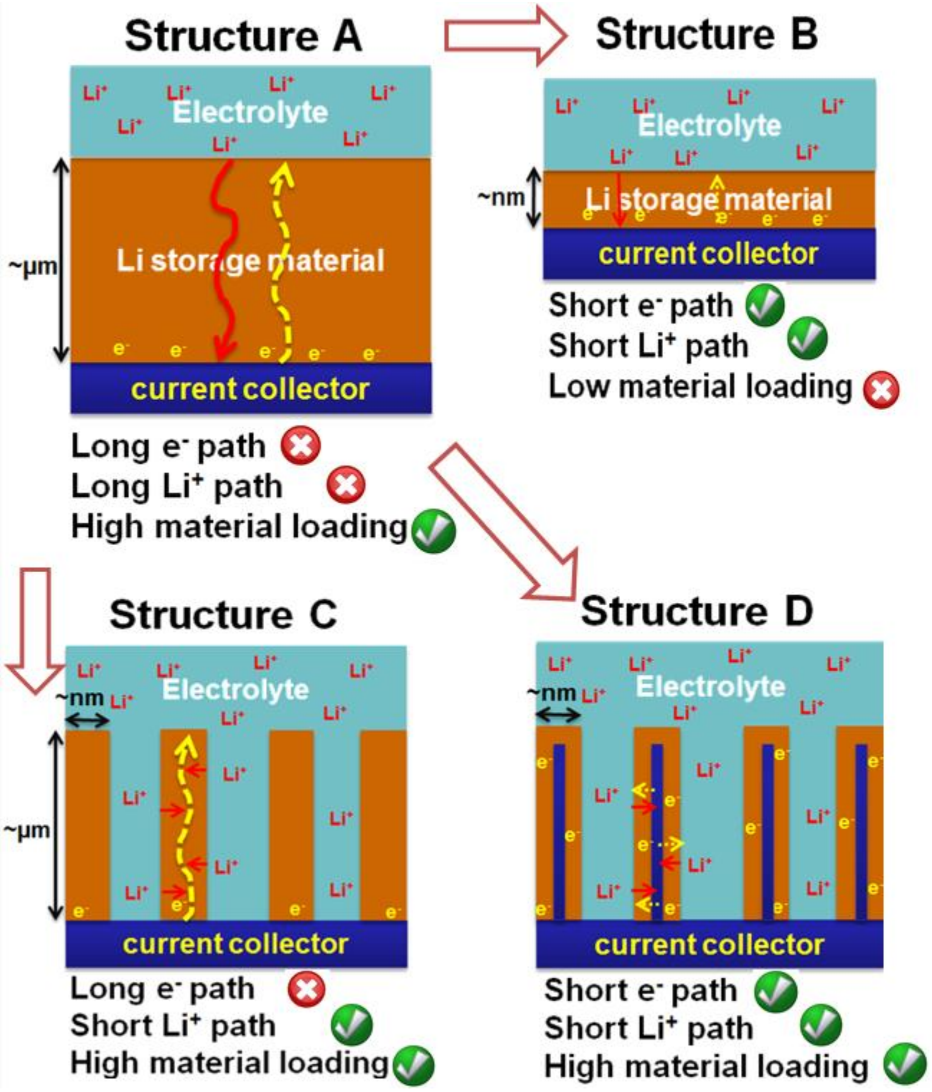

Figure 2. Schematics of four structures for electrochemical energy storage electrode.

an ionic conductive electrolyte to transfer lithium ions between the two electrodes. A major challenge for LIB to achieve high rates (power) is to overcome the long charge/discharge times caused by low Li diffusion coefficient in electrode materials. Kinetically, the diffusion time is proportional to the square of diffusion length. As illustrated by structure A and B in Figure 2, thin film electrodes (Fig. 2b), in contrast to thicker particle-based composite electrodes (Fig. 2a), provide a potential solution to achieve high power densities by reducing the thickness of active storage material layers, i.e. a reduction of thickness from 1 μm to 10 nm will reduce the diffusion time by four orders of magnitude.[8, 9] However, to achieve good performance of the total device, a reasonable amount of active material is required. Nanostructures built in three-dimensions (3D) will significantly increase the material loading on a fixed footprint, while maintaining the short Li diffusion length, as shown in structure C. In addition, electron transport could also be a limiting factor for high rate discharge/charge performance since electrochemical (de)/lithiation is accompanied with charge transfer with electrons. Structure D explores the thin active Li storage layer on nanostructured conductive scaffold for fast kinetics and the high material loading, thus making it most promising to achieve high power performance without sacrificing energy density.

To fabricate a nanostructure electrode like Structure D, it is important to have the capability to conformally coat active materials on 3D current collectors with desired thickness. Atomic layer deposition (ALD) is an attractive way to accurately deposit film thicknesses in typically 1-100 nm range with unprecedented capability for uniform and conformal deposition. It is a low temperature thin film growth technique by which sequentially pulsed precursors are exposed to a surface, leading to predictable monolayer growth with superb uniformity even over demanding topography, such as high-aspect ratio nanostructures.[10]

1.2 Atomic layer deposition (ALD)

1.2.1 Brief introduction to ALD

Atomic Layer Deposition (ALD), which was known as atomic layer epitaxy (ALE) before 2000, was developed as a method for depositing thin, defect-free, high-purity films.[11] It has become a key processing technique in the display and microelectronics industries where miniaturization has required precise atomic control of film thickness and conformal deposition.[12, 13] Unlike Chemical Vapor Deposition (CVD), where precursors react in the gas-phase simultaneously, ALD is a cyclic and self-limiting process based on sequential binary surface reactions.[14, 15] ALD can be used to coat a variety of substrate materials with typically amorphous films because it is a low temperature process.[16] Various recipes can be deposited consecutively since each precursor is introduced separately and many recipes have a wide deposition temperature window. Furthermore, this process is scalable, able to coat large and/or multiple substrates.[17] Figure 3 shows a generic schematic of an idealized ALD process. The process starts with a substrate with known surface groups, in this case –OH groups. Next, a metal-organic precursor ML_x (M represents metal ion and L represents organic ligand) is pulsed into the reaction chamber where it chemisorbs and reacts with the surface species producing by products that are then pumped away during inert gas purge step. The second precursor, in this case water, is then exposed to the substrate and reacts with the metal-organic precursor at the surface, again producing by-products that are pumped away in the next purge. Ideally after one complete cycle a single monolayer of the desired material, in this case M_xO_y, would have been deposited and the surface species will be the same as they were at the start, in this case the –OH species. Such ALD cycle repeats until desired film thickness is achieved.

The dose of each precursor is generally controlled by using timed ALD valves which allow a fixed amount of precursor, depending on the individual vapor pressures, into a reaction chamber. By varying the time of each pulse the dose of each precursor is effectively controlled. At some precursor dosage all available reaction sites have been used therefore further increases in dosage will not result in larger

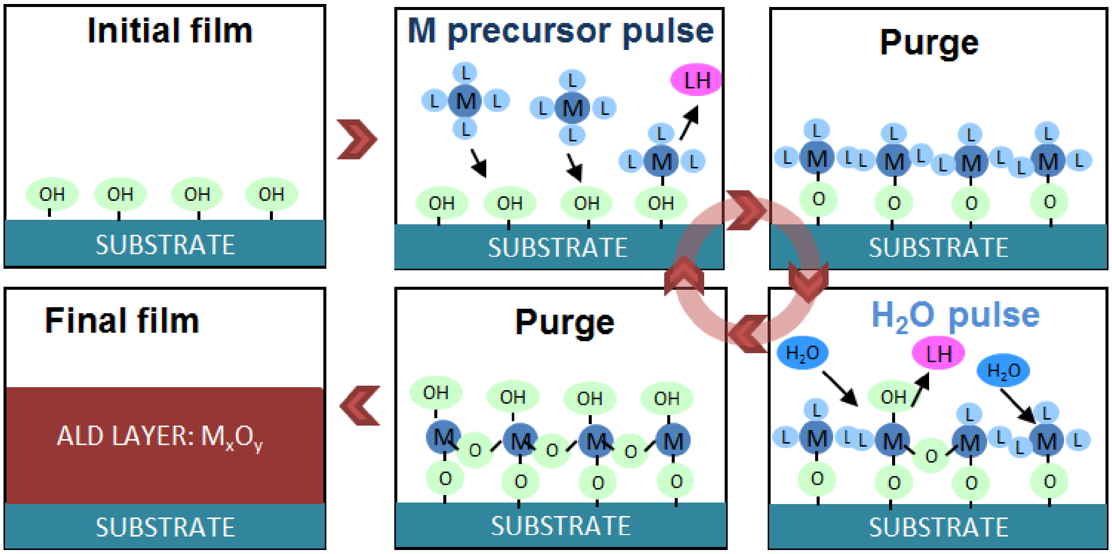

Figure 3. Schematic for a generic ALD process. A process starts with a clean substrate with a hydroxylated surface. Next a metal-organic precursor is pulsed into the reaction chamber and reacts with the –OH surface producing reactants that are pumped away. Water is then pulsed into the reactor that reacts with the remaining metal-organic precursor and, again, the by-products are pumped away. By repeating this cycle thicker layers can be added one monolayer at a time.

growth rate per cycle (GPC). Therefore, a saturation of each precursor dosage will be observed when other parameters are fixed, which features ALD as self-limiting.

1.2.1 ALD for energy storage

Initial application of ALD to electrical energy storage was in using ultrathin ALD layers as passivation/stabilization layers.[18,19] A few recent reports have used ALD films as active ion storage materials – mostly as anode materials for Li-ion battery structures.[20-24] Panda et al. demonstrated that 5 nm thick TiO_2 nanotubes produced by ALD in nanoporous alumina templates can deliver close to 100 mAh/g capacity when cycled at a high (60C) rate (nC means charge/discharge the battery with 1/n hours).[20] Cheah et al. reported a self-supporting 3D electrode with 17 nm ALD TiO_2 coated on Al nanorods, which maintained 35% of the initial capacity when cycled at 20C rate.[21] ALD of TiO_2 was also demonstrated on freestanding bio-templates, showing enhanced areal and gravimetric capacity.[22] SnO_2 and Co_3O_4 were also deposited by ALD and demonstrated with high gravimetric capacity as anode materials in Li-ion batteries.[23, 24]

1.3 Cathodic material-V_2O_5

1.3.1 V_2O_5 for Li storage application

Cathode materials typically limit the energy density of electrochemical storage devices since they have much lower specific capacities compared with anode materials.[25] Among well-known cathode materials, V_2O_5 offers relatively high specific capacity (147 mAh/g at 4.0-2.6 V; 294 mAh/g at 4.0-2.0 V; 441 mAh/g at 4.0-1.5 V), fast lithiation, and better safety, which has led to substantial research on its growth and characterization.[26-32] Recently, Cui et al. reported fast, completely reversible Li insertion in V_2O_5 nanoribbons.[28] Yu et al. reported mesoporous V_2O_5 nanofibers with significantly enhanced Li-ion storage properties.[29] High performance has also been reported by making V_2O_5 based nanocomposites, including V_2O_5/SnO_2 nanowires,[30] V_2O_5-based double-shelled nanocapsules[31] and V_2O_5/carbon nanotubes (CNT) arrays.[32]

1.3.2 ALD of V_2O_5

ALD processes for V_2O_5 are thus attractive for energy storage nanostructures. Significant research has been done using vanadyl triisopropoxide ($VO(OC_3H_7)_3$, VTOP) as the vanadium precursor and water as the oxidant, an ALD process which yielded amorphous films associated with V_2O_5 gel formation from water exposure in the process and subsequent ambient exposure.[33] In order to remove the water and crystallize the film, post annealing above 400 ^{o}C was required, posing limitations for the choice of the substrates for electrodes. Recently, Detavernier et al. extended the choices of oxidants to include plasma oxygen in a remote plasma-enhanced ALD process, achieving crystalline V_2O_5 films.[34] However, detailed process mechanism and film properties were not reported.

1.4 Overview of dissertation

1.4.1 Objective

The following objectives of this research focus on improving the electrochemical energy storage capabilities by designing ALD-enabled nanostructures and understanding the scientific issues in each system.

1. Develop ALD processes for high performance Li storage materials.

2. Understand the electrochemical storage properties of ALD thin films and identify critical factors.

3. Understand the role of electron conduction, Li diffusion, and Li ion migration in rationally-designed nanostructures.

4. Fabricate high performance electrochemical energy storage devices.

1.4.2 Outline

Chapter 2 describes the new ALD process we developed for V_2O_5 using novel oxidant ozone, which is systematically compared with the traditional water-based process. Next, the electrochemical properties of V_2O_5 films produced from two ALD processes are discussed in Chapter 3. The roles of charge/discharge voltage window, film crystallinity, and thickness are studied. In Chapter 4, three approaches for nanostructured electrodes are presented, exploring multiwall nanotubes (MWCNT) sponge, porous cellulose fiber paper, and anodic aluminum oxide (AAO) as templates, respectively. The roles of electron conduction in current collector, Li diffusion in storage material, and Li migration in electrolyte are discussed in specific cases. Chapter 5 summarizes the major research findings and impacts, and provides discussion on future work.

Chapter 2: ALD process development for V_2O_5

2.1 A new ozone based ALD process

2.1.1 Process window

The ALD V_2O_5 process was developed in BENEQ TFS 500 reactor with a 2 mbar base pressure (see Appendix). $VO(OC_3H_7)_3$ was used as the vanadium precursor, which was kept at 45°C with a vapor pressure of 0.29 torr. Ozone as the oxidizing agent was for the first time studied in ALD V_2O_5 process. A MKS O3MEGA™ ozone delivery subsystem was employed to supply a stable 18 wt% of O_3 from pure O_2 source. The film thickness was measured using a SOPRA GES5 Spectroscopic Ellipsometer. The non-uniformity is indicated by the error bars, which were standard deviations from 9 point measurements on Si wafers along the flow direction.

The growth rate per cycle (GPC) was determined as a function of deposition temperature from 150 to 210 °C, as shown in Figure 4a. A constant GPC is seen between 170 and 195 °C. Non-uniformity is less than 9% at temperatures between 170 and 185°C, but rapidly increases at higher temperature (right axis of Figure 4a). Therefore, the ALD temperature window is defined as 170-185 °C, where both stable growth rate and uniformity are observed. At temperatures lower than 170 °C, there might be insufficient activation energy for the O_3 to completely react with surface organic ligands, and the saturation for the reaction might take much longer time.[35] Above 185 °C, VTOP starts to decompose resulting in a CVD-like reaction.[34, 36] Combined, these results suggest that the ALD reaction be confined within a narrow temperature window between 170 and 185 ^{o}C (Figure 4a). Such low deposition temperatures may enable electrode fabrication by depositing crystalline V_2O_5 on flexible substrates such as polymers and bio-templates.

2.1.2 Nucleation discussion

To understand the deposition kinetics the GPC was monitored as a function of cycle number at a constant temperature of 170^{o}C (Figure 4b). In principle, the growth rate in an ideal ALD process should be constant regardless of cycle number. However, in our experiments we observed that the film growth rate was only 0.13 Å/cy at 100 cycles, and later reached about 0.22 Å/cy at 250 and 500 cycles with a slight increase to 0.27 Å/cy at 2500 cycles. This suggests the dominance of nucleation mechanisms until ~250 cycles for the O_3-based ALD V_2O_5 process, which is confirmed by atomic force microscope (AFM) in the next section.

The saturation behavior of growth rate with precursor dose, also an indicator of ALD behavior, was investigated by monitoring GPC as a function of both VTOP and O_3 pulse times, again at the constant temperature of 170 ^{o}C (Figures 4c and 4d). Reaction with VTOP was observed to saturate more quickly (0.5 s pulse) than for ozone (2 s pulse). This may suggest that oxidant is the rate-determining step in the process, which is similar to the H_2O-based ALD process reported by Musschoot et al.[34] and Badot et al.[36]

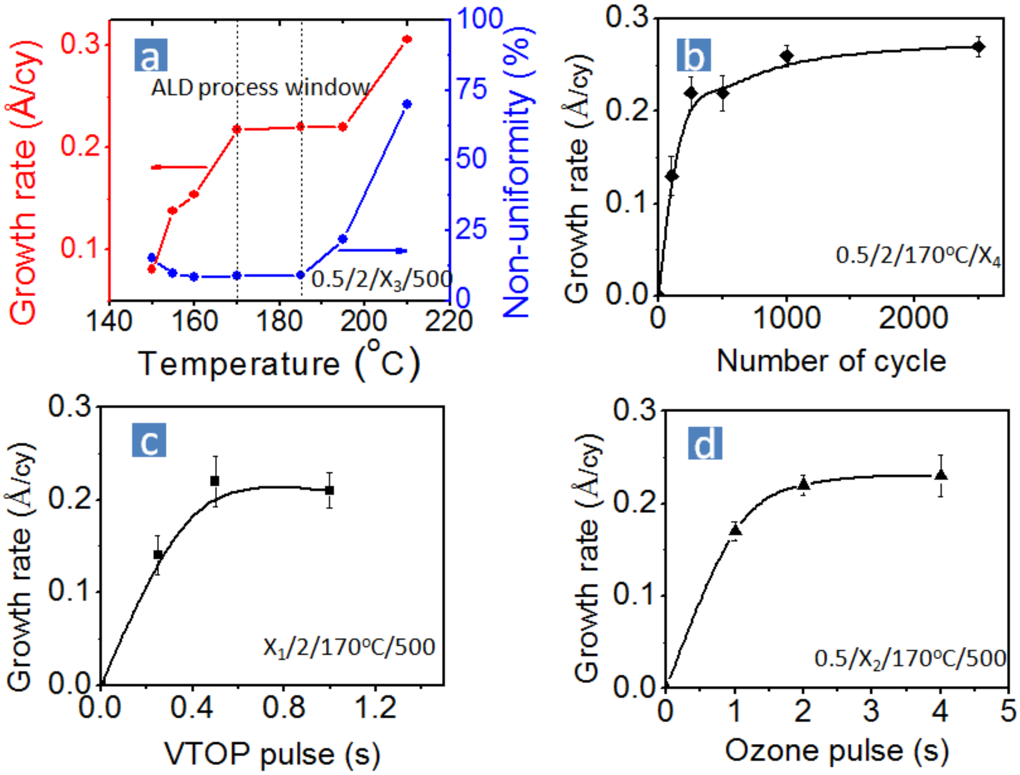

Figure 4: O_3-based ALD V_2O_5 process (the recipe VTOP pulse/O_3 pulse/temperature/cycle number is abbreviated as $X_1/X_2/X_3/X_4$): (a) growth rate and non-uniformity across 4” Si wafer as a function of temperature (dotted lines indicate ALD process window); (b) growth rate as a function of cycle number; (c) and (d) saturation behaviors of VTOP and ozone, respectively. Error bars in (b), (c) and (d) indicate standard deviations of thickness across 4” wafer.

While ALD processes typically reach non-uniformities of just a few % or less, we consider the non-uniformity here (~ 9% for films with 500 cycles ALD) consistent with the nucleation mechanism. This process involves a significant nucleation barrier, requiring about 250 cycles to initiate stable growth. Nucleation is highly sensitive to surface condition. For the films with 500 cycles ALD, the nucleation period itself comprises a significant contribution to the growth kinetics observed. Varying surface conditions across the sample could well account for variations in nucleation delay, leading to larger non-uniformities than one might anticipate for an ALD process. It is also found that the non-uniformity generally decreases with the number of cycles; the non-uniformity with more than 1000 cycles was improved to ~ 4% (see Figure 4b), consistent with our expectation. We also noticed the measured film thicknesses were randomly distributed on the 4” substrate, rather than decreasing along the flow direction, another indication that the slow nucleation accounts for the apparent non-uniformity, rather than un-optimized process for ALD.

2.2 Comparison of ozone and water based process

2.2.1 ALD Process and mechanism discussion

The ALD process windows for O_3-based and H_2O-based methods are indicated in Figure 5a. As is discussed, the O_3 process operates in a narrow temperature window from 170-185 ^oC, where both stable growth rate and good uniformity were observed.[37] The H_2O-based process shows a wider temperature window with a stable growth rate between 70-130 ^oC. The growth rate vs. cycle number was plotted in Figure 5b, where an obvious lower growth rate was found in the first 500 cycles for O_3-based films, indicative of significant nucleation barrier. For long ALD cycles, the growth rate of the two processes is similar at 0.28-0.3 Å/cycle.

To understand the reaction mechanism of the O_3-based V_2O_5 ALD process we considered previous studies on thermal H_2O, O_3 and O_2 plasma-based ALD of Al_2O_3[38-41] as well as thermal H_2O and O_2 plasma-based ALD of V_2O_5.[33, 34] In the case of Al_2O_3 ALD using trimethylaluminium (TMA) as Al precursor, direct evidence from in-situ analysis has suggested combustion-like reaction mechanism for both O_3 and O_2 plasma-based processes. However, the reaction mechanisms vary slightly with oxidability of the oxidants. For example, in the ozone/TMA ALD process, the products involve CH_4, C_2H_4, H_2O, O_2[19] and sometimes CO, CO_2[20] while in the O_2 plasma/TMA case, CH_4, CO, CO_2, H_2O and O_2 were detected in the products.[21] In the case of V_2O_5 ALD, Musschott et al. found through optical emission spectrometry (OES) that CO_2 and H_2O were generated as by-products in the O_2 plasma-based process. The process yields (001) oriented crystalline V_2O_5 films as a result of a combustion-like mechanism.[34] The mechanism for O_3-based process should also be combustion-like, but may differ from O_2 plasma-based process, as indicated by their difference in growth rates (~ 0.27 Å vs. 0.6 Å/cy). The reaction mechanism at 160 °C may also differ from that at 170 °C, as absorption/desorption and oxidability of the oxidants are temperature dependent. However, in-situ techniques, such as quadrupole mass spectroscopy (QMS), OES, and Fourier transform infrared spectroscopy (FT-IR), must be used for a thorough understanding of the detailed chemical reaction in this process. The possible mechanism for two reactions are listed below.

Combustion reaction for O_3-based process:

$$2VO(OC_3H_7)_3 + 54O \rightarrow V_2O_5 + 18CO_2(g) + 21H_2O(g)$$

Ligand-exchange reaction for H_2O-based process:

$$2VO(OC_3H_7)_3 + 3H_2O \rightarrow V_2O_5 + 6C_3H_7OH(g)$$

Barring steric hindrance effects, ALD growth rates should be close to one monolayer of V_2O_5 per cycle. However, the growth rate of O_3-based ALD of V_2O_5 is ~ 0.27 Å/cy, which is much lower than one monolayer in (001) plane of crystalline V_2O_5 (c = 4.37 Å, one monolayer thickness will be 2.19 Å). It would not be surprising if reaction involving the large VTOP molecule would be sterically hindered.[35] The growth rate of O_3-based ALD of V_2O_5 is very similar to thermal H_2O-

based process (~ 0.3 Å/cy), but lower than O_2 plasma process (~ 0.6 Å/cy).[33, 34] Similar phenomenon has been found in the case of Al_2O_3 ALD, which gives growth rate of 1.1, 1.1 and 1.7 Å/cy for thermal H_2O, O_3, and O_2 plasma-based process respectively.[40] It can be explained that the O_2 plasma pulse generates a higher number of reactive oxide surface groups for metal precursor chemisorption than do the H_2O and O_3 pulses.

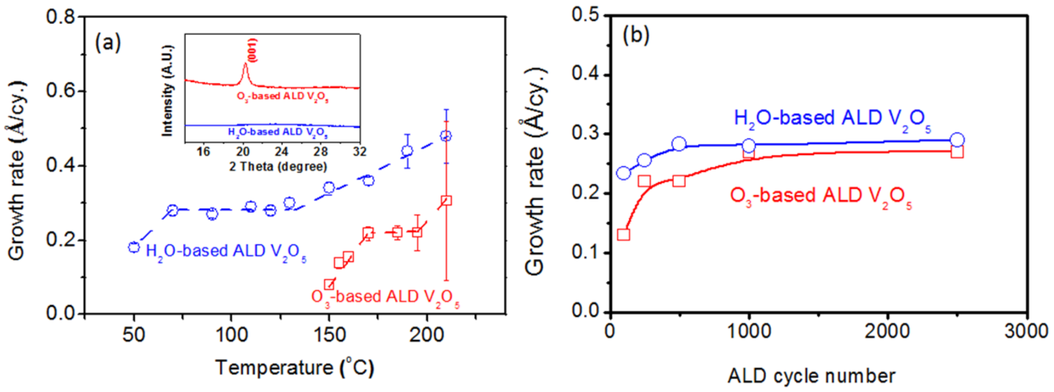

Figure 5: (a) Temperature dependent growth rate and uniformity for O_3-based and H_2O-based ALD of V_2O_5. Error bars are indicative of non-uniformity across 4" wafers. Dashed lines are guides to eyes. The films were grown with 500 ALD cycles. The O_3-based process shows a process window of 170-185°C while that for H_2O-based process is 70-130°C. The inset shows X-ray diffraction patterns for O_3-based ALD V_2O_5 prepared at 170°C and H_2O-based ALD V_2O_5 prepared at 120°C, indicating formation of the crystalline and amorphous films, respectively. (b) Growth rate as a function of cycle number.

2.2.2 Film crystallinity and morphology

Film crystallinity can be controlled directly by using different oxidants, as shown in the XRD patterns (inset of Figure 5a). The O_3-based films show characteristic (001) peak while the H_2O-based films are amorphous. To understand the temperature effect, Raman spectroscopy and thermogravimetric analysis (TGA) were conducted for the H_2O-based films deposited at 170 ^oC, compared to the O_3-based films deposited at the same temperature (not shown in Figure). For the H_2O-based films, characteristic Raman peaks were not observed and more residual water-related species were seen, indicating a significant effect of oxidant on the film crystallinity.

The two different ALD processes produced films with different surface morphology. Figure 6 compares the morphology of the O_3-based and the H_2O-based films using AFM. The color scale was kept the same for the films with same ALD cycle number for easy comparison. The O_3-based process is featured with formation of V_2O_5 islands, resulting in a relatively rough surface. On contrast, the H_2O-based films were very smooth. Figure 6i summarizes the change of RMS roughness with cycle number. When ALD cycle number increased from 100 to 2500, the RMS roughness for the O_3-based films kept increase from 0.7 to 10.4 nm while that for H_2O-based films only increased from 0.4 to 1.9 nm. Despite that, for around 70 nm thick films done with 2500 cycles, the real surface area of the O_3-based films over the projected area is 1.10, not much larger than 1.02 for the H_2O-based films.

The difference in morphology and crystallinity is also shown in the transmission electron microscope images (Figure 7), where we used Ni-coated *Tobacco Mosaic Virus* (TMV) nanowires as the template for V_2O_5 deposition.[42] The V_2O_5 layer was marked in the images according to detailed EDS analysis. In Figure 7a and b, we observed a rougher surface of the O_3-based films, in agreement with the AFM study in Figure 7. Moreover, the V_2O_5 thickness along the nanowire is very consistent for both processes, demonstrating the conformal coating capability on 3D substrates. The electron diffraction patterns from selected areas marked in Figure 7a and b as “SAD” are shown in Figure 7c and d, respectively. Diffraction rings from the substrate Ni were identified for both samples, while the characteristic diffraction patterns of crystalline V_2O_5 were only observed from the sample prepared by O_3-based process, and are indexed in Figure. 7c. The characteristic V_2O_5 lattice fringe of 0.41 nm

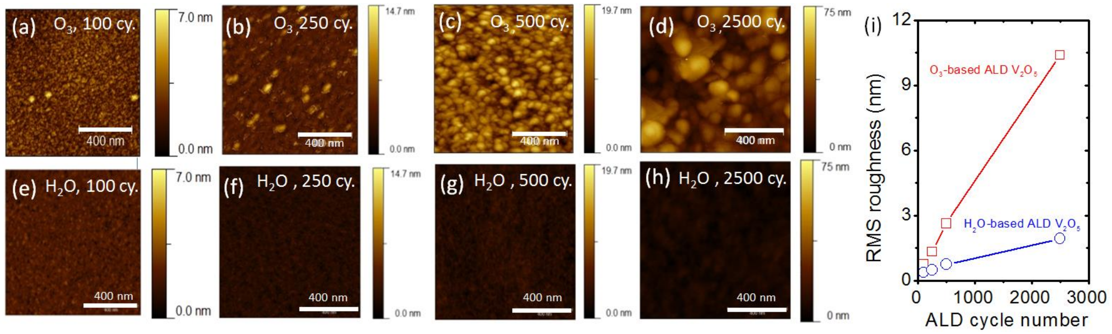

Figure 6: AFM images of (a-d) O_3-based V_2O_5 films and (e-h) H_2O-based V_2O_5 films with different ALD cycle number, (i) RMS roughness as a function of cycle number.

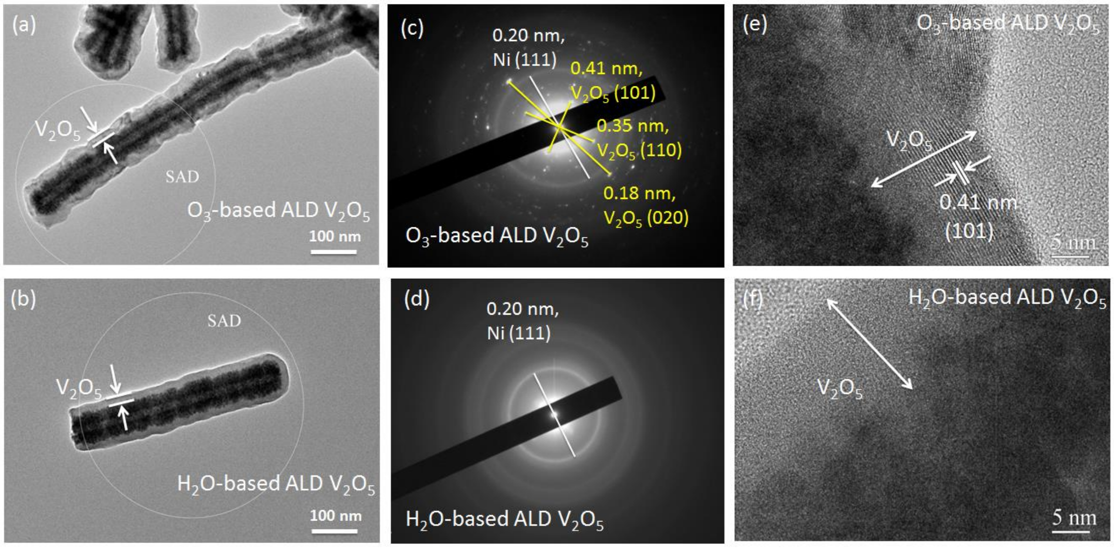

Figure 7: (a, b) TEM images of ALD V_2O_5 films deposited on Ni-coated TMV templates with selected area diffraction (SAD) patterns shown in c and d. (e, f) HR-TEM images of ALD V_2O_5 films deposited on Ni-coated TMV templates.

corresponding to the (101) plane is shown in high resolution TEM of O_3-based V_2O_5, while no lattice fringes can be seen for H_2O-based one (Figure 7e and f).

2.3 Conclusions

In this Chapter, a new O_3-VTOP ALD process for V_2O_5 is presented which shows self-limiting behavior – a characteristic ALD feature. This process is then systematically compared with the traditional H_2O-VTOP process, regarding the process window, film morphology, crystallinity. Crystalline V_2O_5 with rough surface can be directly deposited using O_3 as oxidant, while amorphous and relatively smooth films result from using H_2O as oxidant. The O_3-based process is considered as a combustion reaction with typical noticeable nucleation at initial stages, while H_2O-process reaction is based on ligand exchange. The control of film crystallinity via oxidant choice allows to evaluate the consequences of crystallinity in nanoscale V_2O_5 films with regard to electrochemical properties including gravimetric and areal capacity, energy and power density, which will be discussed in the next Chapter.

Chapter 3: Electrochemical characterizations of V_2O_5 thin film electrodes

3.1 Capacity of crystalline and amorphous films

V_2O_5 films were deposited on stainless steel disks and tested as cathodes in a half-cell configuration versus Li/Li^+ (see Appendix). Three voltage ranges were chosen: 4.0-2.6, 4.0-2.1 and 4.0-1.5 V, which correspond to one, two and three lithium intercalations per V_2O_5 unit cell respectively (abbreviated below as $1Li/V_2O_5$, $2Li/V_2O_5$, $3Li/V_2O_5$).[43] Films of 30 nm thick were studied at a relatively high rate of 1C, corresponding to a current density of 147, 294 and 441 mA/g for $1Li/V_2O_5$, $2Li/V_2O_5$ and $3Li/V_2O_5$ respectively. Because the surface area difference for the O_3-based and H_2O-based films indicated by AFM is small (less than 1.10 : 1.02), the electrochemical performance presented below should be mainly correlated with the crystallinity difference.

Figure 8 shows discharge/charge curves for crystalline and amorphous films at the three voltage ranges selected. It is immediately noteworthy that the specific capacity of the crystalline film is greater than that for the amorphous version, independent of the state of lithiation. For $1Li/V_2O_5$ (Figure 8a), two voltage plateaus are observed for the crystalline film on both discharge and charge curves, indicating the well-defined phase transformation of α-ε-δ.[8] As expected, no plateaus were observed for amorphous films in this voltage range for a lack of phase change. The gravimetric capacity for the crystalline film is 127 mAh/g at 1C rate, consistent with our previous result.[37] Table 1 compares our results with those reported in the literature, where we have also converted their reported results into gravimetric capacity with C rate for more accurate comparison and then found the previously reported capacity of crystalline V_2O_5 in $1Li/V_2O_5$ varying from 102 to 145 mAh/g, depending on the current rate and method of synthesis.[44-47] Our results for $1Li/V_2O_5$ (127-142 mAh/g) are in the higher range of these values. Unfortunately the capacity of amorphous films for $1Li/V_2O_5$ is not available in literature for comparison. However, it can be seen that for ALD films, crystalline films showed higher capacity than that of amorphous ones – (127 over 89 mAh/g).

Figure 8b shows the results for $2Li/V_2O_5$, presenting the additional δ-γ phase transition in crystalline V_2O_5 which corresponds to the plateau around 2.2 V. The gravimetric capacity for the crystalline film in $2Li/V_2O_5$ range was found to be 283 mAh/g, higher than most reported values of crystalline V_2O_5 films by other techniques shown in Table 1 (204 to 300 mAh/g).[44-46, 48-51] Again, for amorphous ALD films, no plateaus were observed in the charge/discharge curves. The capacity is 219 mAh/g, higher than 175 mAh/g for the amorphous film by electrostatic spray deposition.[51] Once again, we conclude that in the $2Li/V_2O_5$ range crystalline V_2O_5 generally showed higher capacity than amorphous ones. We also note that all the reported values for crystalline V_2O_5 in this voltage range are higher than the well-known $LiFePO_4$ cathode (166 mAh/g) cycled at similar conditions (4.5-2.0 V at 2 C rate), presumably due to the incorporation of the second lithium ion into V_2O_5 unit cell.[52]

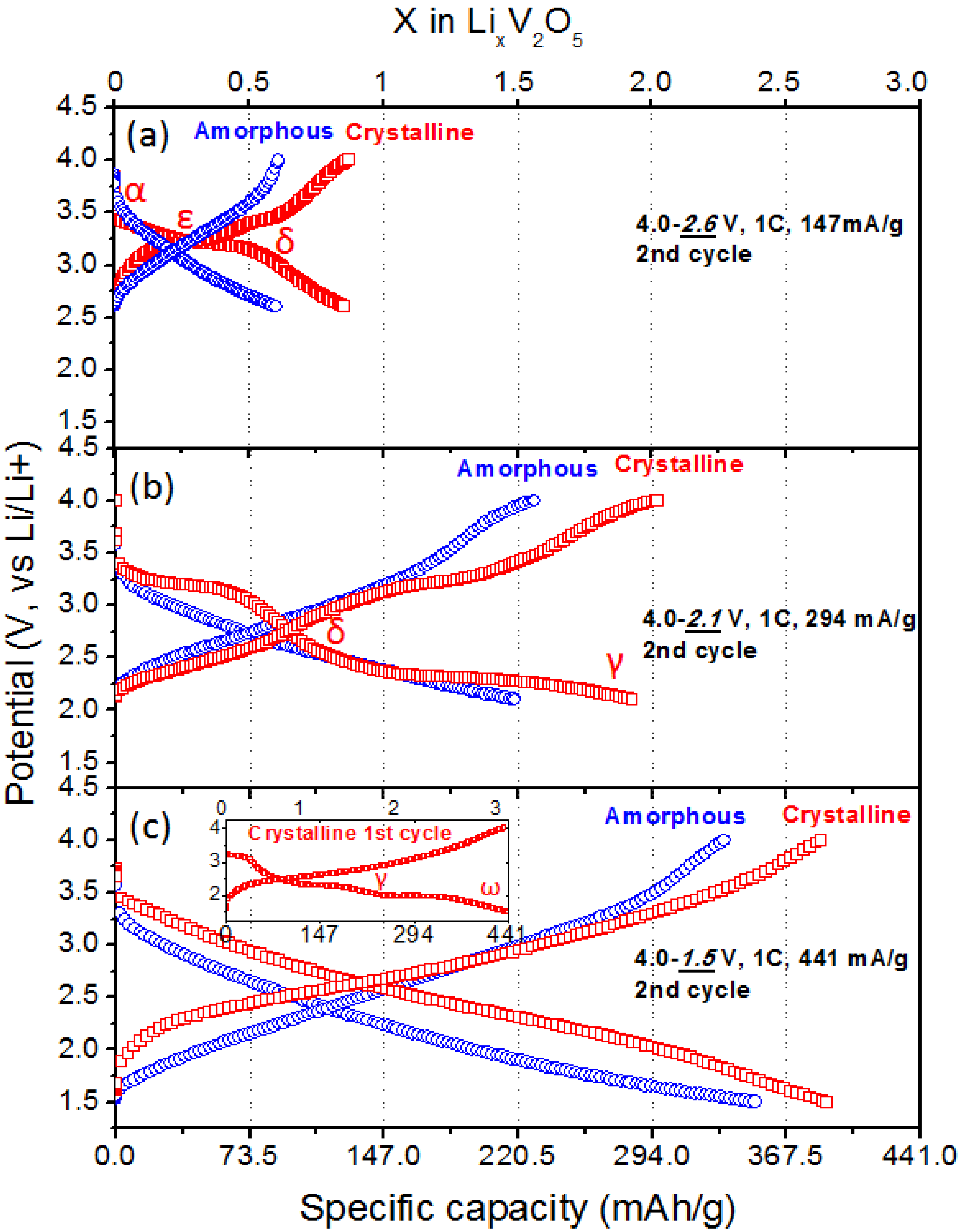

Figure 8: Electrochemical charge/discharge curves of the cells with 30 nm thick crystalline (red square) or amorphous (blue circle) V_2O_5 films at currents for 1C rates in different voltage ranges: (a) 4.0-2.6 V for $1Li/V_2O_5$; (b) 4.0-2.1 V for $2Li/V_2O_5$; (c) 4.0-1.5 V for $3Li/V_2O_5$.

Table 1. Electrochemical Performance of V_2O_5 Thin Film Electrodes

Crystallinity	Method[a]	Voltage (V)	Capacity (mAh/g)[b]	Test Rate[c]	Thickness	Ref.
For $1Li/V_2O_5$						
Crystalline	ALD	4.0-2.6	142	C/3	30 nm	[37]
Crystalline	ALD	4.0-2.6	127	1C	30 nm	This work
Crystalline	Sputter	3.8-2.8	140	C/40	600 nm	[47]
Crystalline	Sputter	3.8-2.8	102	3C	2.4 μm	[44]
Crystalline	CVD	3.8-2.8	115	C/23	1.8 μm	[45]
Crystalline	ECD	3.7-2.7	145	-	-	[46]
Amorphous	ALD	4.0-2.6	89	1C	30 nm	This work
For $2Li/V_2O_5$						
Crystalline	ALD	4.0-2.1	283	1C	30 nm	This work
Crystalline	Sol-gel	3.5-2.0	270	C/40	0.5-3 μm	[48]
Crystalline	PLD	4.1-2.0	250	~1C	800 nm	[49]
Crystalline	Sputter	3.8-2.2	204	3C	2.4 μm	[44]
Crystalline	CVD	3.8-2.2	220	C/23	1.5 μm	[45]
Crystalline	CVD	3.8-2.2	~250	~C/24	240 nm	[50]
Crystalline	ECD	3.7-2.0	236	-	-	[46]
Crystalline	ESD	4.0-2.0	~300	C/20	-	[51]
Amorphous	ALD	4.0-2.1	219	1C	30 nm	This work
Amorphous	ESD	4.0-2.0	175	C/20	-	[51]
For $3Li/V_2O_5$						
Crystalline	ALD	4.0-1.5	440	1C	30 nm	This work
Crystalline	Sputter	3.7-1.5	~388	0.4-2C	230 nm	[53]
Crystalline	PLD	4.1-1.5	300	~1C	800 nm	[49]
Crystalline	ECD	3.5-1.6	402	1.3C	160 nm	[54]
Amorphous	ALD	4.0-1.5	356	1C	30 nm	This work
Amorphous	ALD	4.0-1.5	455	C/10	200 nm	[55]
Amorphous	PLD	4.1-1.5	346	~2C	310 nm	[49]

[a] ALD-atomic layer deposition; PLD-pulse laser deposition; CVD-chemical vapor deposition; ECD-electrochemical deposition; ESD-electrostatic spray deposition.

[b] The numbers with "~" prefix are calculated from given thickness and current density per area, assuming V_2O_5 density is 3.36 g/cm^3. E.g., $x\ \mu Ah/cm^2 \approx \frac{3x}{y} mAh/g$, where y is thickness in μm.

[c] The numbers with "~" prefix are calculated from given thickness and current density per area, assuming V_2O_5 density is 3.36 g/cm^3 and theoretic capacity of 147 mAh/g for each Li in V_2O_5. E.g., $x\ mA/cm^2 \approx \frac{20x}{yz} C$, where y is thickness in μm and z is expected number of Li in V_2O_5.

The discharge/charge curves for 3Li/V_2O_5 voltage range are shown in Figure 8c. Another well-known phase change from γ to ω was observed around 1.8 V for the crystalline film in the first discharge curve, consistent with all the phase transition observed in bulk V_2O_5.[43] The first discharge capacity of 440 mAh/g was observed, close to the theoretical value of 441 mAh/g for 3 Li intercalation into V_2O_5 unit cell. However, all the plateaus disappeared in the second charge/discharge curve due to the formation of ω-$Li_xV_2O_5$ phase which is known to form a solid solution.[56] The capacity dropped to 389 mAh/g in the second discharge, in agreement with literature on ω-phase cycling[56]. In this voltage range, crystalline V_2O_5 ALD films again showed advantage over those synthesized by other methods, which delivered capacity from 300 to 402 mAh/g (Table 1).[49, 53, 54] As expected, amorphous ALD films showed no plateaus in this voltage range, but the second discharge capacity (356 mAh/g) is close to that of crystalline films (389 mAh/g). Other reported values for amorphous films vary from 346 to 455 mAh/g, with ALD films showing the highest.[49, 55] Generally, in this voltage range crystalline V_2O_5 shows comparable capacity to the amorphous one starting from the second cycle.

These specific capacities underscore two conclusions. First, the crystalline films obtained by using ozone oxidant are definitely higher than those for amorphous films from H_2O at one and two lithium intercalation stages. Second, by comparison to previous data in Table 1, it can be concluded that the ALD films provide specific capacity in the upper range of reported values. This may result, in part, from the fact that our ALD V_2O_5 films are generally thinner than those prepared by other methods, enabling more of the film to be used for energy storage at a given C rate for charging/discharging. However, as discussed above, the need for higher power at high energy requires nanostructured designs, for which thin conformal ALD layers are particularly well suited. The role of thickness is discussed in greater detail below.

3.2 Cycling of crystalline and amorphous films

Cycling tests for crystalline and amorphous films for the three voltage ranges were performed, yielding gravimetric capacities from 2nd to 100th cycle as summarized in Figure 5. The ALD films are stable upon cycling, showing less than 0.15% decay per cycle when cycled for 2Li/V_2O_5 and 1Li/V_2O_5. A relatively faster decay in the first 20 cycles was observed for both crystalline and amorphous films in 3Li/V_2O_5 range, probably due to formation of a solid electrolyte interface (SEI) at low voltage. The difference of cycling degradation rates of crystalline and amorphous films for 1, 2, or 3 Li intercalation cases is not very noticeable, with amorphous films slightly more stable in 3 Li case.

We attribute at least part of the good cycling performance primarily to strong chemical bonding and good mechanical adhesion of the ALD V_2O_5 to the current collecting substrate. The relatively low temperature ALD process for depositing the V_2O_5 active storage material also reduces the risk of delamination caused by thermal stress between active material and substrate, [50] and thinner films may also reduce risk of delamination during cycling, as found in Si materials.[57] Such effects may also contribute to the generally higher capacities of ALD films compared to most other methods.

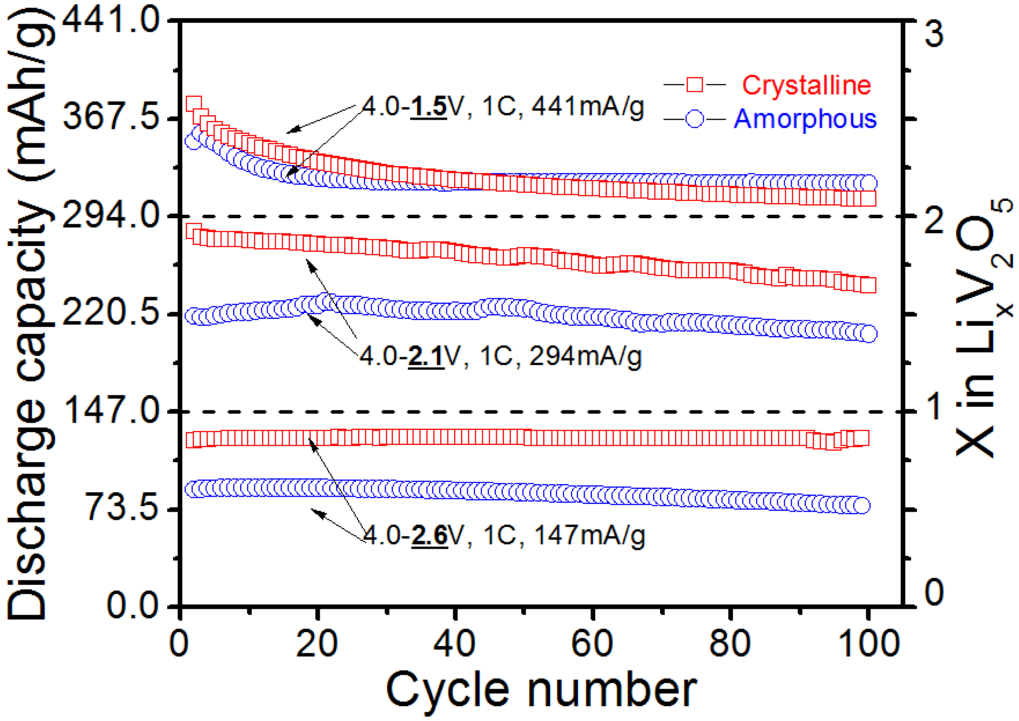

Figure 9: Cycling performance of the cells with 30 nm thick crystalline (red square) or amorphous (blue circle) V_2O_5 films at different voltage ranges at 1C current. Dashed lines indicate theoretic values.

3.3 Thickness dependence

For storage applications where high power as well as high energy is important, optimizing thickness of the active storage material is a key factor. As thickness increases, total energy storage capacity increases at low rate but power, which is related to capacity at high rate, may be limited due to diffusion kinetics of ion transport in the storage material. On the other hand, films too thin do not enable enough energy to be delivered at a given area. These considerations suggest, for a given materials system, an optimum thickness of storage material for achieving highest power.

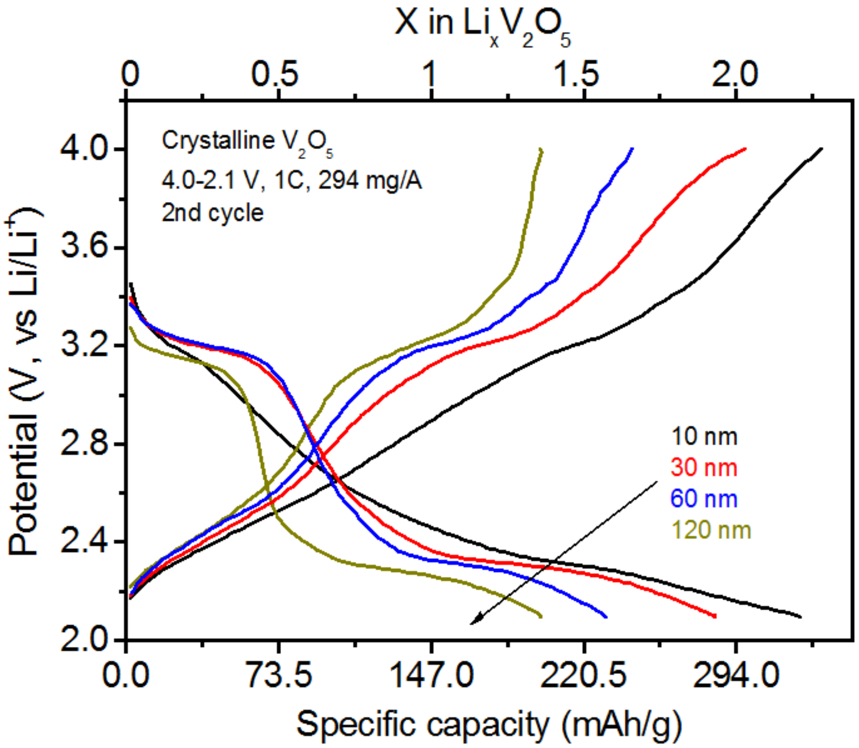

Figure 10: Second cycle charge/discharge curves of the cells with 10-120 nm thick crystalline V_2O_5 films (4.0-2.1 V for $2Li/V_2O_5$, 1C rate).

To pursue this idea, we consider the thickness dependence of electrochemical properties for crystalline V_2O_5 in the 4.0-2.1 V range, where both high capacity and stable cyclability occur. We first studied gravimetric capacities of films at 1C rate with thicknesses of 10, 30, 60 and 120 nm, shown in Figure 10. The capacities for these films are 324, 283, 230 and 198 mAh/g respectively, with the thinnest film showing highest capacity. The same trend was shown in TiO_2 nanotubes studied in the 2-40 nm thickness range.[20] The capacity of the 10 nm thick V_2O_5 film is higher than the theoretical value of 294 mAh/g for the 2Li/V_2O_5 range, perhaps a result of significant surface charge (double layer capacitance) to the capacity.

To explore the high power regime, we also cycled the cells with high rates up to 50C. For each C rate the cells were cycled 10 times, the rate was then increased and repeated, as shown in Figure 11a. To compare these values, Figure 11b plots the second cycle discharge gravimetric capacity for each C rate as normalized to that for 1C rate. In Figure 11c the gravimetric capacity is plotted vs. film thickness. For each thickness, higher rates produce lower gravimetric capacities, and at each fixed scan rate thinner films consistently show higher gravimetric capacities. This illustrates the tradeoff between thickness and rate performance if total power handling capability is a valued metric. We also note that at a high rate 50C, the films of 10, 30 and 60 nm can still deliver high gravimetric capacities of 164, 120 and 81 mAh/g, respectively.

Interestingly, we notice there is a particularly sharp capacity drop for the 120 nm thick film when the rate is increased to higher than 5C. This result is more obvious in Figure 11b and 11c, where a large difference can be seen between the 10-60 nm films and that of 120 nm film. To understand this, we estimated the Li diffusion time τ in films as a function of thickness L. Mcgraw et al. reported the Li diffusivity D in crystalline V_2O_5 in 2Li/V_2O_5 range as 5×10^{-14}-2×10^{-12} cm^2/s.[58] If we take a middle value from this range, 3×10^{-13} cm^2/s, and use the kinetic equation $\tau = L^2/2D$, we can calculate the time required for Li diffusion. The result is shown in Figure 11d, where the corresponding C rate is also marked for reference. The diffusion time for 60 nm thick film is 60 s, corresponding to 60 C, higher than the C rates we studied here.

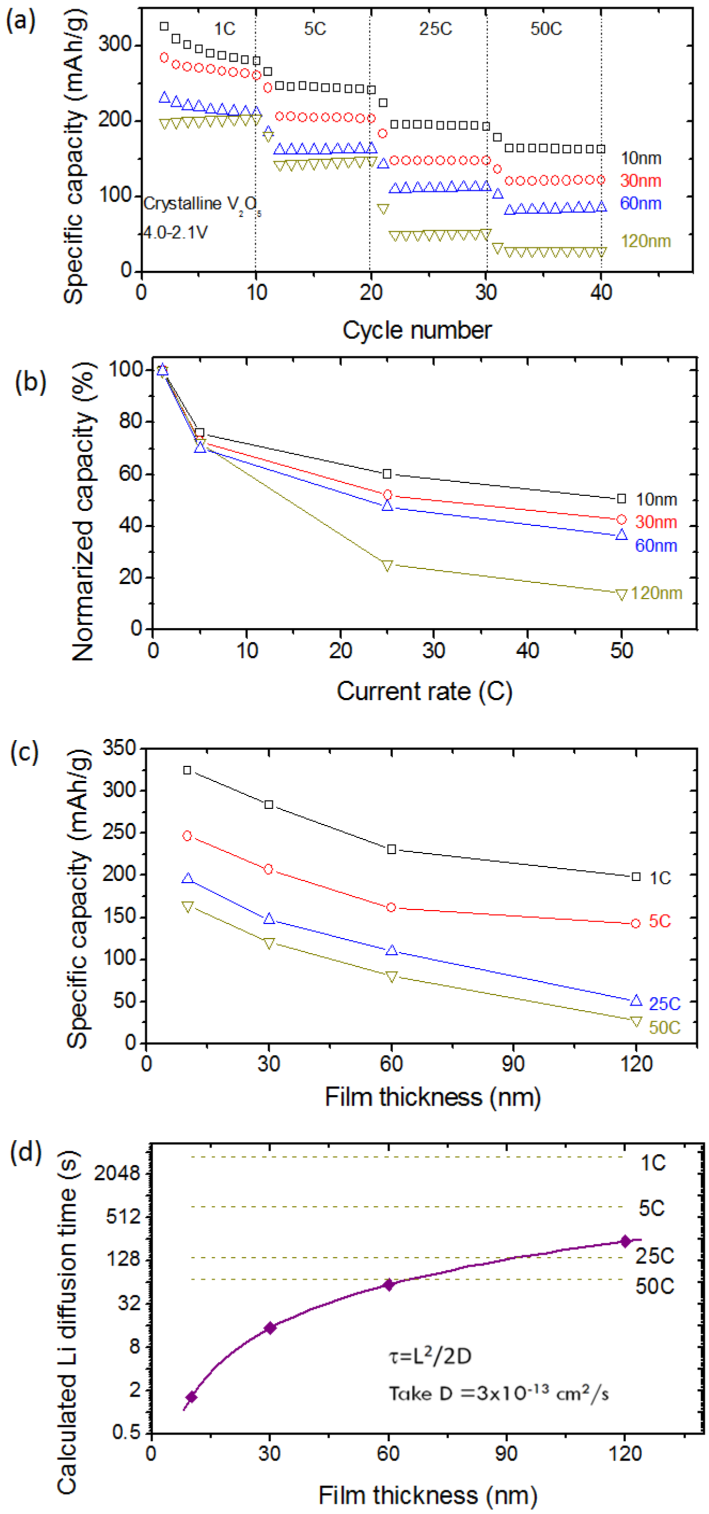

Figure 11: (a) Rate performance of the coin cells with 10-120 nm thick crystalline V_2O_5 films in the range of 4.0-2.1 V for $2Li/V_2O_5$. The cells were cycled for 10 times at each C-rate. The data in (a) is summarized in (b) where the second cycle discharge gravimetric capacity for each C rate is normalized with that of 1C rate, and (c) where the gravimetric capacity is plotted vs. film thickness. (d) Estimated Li diffusion time for 10-120 thick V_2O_5 films, assuming a Li diffusion coefficient of 3×10^{-13} cm^2/s.

However, for 120 nm thick films, the diffusion time is 240 s, corresponding to 15C, lower than 25C where we start to see a significant drop in gravimetric capacity. The results presented here thus suggest that Li diffusion is the limiting factor for high rate performance for the 120 nm filmsWe also considered the role of electron conductivity in the V_2O_5 electrodes. The total circuit series resistant from electrochemical impedance spectroscopy (EIS) measurements (not shown here) for the cell with 120 nm V_2O_5 cathode was 20.6 Ω, which is mainly from the V_2O_5 electrode resistance and electrolyte resistance. The total voltage drop caused by this resistance is less than 0.03V, giving a current density of 14.7A/g at 50 C for electrode mass of 91 µg. This means that the voltage difference associated with the current collector/electrode interface and the electrode/electrolyte interface is even less than 0.03 V, i.e., too small to be responsible for the large capacity drop we observed on thick films.

A conventional Ragone plot for power and energy is shown in Figure 12 to convey a picture of the power-energy densities of ALD crystalline V_2O_5 tested from 4.0-2.1 V for $2Li/V_2O_5$. Gravimetric features are shown in Figure 12a, where thinner films present both higher power and energy because they have easier access to both electrons from current collector and Li^+ from electrolyte. To obtain a rough estimate of performance at device level, we assume a 50 % mass fraction of active V_2O_5 as we demonstrated before using the low density and high porous multiwall carbon nanotubes (MWCNT) as scaffold and current collector (more details in the next Chapter).[59] Taking into account that the total cathode mass is normally around 40% of the total device, we calculated the device performance by applying a factor of 20% on the performance of V_2O_5 only, which is also shown in Figure 8a. The estimated device performance is obviously superior to current Li-ion batteries.[60] A factor of one order increase in gravimetric power density could be expected.

If the capacities are normalized by area (Figure 12b), we found that from 10-60 nm, both areal energy and power increase with the thickness, because increased material loading is more significant than the decrease in gravimetric capacity. In this thickness regime, the highest power of 0.93 mW/cm^2 is achieved with total energy of 0.005 mWh/cm^2. Most importantly, power increase was achieved without sacrificing much energy. However, for thicker films of 120 nm, more energy can be obtained only if the cell is cycled slowly enough (1C and 5C). But for fast cycling at 25C and 50C, a higher power was achieved in the price of a significant decrease in energy. As we interpreted above, this is because of the limited Li diffusion at high rate, rendering

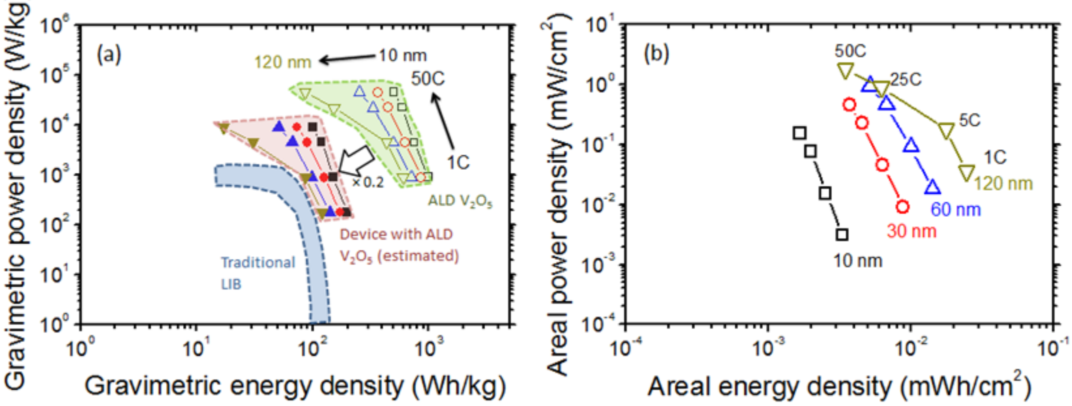

Figure 12: (a) Gravimetric power density vs. energy density for the cells with 10-120 nm thick crystalline V_2O_5 films in the range of 4.0-2.1 V for $2Li/V_2O_5$. The estimated device performance were plotted with a factor of 20% (50% mass fraction of V_2O_5 using MWCNT as scaffold and current collector, and 40% mass fraction of cathode over device), to compare with traditional Li-ion batteries. (b) Areal power density vs. energy density from the cells with 10-120 nm crystalline V_2O_5 films in the range of 4.0-2.1 V for $2Li/V_2O_5$.

most of the material in thick film unused. We conclude that above a certain thickness, 60 nm in this case, making thicker films will not result in better energy-power characteristic. In order to achieve high power density per area while maintaining high energy, there should be an optimized thickness for any active material to balance the amount of material and gravimetric capacity at high current. This conclusion should apply for any substrate and therefore shine light on 3D microbattery designs.

3.4 Conclusions

Electrochemical tests showed that ALD V_2O_5 films present higher capacity than most literature values reported using other deposition techniques. Our results showed that crystalline films have higher capacities than amorphous ones for $1Li/V_2O_5$ (127 vs. 89 mAh/g) and $2Li/V_2O_5$ (283 vs. 219 mAh/g), while for $3Li/V_2O_5$, both films showed similar capacities stabled at ~320 mAh/g. Thinner films are favored for high gravimetric capacity, especially at higher C rates. The important tradeoff between thickness and usable gravimetric capacity is clearly demonstrated for the higher-capacity crystalline material. At 120 nm thickness, capacity decreases rapidly at 25C and 50C rate, which is explained by the limited Li diffusion, while considerably thinner films suffer from limited areal capacity to support total high power. Accordingly, areal energy and power density is optimized with V_2O_5 thickness round 60 nm. We believe these kinds of investigations focusing on both power and energy will be essential for the design of next-generation 3D nanostructured electrodes for high power and energy storage devices.

Chapter 4: 3D electrode fabrications and tests in Li half cells

4.1 Multiwall carbon nanotube (MWCNT) sponge/V_2O_5 electrodes

4.1.1 Motivation

Carbon nanotubes (CNTs) are particularly attractive in combination with active storage materials because of their excellent electronic conductivity, low density, and good mechanical and chemical stability. A successful strategy reported by several groups is to create interpenetrating networks of CNTs and V_2O_5 nanowires.[61-63] To further reduce electron transport distances, V_2O_5 can be directly deposited on the surface of CNTs; *e.g.*, Prakash *et al.* reported commercial CNTs coated and stabilized with 4-5 nm V_2O_5 through a solution based hydrolysis method.[64] The as-prepared V_2O_5-CNT cathode showed high power density as well as gravimetric and volumetric energy density, but the achievable V_2O_5 mass loading was limited and the cyclability of the material was poor.

Inspired by these previous studies, we designed and developed a novel strategy to create high density assemblies of composite V_2O_5-CNT nanostructures for high performance cathode applications, featuring multiwall carbon nanotube (MWCNT) sponge as a structural backbone and nanostructured current collector, and atomic layer deposition (ALD) as a method to deposit V_2O_5 as a coating and to anchor the MWCNTs. The rationale is as follows. MWCNT sponge has excellent electronic conductivity, high surface area, and high porosity. [65, 66] ALD, a powerful technique with unique capabilities such as sub-nm thickness control, extremely high film uniformity, and unparalleled conformality, can exploit this high surface area by conformally coating the CNT sponge.[35, 67-69] The high surface area of MWCNT and conformal coating capability of ALD enable significantly enhanced loading of active material to achieve high energy density compared to prior work.[64] In addition, the excellent electronic conductivity of MWCNT in intimate contact with a thin layer of V_2O_5 will profoundly reduce the time required for electron and ion transport during the charge-discharge process, while the high porosity of the MWCNT sponge facilitates ion migration in the electrolyte, all of which are properties essential for high power density.[70, 71]

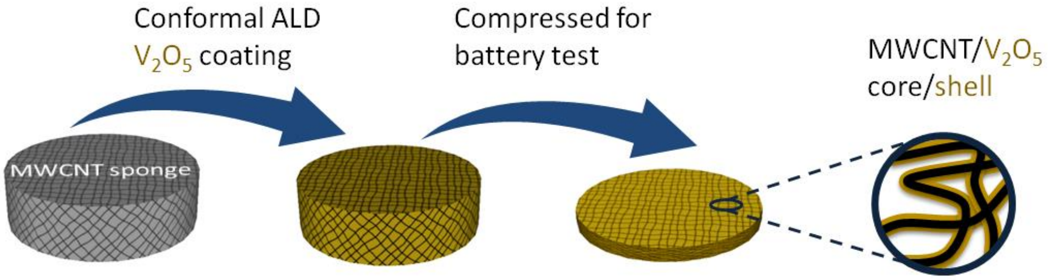

Figure 13: Schematic of experimental flow to fabricate V_2O_5 coated MWCNT sponge. The highly porous MWCNT sponge enables conformal coating of V_2O_5 on the surface of MWCNT by ALD. The coated MWCNT sponge can be pressed and used as the cathode, where MWCNT functions as electron conductor, V_2O_5 as Li storage material, and the open pores allow easy electrolyte access. The thickness of the sponge is ~ 2 mm before and ~ 170 µm after compressing to form a coin cell battery.

4.1.2 Structural characterizations

Our strategy is shown schematically in Figure 13. We first used chemical vapor deposition (CVD) to grow MWCNT sponge in a quartz tube at 860 °C, which as-prepared has very low density (~7 mg/cm^3) and high porosity (>99%).[65] Then the sponge was cut into the desired size (typically 0.143-0.174 cm^2, ~2 mm thick) and placed in a commercial ALD reactor, where 1000 cycles H_2O-based ALD V_2O_5 was deposited on the MWCNT sponge. When the V_2O_5-coated MWCNT sponge was assembled in a coin cell battery, it was compressed from ~ 2 mm to ~ 170 µm thickness (see experimental details). Since the sponge material is very highly porous, even this 12X compression in one direction will not degrade the ability for ion transport through pores to the active material, i.e. the 3-D porosity is preserved. This is critical for the electrochemical performance especially at high charge-discharge rate, when depletion of ion concentration at the electrolyte/electrode surface could be a limiting factor.[71] A good example can be found in the work by Rinzler *et al.*, where it was shown that engineering the macroporosity of CNT films can double the specific capacitance.[70]

Figure 14 shows scanning electron microscope (SEM) images of the MWCNT sponge before and after ALD V_2O_5 coating, together with a photograph of the sponge (inset of Figure 14a). As expected the ALD coating is very uniform and no uncoated MWCNT can be seen after the deposition. The outer diameter of the MWCNT is ~ 32 nm on average, in line with our previous results.[65] After 1000 cycles of ALD V_2O_5, the outer diameter increased to ~ 66 nm, indicating V_2O_5 thickness of ~ 17 nm (related measurements are described below). The same ALD process on planar Si substrates gave a larger measured thickness ~ 30 nm, suggesting a significant nucleation barrier for the ALD process on MWCNT surface. This would not be surprising since the surface of MWCNT is generally free of hydroxyl or carboxyl groups and thus relatively inert to ALD. Previous studies indicated that the nucleation inhibition can be overcome by surface functionalization using HNO_3 acid or NO gas.[72, 73] Alternatively, the reduced growth rate could also result if precursor doses were not high enough to saturate the surface reaction over the unusually high surface area of the sponge, as discussed further below. While we are continuing to investigate the surface modification of MWCNTs, ALD recipe optimization, and novel O_3-based ALD V_2O_5 process we developed recently,[74] the nanocomposite sponge structure displays significant electrochemical performance that we focus on here.

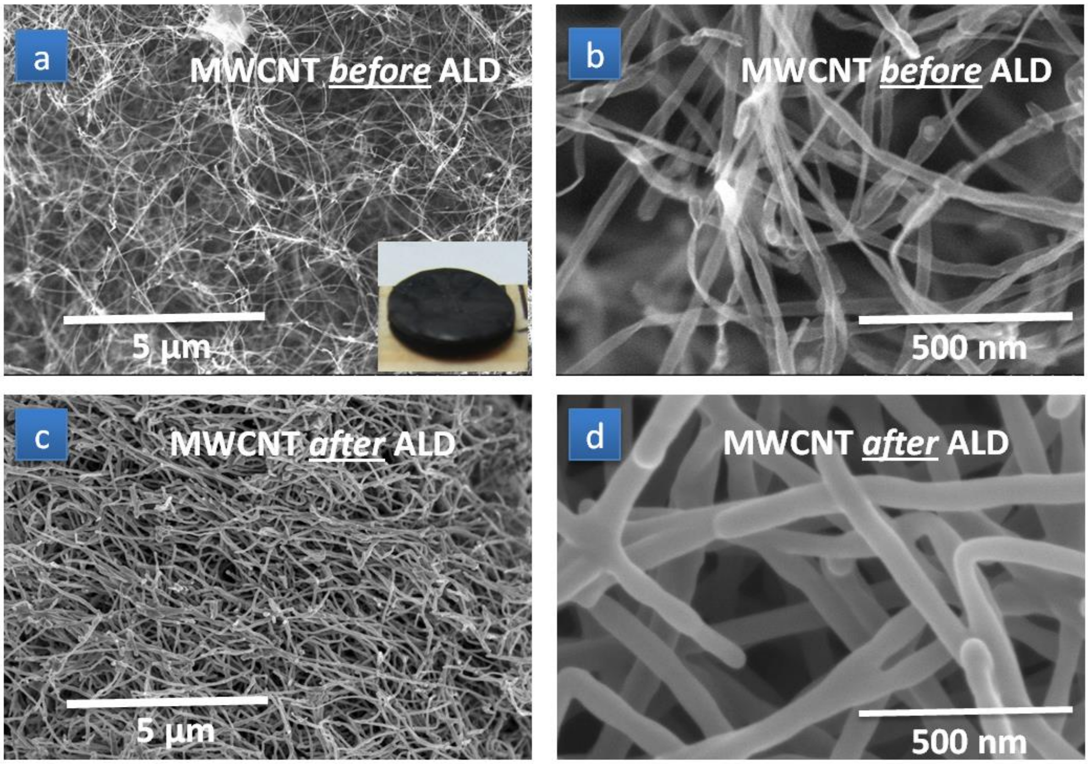

Figure 14: SEM images of MWCNT sponge (a, b) before and (c, d) after 1000 cycles of ALD V_2O_5 coating. Inset of (a) shows an optical photograph of MWCNT sponge with 6.4 mm diameter × 2 mm thickness.

TEM also shows uniform V_2O_5 coatings over individual MWCNT's were achieved using H_2O-based ALD (Figure 15a). The desired MWCNT/V_2O_5 coaxial structure can be well resolved in higher magnification TEM images (Figure 15b and c). The energy-dispersive X-ray spectroscopy (EDX) in the inset of Figure 15b shows clear evidence of core/shell tubular structure with the V and O signal peaks at the outside (shell) of the composite nanotube and the C signal peak at the inner part (core) of the tube. The interface between V_2O_5 and MWCNT can be also distinguished from the grey scale contrast cross the nanotube, according to the TEM-based methodology developed in our laboratory for nanotube analysis.[75] No diffraction features are seen from the V_2O_5 layer, which indicates it is amorphous, consisting with our previous result.[76]

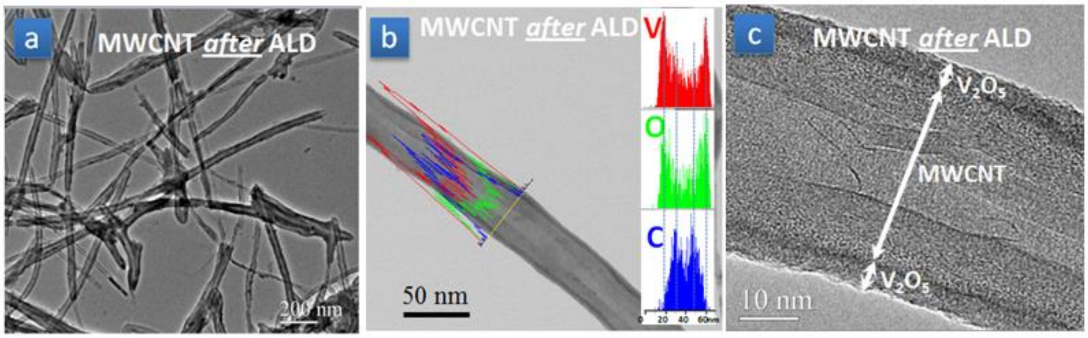

Figure 15: (a) TEM image of MWCNT coated with ALD V_2O_5 showing uniform coating. (b, c) High magnification TEM images, where the co-axial structure of MWCNT and V_2O_5 are well resolved and distinguished by the EDX line scans across the nanostructure shown in the inset of (b) and by the grey scale contrast in (c).

The thickness of V_2O_5 layer as observed by TEM is only 4-6 nm, less than the ~17 nm measured in SEM. It can be presumed that the penetration of the ALD film into the sponge may be limited, given the high surface area and aspect ratio, as well as the tortuous structure of the sponge, leading to thinner films in the middle of the sponge than at the surface. Since the SEM observation focuses on the surface of the sponge while the TEM observation originates from a random location in the sponge, limited penetration of the ALD film into the sponge will cause smaller thicknesses observed in TEM than in SEM, as found here. This might be regarded as non-ideal conformality, albeit on a considerably larger length scale than the film uniformity over high aspect ratio MWCNT's. Indeed, the thickness depletion from surface to inner part of the sponge is not uncommon for ALD coating on very high aspect ratio structures.[77]

4.1.3 Electrochemical performance

The MWCNT sponge was also characterized with Raman spectroscopy before and after ALD the coating, showing the expected MWCNT and V_2O_5 (not shown in Figure here). With the clear evidence for successful synthesis of MWCNT/V_2O_5 core/shell sponge, samples were incorporated into coin cells for electrochemical performance tests. The MWCNT/V_2O_5 sponge cathodes were tested in a half-cell configuration using Li metal as the standard anode. To fully explore the capacities, we chose three voltage ranges: 1Li/V_2O_5, 2Li/V_2O_5, 3Li/V_2O_5 at 4.0-2.6, 4.0-2.1 and 4.0-1.5 V, respectively.[78]

As shown in Figure 16a, the C/20 discharge gave an expected higher capacity of 204 mAh/g than that at 1C rate (167 mAh/g, 82% of 204 mAh/g). We noted that the capacity difference at 1C and C/20 is small because the thin V_2O_5 layer and the high conductivity of MWCNT provide fast kinetics. Therefore, we concentrate on the 1C rate to represent the results of our composite. In addition, testing at 1C rate is 20X faster than that at C/20, significantly shortening experiment time for 100 cycle life time testing. Shown in Figure 16b, the MWCNT sample coated with ALD V_2O_5 took 2043 s to discharge to 2.1V, while that with MWCNT only took 37 s. This result means that MWCNT only stored a tiny amount of charge compared to V_2O_5. The portion of charge stored by MWCNT is less than 2% (37/2043 = 1.8%). Since most capacity is from V_2O_5, the cell performs more like a battery than a carbon supercapacitor.

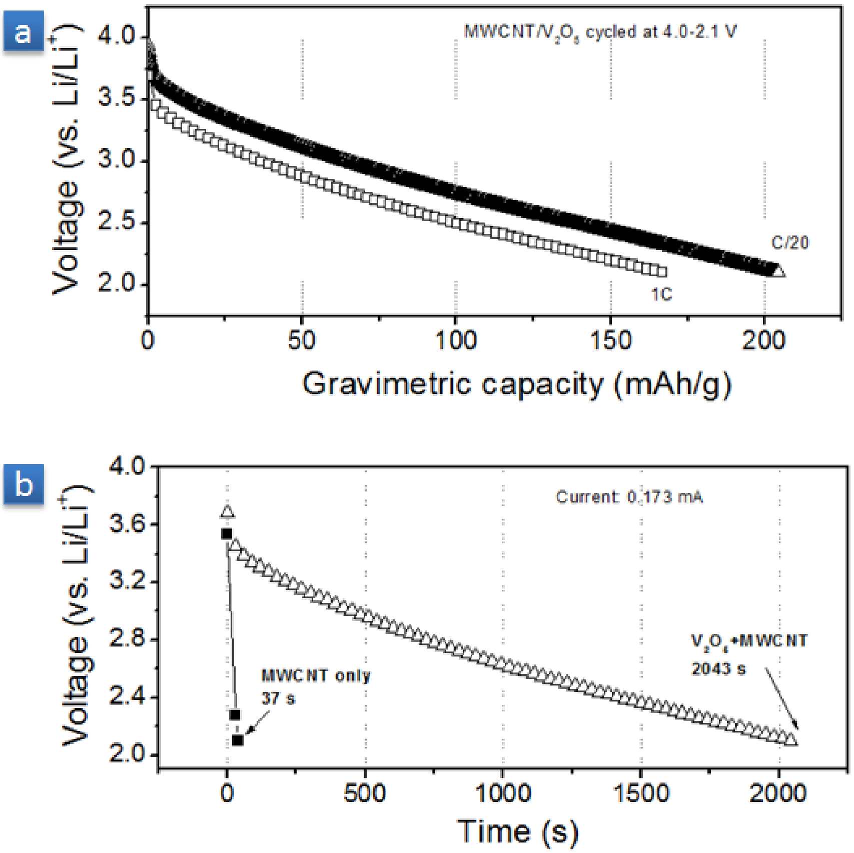

Figure 16: (a) Gravimetric discharge curves for the cells with MWCNT/V_2O_5 sponge cathodes for 2Li/V_2O_5 (4.0-2.1 V) at C/20 and 1C rate. (b) Discharge curve for V_2O_5 coated MWCNT and equal amount of MWCNT only with same current.

Since the sponge was only ~ 170 μm thick after compression, an attractive (though not unique) application would be in a microbattery, where the capacity per unit substrate area is of particular interest.[79, 80] The charge-discharge curves plotted as voltage *vs.* areal capacity at the second cycle are shown in Figure 17a. No plateau can be observed at any voltage range during charge-discharge procedures, indicating the absence of phase transitions typical of the Li (de)/insertion for crystalline V_2O_5 films.[78] The absence of plateaus has been reported before as a characteristic for amorphous films.[81]

The corresponding capacities for the second discharge cycle for $1Li/V_2O_5$, $2Li/V_2O_5$ and $3Li/V_2O_5$ are 514, 818 and 1284 μAh/cm^2 respectively. These values are all larger than those for commercial planar Li-ion microbatteries (113 μAh/cm^2)[82], and comparable to most state-to-art three-dimensional (3D) microbatteries (in the range of 1 mAh/cm^2).[83]

The sponge architecture provides a dramatic enhancement of storage capacity. For $2Li/V_2O_5$ (4.0-2.1 V), we compared the areal capacity of the MWCNT/V_2O_5 sponge with thin film V_2O_5 simultaneously deposited on a planar stainless steel disk (Figure 17b). The second cycle discharge capacity for the planar V_2O_5 film is only 1.8 μAh/cm^2, while the sponge delivered a dramatically higher capacity - 818 μAh/cm^2 - a 453X increase. This increase is primarily attributed to the high surface area of the sponge that enabled 517X more V_2O_5 (determined from measured mass), but more importantly to the superior nanoarchitecture that makes most of the V_2O_5 easily accessible for Li (de)/intercalation on a short time scale. We note that this areal capacity enhancement (453X) is significantly higher than other designs using 3D micro-channels (20-30X)[80], free standing Al nanorods (10X)[84] and bio-templated nanowire forest (~ 8X).[85]

The performance of the cells cycled at various voltage ranges (Figure 17c) shows excellent cycling stability at for 1Li/V_2O_5 and 2Li/V_2O_5 (4.0-2.6 and 4.0-2.1 V), with only modest decay after 100 cycles (< 0.1 % decay per cycle). In contrast, for 3Li/V_2O_5 (4.0-1.5 V), capacity decay was much larger, *i.e.*, 49 % capacity loss after 100 cycles (0.49 % decay per cycle). However, this decay was not as fast as that reported for V_2O_5/SnO_2 nanowires, which lost 38% capacity after only 15 cycles at 4.0-1.8 V (2.5 % decay per cycle).[86]

There was an obvious increase in capacity for 3Li/V_2O_5 (4.0-1.5 V) at the first five cycles, which is quite different from that in the other two voltage ranges. This “warm-up” behavior is possibly due to the improved wetting of electrolyte-electrode interphase, especially for nanoscale porous electrode materials. In addition, we propose another possible proton exchange mechanism. The thermogravimetric analysis (TGA) showed about 3% weight loss between 100 and 325 ^{o}C due to residual water-related species in the film (not shown in Figure). In the first few cycles, the associated protons in the V_2O_5 film can be pulled out while Li is pulled out during charge, leaving sites open for additional Li insertion during the next discharge. That this behavior is more obvious at 4.0-1.5 V than 4.0-2.1 and 4.0-2.6 V could be explained that the residual H_2O-related species in V_2O_5 is fairly stable and thus wider range of voltage is required to make the proton exchange happen.

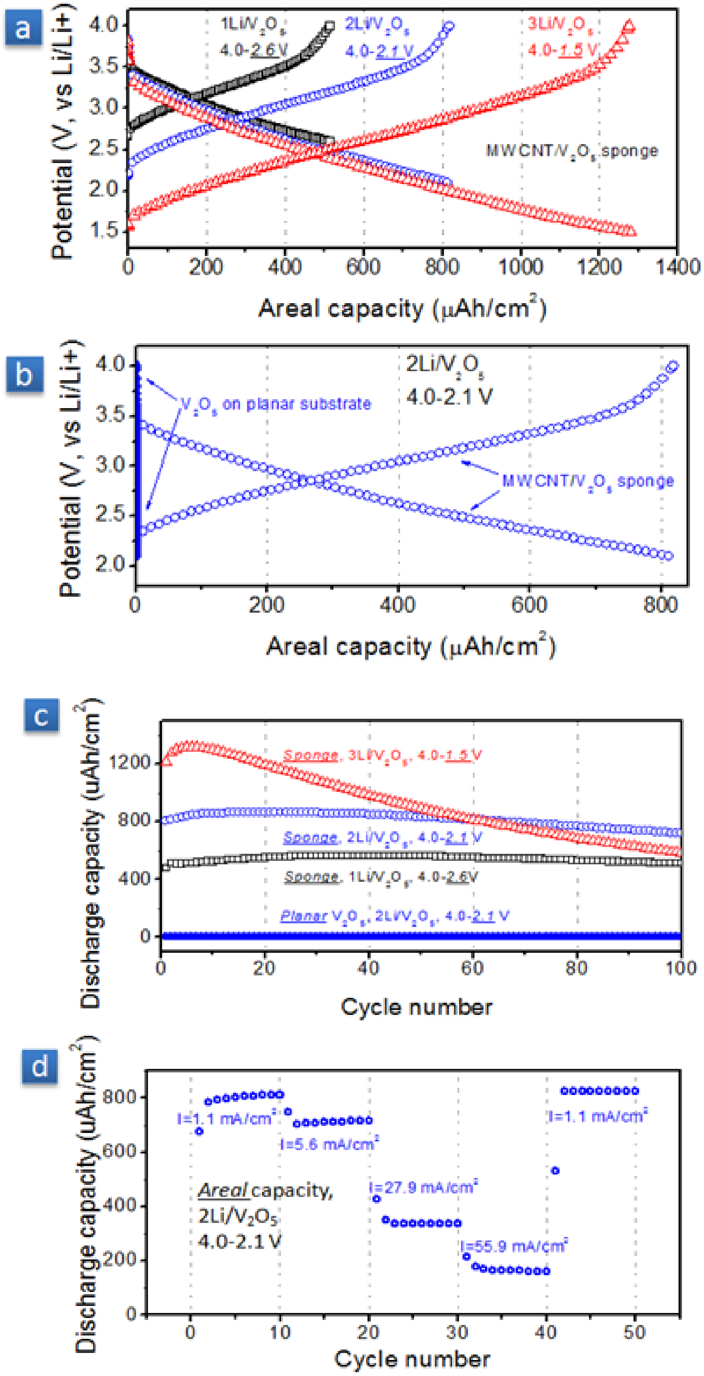

Figure 17: (a) Discharge and charge curves (second cycle) for the cells with MWCNT/V_2O_5 sponge cathodes in three different voltage ranges with 1C current. (b) Discharge and charge curves (second cycle) of the cells with planar and MWCNT/V_2O_5 sponge cathodes in the voltage range for 2Li/V_2O_5 (4.0-2.1 V) with 1C current. (c) Cycling performance and areal capacity comparison between the cell with planar V_2O_5 cathode in the voltage range for 2Li/V_2O_5 (4.0-2.1 V) and the cells with MWCNT/V_2O_5 sponge cathodes in three different voltages with 1C current. (d) Rate capability data for MWCNT/V_2O_5 sponge cathodes in the voltage range for 2Li/V_2O_5 (4.0-2.1 V) at different current densities as indicated in the figure.

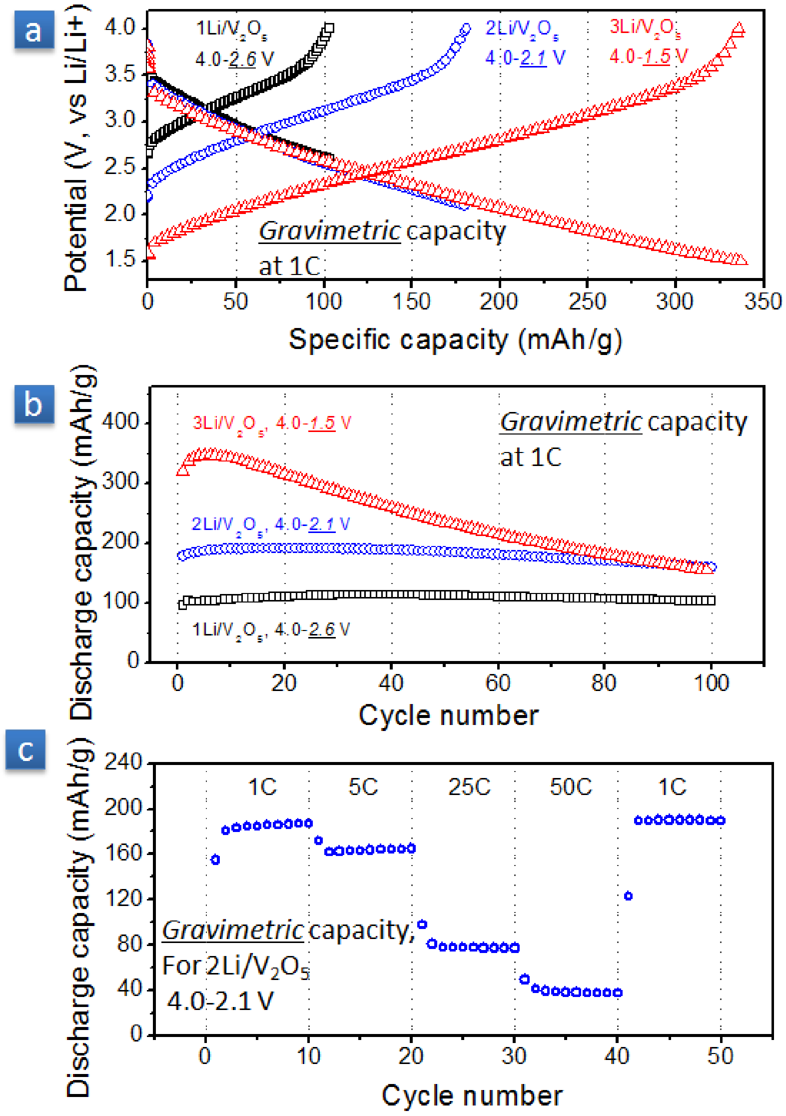

Figure 18: (a) Gravimetric discharge and charge curves (second cycle) for the cells with MWCNT/V_2O_5 sponge cathodes in three different voltage ranges at 1C rate. (b) Cycling performance of the cells with MWCNT/V_2O_5 sponge cathodes in three different voltages at 1C rate. (c) Rate capability data for MWCNT/V_2O_5 sponge cathodes in the voltage range for $2Li/V_2O_5$ (4.0-2.1 V) at different C-rates as indicated in the figure.

Figure 17d shows results from rate capability experiments for the MWCNT/V_2O_5 sponge cathodes upon cycling at different current densities of 1.1, 5.6, 27.9 and 55.9 mA/cm^2 (corresponding to 1C, 5C, 25C and 50C respectively). At each current, the battery was tested for 10 cycles to ensure the reliability of the reported readings. The specific capacity was stable at a constant current rate, while changes in current density resulted in stepwise dependence of the areal capacity. The sponge cathodes were able to provide 90%, 44% and 22% of the initial capacity at 1C rate when the cycling current was increased by 5, 25, and 50 times. When tested at 55.9 mA/cm^2, the areal capacity was 155 µAh/cm^2. The calculated energy densities at 1.1 and 55.9 mA/cm^2 are 2.29 and 0.43 mWh/cm^2, corresponding to power densities as high as 2.29 and 21.7 mW/cm^2 respectively

This rate performance is somewhat better than that previously found for Al nanorods coated with 17 nm ALD TiO_2.[84] There the authors reported 35% capacity retention from C/5 to 20C, while our MWCNT/V_2O_5 sponge showed 44% retention from 1C to 25C. We believe this good rate performance originates from the structure of MWCNT/V_2O_5 sponge, which provides excellent electronic conduction, short charge carrier (both e^- and Li^+) transport path lengths over V_2O_5 layer, and easy access for the electrolyte to the increased surface area.

The gravimetric capacity data of the V_2O_5 in MWCNT/V_2O_5 nanostructured sponge are recorded in Figure 18. The initial specific capacity of the V_2O_5 was 103, 181, and 336 mAh/g when the discharge cut off voltage was set for 3Li, 2Li, and 1Li transfer respectively. Taking the 2Li/V_2O_5 range (4.0-2.1 V) for example, the capacity of V_2O_5 on MWCNT is 181 mAh/g, which is not far away from the thin V_2O_5 on planar stainless steel disk (219 mAh/g, not shown here). This again indicates that most of V_2O_5 on MWCNT was accessible for (de)/lithiation. While a capacity of 181 mAh/g at 4.0-2.1 V is not among highest of the reported values for V_2O_5, it is comparable to that of the well-known $LiFePO_4$ cathode (166 mAh/g) cycled at similar conditions (4.5-2.0 V at 2 C rate).[87] When cycled for $3Li/V_2O_5$ (4.0-1.5V) with 1C rate, the capacity of V_2O_5 on MWCNT (336 mAh/g) is lower than reported value (455 mAh/g) for amorphous ALD V_2O_5 film on planar Ti foil, which was tested at C/10 rate though.[81] For the $1Li/V_2O_5$ (4.0-2.6 V), the capacity of 103 mAh/g reported here is lower than our previous report on crystalline V_2O_5 (130 mAh/g) at the same 1C rate, primarily due to the difference in crystallinity. This also indicates higher capacity would be expected with deposition of crystalline V_2O_5 on MWCNT.[74] The cycling performances for the gravimetric capacities (Figure 18b) are consistent with the areal ones discussed in Figure 17c. The rate performance data in Figure 17c show gravimetric capacities of 181, 163, 80, and 40 mAh/g at current of 1C, 5C, 25C, and 50C, respectively. The highest energy and power density from V_2O_5 delivered here are 453 Wh/kg, and 5000 W/kg. Taking into account that the V_2O_5 mass is 54% of the whole sponge on average and that typical cathode mass is around 40% of a battery, one can make a full battery with energy density of 98 Wh/kg and power density of 1080 W/kg, which support our estimation in Figure 12a and all surpasses the DOE goal for application in hybrid electric vehicles (HEV).[88] In all, these gravimetric results show MWCNT /V_2O_5 sponge is also promising for the applications in LIBs.

We found that the Coulombic efficiency (Figure 19a) for $3Li/V_2O_5$ (4.0-1.5 V) is consistently lower than that for $2Li/V_2O_5$ (4.0-2.1 V), supporting the cycling performance shown in Figure 18c. We performed analysis using electrochemical impedance spectroscopy (EIS) to understand the decay mechanism, with results shown in Figure 19b and c. The spectra were fitted using an equivalent circuit (EC), shown in the inset of Figure 19b. The proposed EC was $R_{sol}(C_{dl}[R_{CT}W])$, where R_{sol} represents the electrolyte resistance, C_{dl} the double layer capacitance and R_{CT} the charge-transfer resistance at V_2O_5-electrolyte interface, which is in serial connection with the Warburg element (W). There are two major changes after 100 cycles for $2Li/V_2O_5$ (4.0-2.1 V) and $3Li/V_2O_5$ (4.0-1.5 V). First, the enlarged semicircle diameter indicates an increase of resistance for charge-transfer at the V_2O_5-electrolyte

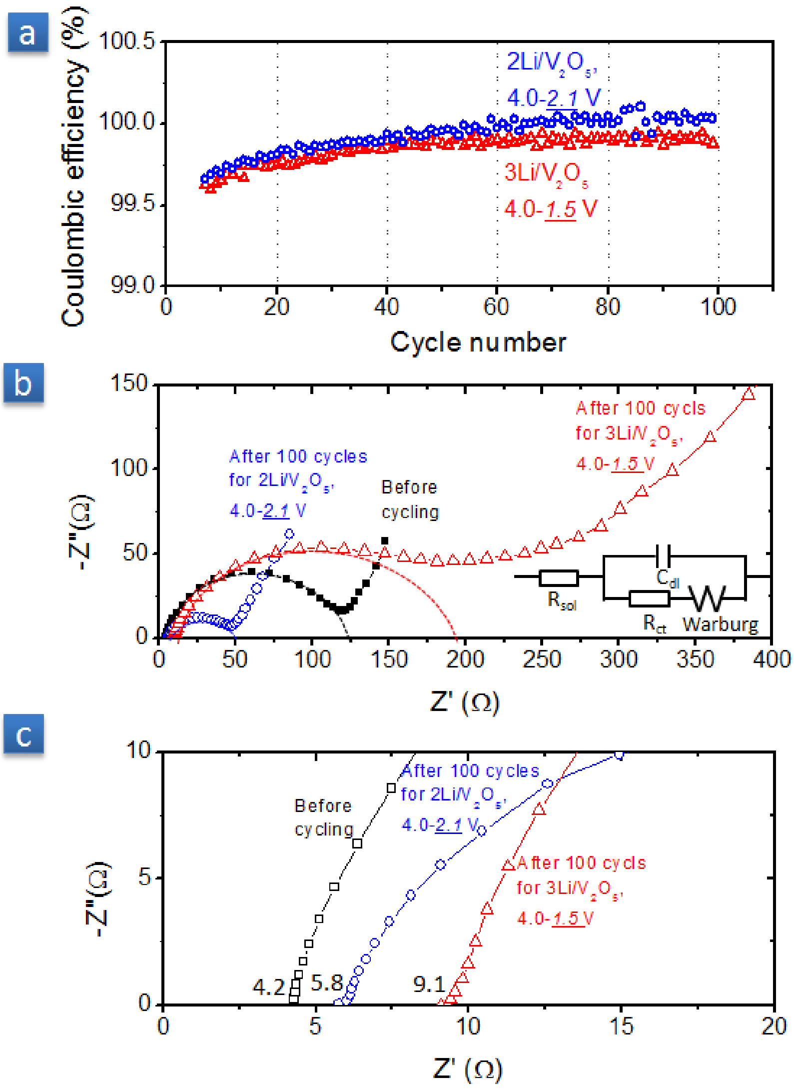

Figure 19: (a) Comparison of Coulombic efficiency for the cells cycled for $2Li/V_2O_5$ (4.0-2.1 V) and $3Li/V_2O_5$ (4.0-1.5 V). (b, c) EIS data collected from the cells with MWCNT/V_2O_5 sponge cathodes before cycling and after 100 charge-discharge cycles for $2Li/V_2O_5$ (4.0-2.1 V) and $3Li/V_2O_5$ (4.0-1.5 V). Inset of (b) shows the equivalent circuit of the cell.

interface when cycled for 3Li/V_2O_5 (4.0-1.5 V), in contrast with a decrease of charge-transfer resistance when cycled for 2Li/V_2O_5 (4.0-2.1 V). This is possibly associated with a higher resistive solid electrolyte interphase (SEI) formation for 3Li/V_2O_5 (4.0-1.5 V). In contrast, the enhanced wetting between electrolyte and electrode after cycling might be responsible for the decrease in charge-transfer resistance for 2Li/V_2O_5 (4.0-2.1 V), where the SEI formation is not significant because of the higher cut-off voltage. Second, the electrolyte resistance, as indicated by the real part of the impedance at high frequencies, has increased from 4.2 to 9.1 Ω when cycled for 3Li/V_2O_5 (4.0-1.5 V), larger than 5.8 Ω for 2Li/V_2O_5 (4.0-2.1 V). This may result from dissolution of active material into electrolyte 3Li/V_2O_5 (4.0-1.5 V), as indicated by previous studies on V_2O_5 based materials,[64, 86] or from consumption of electrolyte during SEI formation.

Finally, we looked at the morphology of the sponge after cycling 3Li/V_2O_5 (4.0-1.5 V) and compared it with that of fresh sponge (Figure 20). No obvious change in the morphology can be observed except that the surface became rough after cycling, probably associated with the SEI formation. More importantly, no uncoated MWCNT exists, demonstrating the stability of the coaxial structure of MWCNT/V_2O_5 upon electrochemical cycling. Therefore, we conclude the decay for 3Li/V_2O_5 (4.0-1.5 V) was primarily caused by the intrinsic property of V_2O_5, but no link to structure failures could be found.

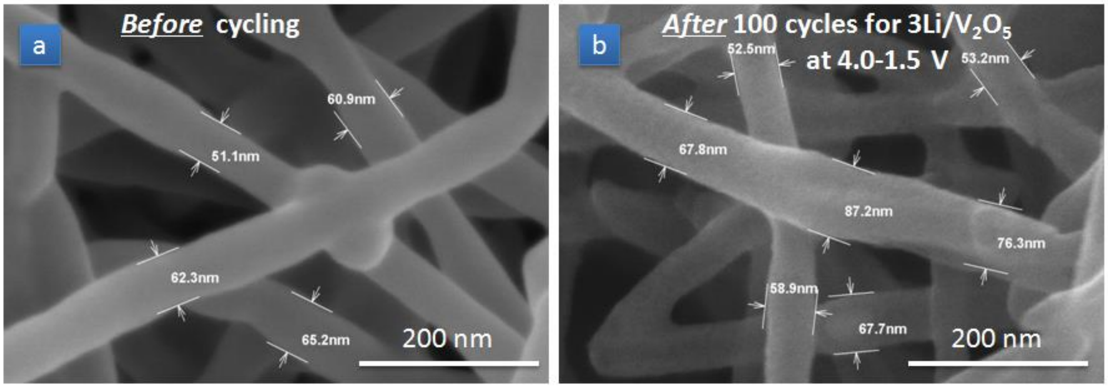

Figure 20: SEM images of MWCNT/V_2O_5 sponge (a) before and (b) after electrochemical test for 3Li/V_2O_5 (4.0-1.5 V) for 100 cycles, showing the stability of the core/shell structure.

4.1.4 Conclusions

We have successfully fabricated MWCNT/V_2O_5 sponges designed for high electrochemical performance. The high surface area of the sponge allows for significant amount of active material loading. Electrons can freely transport through the MWCNTs. The thin uniform layer of V_2O_5 (<16 nm) enables (de)/lithiation in active material within very short time. The high porosity of sponge provides easy access of electrolyte to the active storage material. The MWCNT/V_2O_5 sponge delivered a high initial areal capacity of 1284 µAh/cm^2 for 3Li transfer (4.0-1.5 V), although cyclability was poor. EIS results showed an increase in charge-transfer resistance after cycling, probably due to the dissolution of V_2O_5 and the formation of higher-resistive SEI layer. SEM confirmed that the MWCNT/V_2O_5 core/shell structure, however, was stable after electrochemical cycling. The cycling stability was largely improved using a larger discharge cut off voltage. In the 4.0-2.1 V range for 2Li/V_2O_5, the initial areal capacity was 818µAh/cm^2 at 1C and maintained capacity of 155 µAh/cm^2 with 50C rate, giving a high power density of 21.7 mW/cm^2. We suggest initial application of such sponge cathode primarily for thin film batteries, though other applications to larger energy storage challenges may follow. For larger scale LIBs, the ALD recipe optimization and/or surface functionalization of MWCNT are required for coating larger scale samples efficiently. Overall, this work demonstrates an effective approach to engineer MWCNT with metal oxide coating for high performance electrochemical energy storage.

4.2 V_2O_5/CNT/cellulose fiber paper electrode

4.2.1 Motivations

Paper has been used as the major medium to record and propagate information and knowledge for more than 2000 years. In recent years, the incorporation of advanced nanomaterials and nanotechnologies have allowed scientists to dramatically expand the applications of paper to other fields including micro-fluids,[89, 90] organic electronics,[91-93] solar energy harvesting,[94-99] and electrochemical energy storage.[100-102] The motivations have been very clear - that paper is both low-cost and flexible. The price of paper is about 0.1 cent per dm^2, orders of magnitude cheaper than plastics, glass, metal foil, silicon, and other traditional substrates. In addition, paper is environmentally friendly as it is recyclable and produced from renewable raw materials.

Paper is produced from a dilute suspension of cellulose fibers which is first dewatered, then filtered, pressed, and heated to the final product. Both the raw materials and the production process give paper a hierarchical porosity and rough surface.[103, 104] The porosity has been considered detrimental to some device applications. Materials printed on paper will have a lower conductivity than on plastics, reducing the performance of organic light-emitting diode (OLEDs), solar cells, and other devices that require a controlled nanostructure.[93] When attempting to fabricate flexible field-effect transistors (FET) using cellulose fiber paper as a dielectric layer, researchers found that lower porosity is preferred for higher rectification.[105] In other cases, however, the porosity (and roughness) of paper is advantageous in that it provides good adhesion for printed materials and improves the sensitivity of sensors.[100, 106, 107]

For energy storage devices, porous paper can be used as a separator membrane[108] and electrode substrate.[102, 109-111] So far, there has been limited focus on porosity engineering in paper-based electrodes and on the relation between porosity and electrochemical performance. Pores in solid material fall into three categories: micropores (widths smaller than 2 nm), mesopores (widths between 2 and 50 nm), and macropores (widths larger than 50 nm).[112] In this work, we show that the hierarchical porosity of pristine cellulose fiber paper comprises of micrometer-sized macropores between cellulose fibers and mesopores within individual cellulose fiber (2-8 nm). Particularly, we explore the creation of electrochemical energy storage in paper-based scaffolds and the relative contribution of the mesopores to the storage through two experimental investigations.

4.2.2 Synthesis and characterization

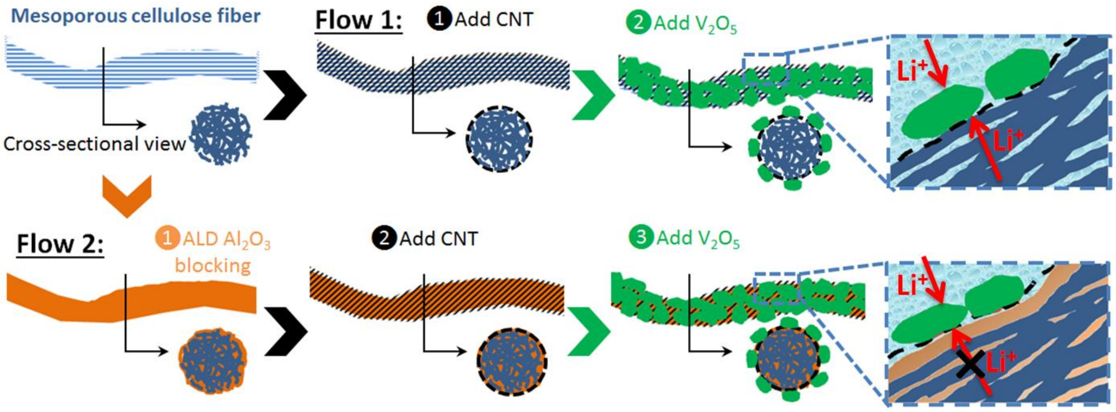

Figure 21. Two experimental flows to fabricate Li-storage paper cathodes. The general route is to functionalize cellulose fibers with highly conductive CNT, and then deposit V_2O_5 for Li-ion storage. The major difference between the flows lies in the modification of the cellulose fibers using 20 nm ALD Al_2O_3. We postulate that the mesopores in the cellulose fiber will contribute to the electrochemical capacity by providing extra paths for Li^+ transport during electrochemical charge/discharge. The addition of the ALD Al_2O_3 blocking layer will close off the mesopores, making these pathways unavailable to electrolyte infiltration.

First, we sequentially functionalize paper with carbon nanotubes (CNT) for electron conduction and ultrafine V_2O_5 nanoparticles for Li storage (Flow 1 in Figure 21). Due to the high electronic conductivity of CNT, short Li^+ diffusion length in V_2O_5 nanocrystals, and hierarchical porosity in paper available for Li^+ transport, a high rate performance (i.e., charge/discharge at high power) was successfully achieved on the V_2O_5/CNT/cellulose cathode. In the control experiment represented by Flow 2 in Figure 21, we intentionally blocked the mesopores of cellulose fiber with 20 nm Al_2O_3 by atomic layer deposition (ALD) before adding CNT and V_2O_5. This blocked cathode scheme is designated as a V_2O_5/CNT/blocked cellulose cathode. The blocked cathode exhibits noticeable reduction in rate performance, attributed to the loss of Li^+ transport paths through the cellulose mesopores. Our results indicate that the mesoporosity in the individual cellulose fibers is critical for paper-based electrochemical energy storage devices to achieve high rate performance, i.e., fast energy storage and high power output.

The morphology of the cellulose fiber after CNT and V_2O_5 functionalization is shown in Figure 22a-22c at various magnifications. In the low magnification SEM images in the inset of Figure 22a, the micrometer scale macroporosity can be clearly seen in the pristine cellulose fiber network. The macroporosity remains intact after CNT wrapping and V_2O_5 deposition. Dip coating the cellulose fiber paper in CNT ink

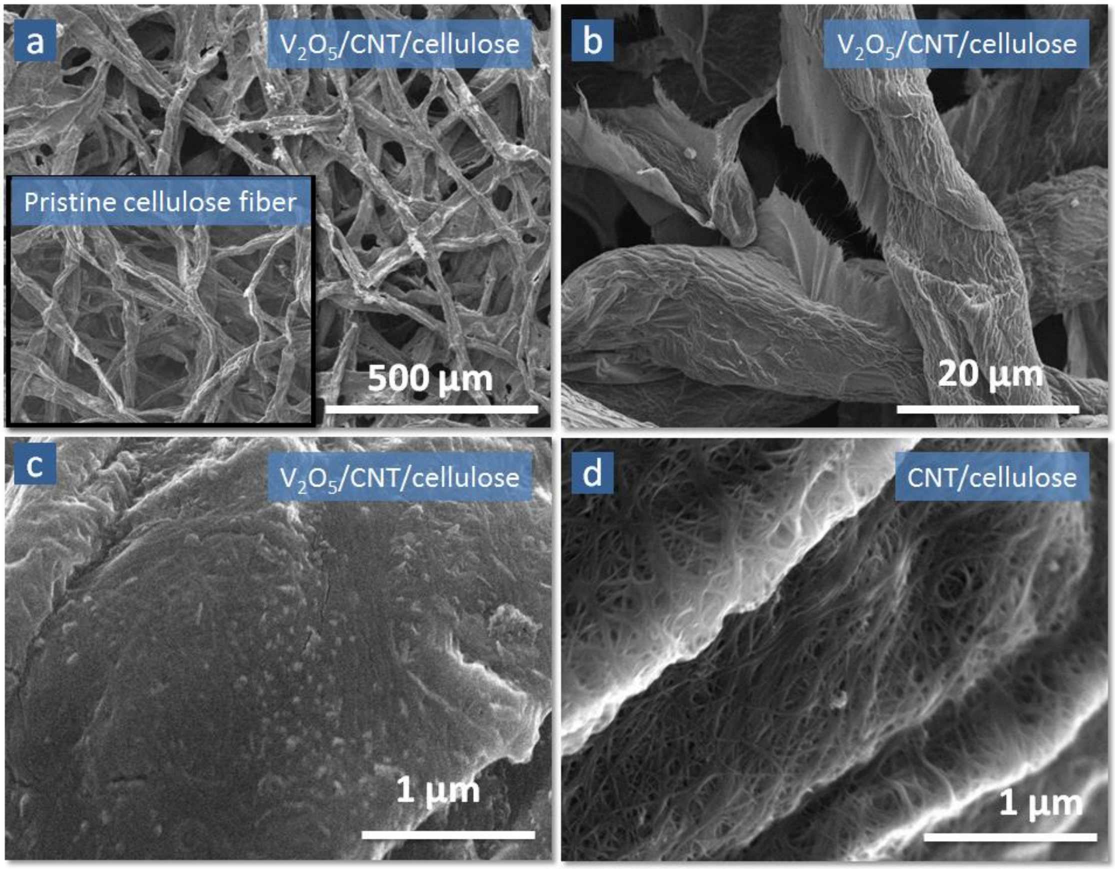

Figure 22. SEM images of (a-c) cellulose fiber after CNT wrapping and V_2O_5 nanoparticle deposition. These SEM images represent the structure presented in the upper right part of Schematic 1. Inset of (a) shows pristine cellulose fiber as a reference. (d) SEM image of CNT wrapped cellulose fiber before V_2O_5 deposition as a reference to (c).

adds conductivity, the sheet resistance after coating is 30 Ω/□. Higher magnification images (Figure 22b and 22d) show that the conformal CNT network extends between individual fibers, contributing to the high conductivity of the paper. The V_2O_5 nanocrystals are deposited using a newly reported ALD process using ozone as the oxidant.[113] For this process, V_2O_5 deposition starts with nucleation at a limited number of sites on a substrate, followed by nanocrystal growth. On Si substrates the nanocrystals form ~10 nm thick layer after 500 ALD cycles. In a similar way in this work, the CNT network deposited on the cellulose scaffold is expected to produce a low density of hydroxyl groups, leading to an aggregation of V_2O_5 nanocrystals only a few nanometers in size. The high magnification SEM image for V_2O_5/CNT/cellulose (Figure 22c) shows that the CNT surface is just buried in a new layer and some nanoparticles are visible.

Cross-section SEM images of and EDS element maps V_2O_5/CNT/cellulose samples are presented in Figure 23. Within the elemental map, the C signal originates from the cellulose fibers and CNT, and O signal comes from both cellulose fiber and V_2O_5. The V signal uniquely indicates the V_2O_5 regions. Vanadium is uniformly distributed on the outer surface of the fiber as expected as V_2O_5 deposition is the final step in the sample preparation.

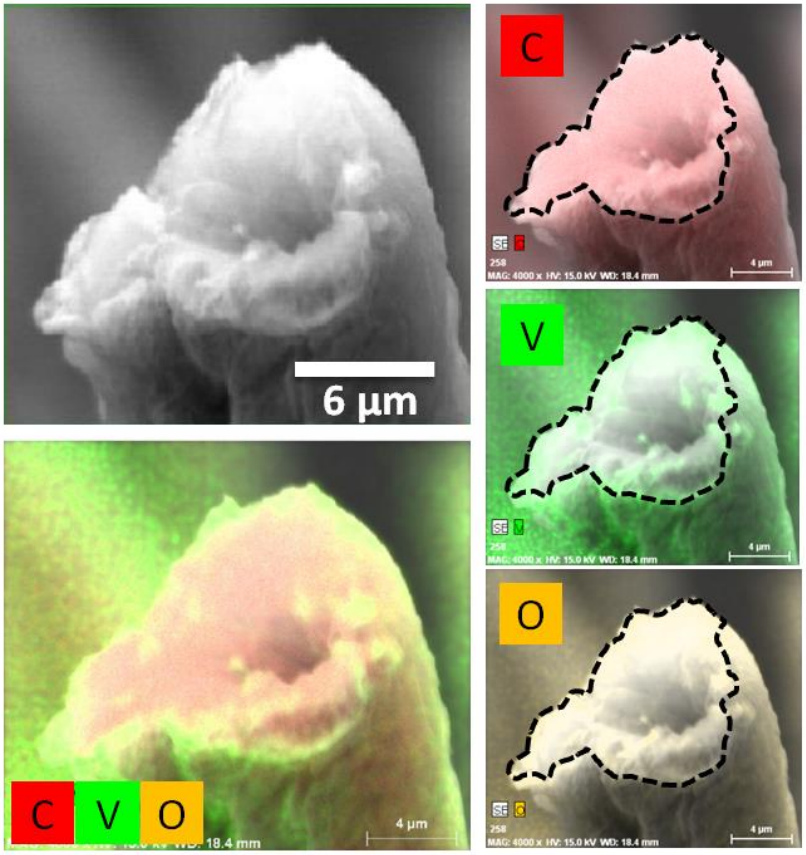

Figure 23. Cross-sectional SEM and EDS mapping of a single V_2O_5/CNT/cellulose fiber (corresponding to upper right panel in Schematic 1). The V_2O_5 is pesent on the outer surface of the CNT/cellulose fiber. The dashed line indicates the V_2O_5 and CNT/cellulose fiber interface.

4.2.3 Electrochemical performance

The electrochemical performance of the paper-based electrodes is evaluated in Li half cells using standard liquid electrolyte and Li metal anode. Figure 24a compares the charge storage capability of CNT/cellulose with and without V_2O_5 deposition in the voltage range of 4.0-2.1 V. With the same current density of 23 µA/cm^2, the discharge time of the CNT/cellulose was 360 s, indicating that some charge was stored. Lithiation of CNTs can only occurs below 2.0 V,[114] the stored charge for

CNT/cellulose, therefore, is attributed to double layer capacitance of the CNTs. Adding the V_2O_5 increases the discharge time of the CNT/cellulose to 5030s, indicating a much larger charge storage capacity. The bare capacity of the CNT/cellulose sample is only ~7% of that with V_2O_5. Furthermore, the V_2O_5 should somewhat reduce the available capacity of the CNT since V_2O_5 partially covered the CNT surface. It can be concluded that the charge storage contribution of V_2O_5 in V_2O_5/CNT/cellulose represents at least 93% of the total capacity.

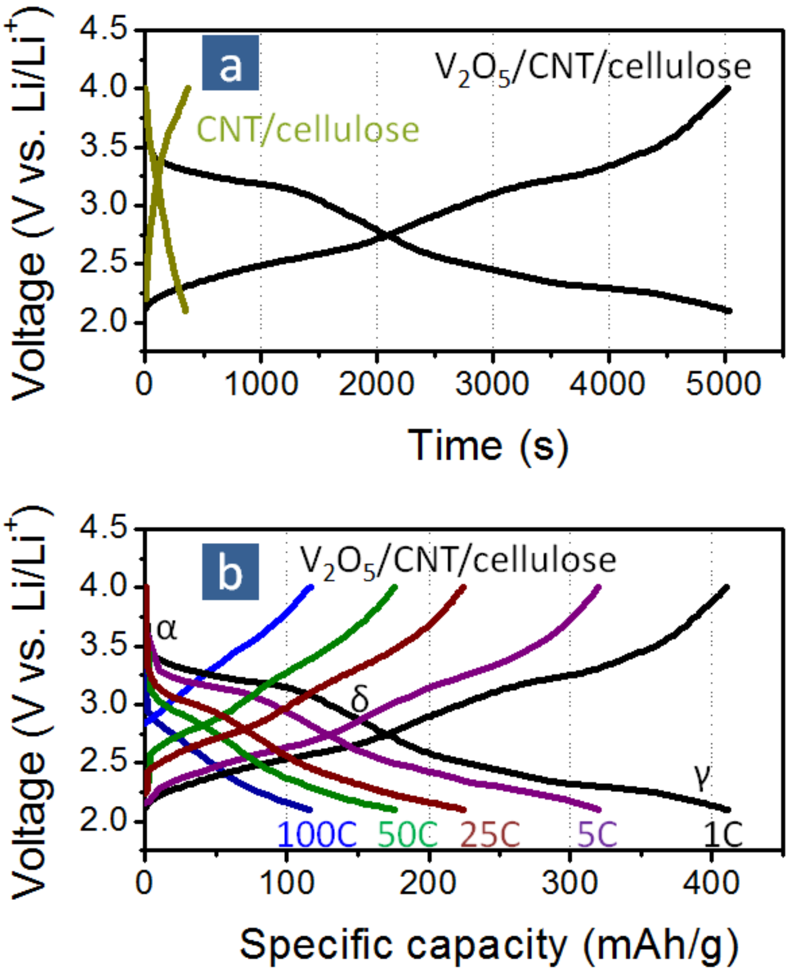

Figure 24. (a) Galvanostatic charge/discharge curves of cells composed of CNT/cellulose fiber cathodes with and without V_2O_5 at a current density of 23 $\mu A/cm^2$. (b) Galvanostatic charge/discharge curves of cells with V_2O_5/CNT/cellulose fiber cathodes at current rates ranging from 1C to 100C. The phase change of V_2O_5 with respect to degree of lithiation degree is marked on the graph.

The galvanostatic charge/discharge curves of the V_2O_5/CNT/cellulose cathodes at various C rates are presented in Figure 24b. A rate of n C corresponds to a current density of 294×n mA/g, or an expected full charge or discharge cycle in 1/n hours. Two voltage plateaus are observed on both the discharge and charge curves, representing the characteristic phase transformation of α-δ-γ, as marked in the graph.[115] At 1C rate, the measured specific capacity of V_2O_5 is 411 mAh/g, much higher than the theoretical value of 294 mAh/g for this voltage range. It is not uncommon for nanostructured V_2O_5 materials to achieve a higher capacity than the theoretical value because of a high surface to volume ratio. In a similar V_2O_5/CNT system, Sathiya et al. reported an experimental capacity of 850 mAh/g at 4.0-1.5 V for a theoretical capacity of 441 mAh/g.[116] The extra capacity can be attributed to contributions from surface double layer capacitance and/or excess Li storage capacity at surface defect sites in the electrode material.

The electrochemical performance of the V_2O_5/CNT/cellulose cathodes at higher C rates is plotted in Figure 24b. At 5C, 25C, 50C, and 100C, the calculated capacities are 321, 225, 177, and 116 mAh/g, respectively. This rate performance is among the highest reported for V_2O_5-based high rate cathodes. Chen et al. found mesoporous V_2O_5 to have a capacity of 87 mAh/g at 56C.[117] Cao et al. reported 120 mAh/g at 70C from a V_2O_5 nano electrode,[118] and the V_2O_5-based high rate cathode reported by Lee et al. delivered 102 mAh/g at 96C.[119] The excellent rate performance reported here - comparable or better than the others - can be attributed to three unique features in our cathode samples. The first is the high electronic conductivity of the CNT coated paper (30 Ω/□), allowing for fast electron transport to the V_2O_5. Second, the thin V_2O_5

nanocrystal layer significantly reduces the Li^+ diffusion time. McGraw et al. reported the Li diffusivity D in crystalline V_2O_5 over the $2Li/V_2O_5$ voltage range as from 5×10^{-14} to 2×10^{-12} cm^2/s.[120] If we take an intermediate value of 1×10^{-13} cm^2/s, the kinetic equation $\tau = L^2/2D$ implies a Li diffusion time in a 10 nm film of 5 seconds (corresponding to 720 C). Most importantly, the paper-based electrode scaffold features a hierarchical porous structure, which is well suited for rapid Li^+ transport through the liquid electrolyte to V_2O_5.

4.2.4 Role of mesoporosity

Computational modeling has indicated that ion depletion near the electrolyte/electrode interface during electrochemical cycling will limit battery performance.[121] Experimentally, the porosity engineering in electrochemical energy storage nanomaterial electrodes has been studied in several material systems. Rinzler et al. reported that by creating macroporosity in the CNT/RuO_2 supercapacitor electrode system, the specific capacitance nearly doubles.[122] In the development of Au electrodes for supercapacitors, Robinson et al. found that pores on the order of several hundred nm's are favored for ion transport. Incorporating these pores achieves a high power density without sacrificing energy density.[123] Similar advances in macroporosity engineering have been made with regards to graphene frameworks for high energy and high power supercapacitors.[124] Introducing macroporosity into electrodes improves ion transport, alleviates ion depletion, and increases the charge/discharge rate; properties desired for high power devices. Macroporosity exists in our composite cathodes between the cellulose fibers as an artifact of the paper fabrication process. We regard the porosity as a major contribution to the high rate performance we observe.

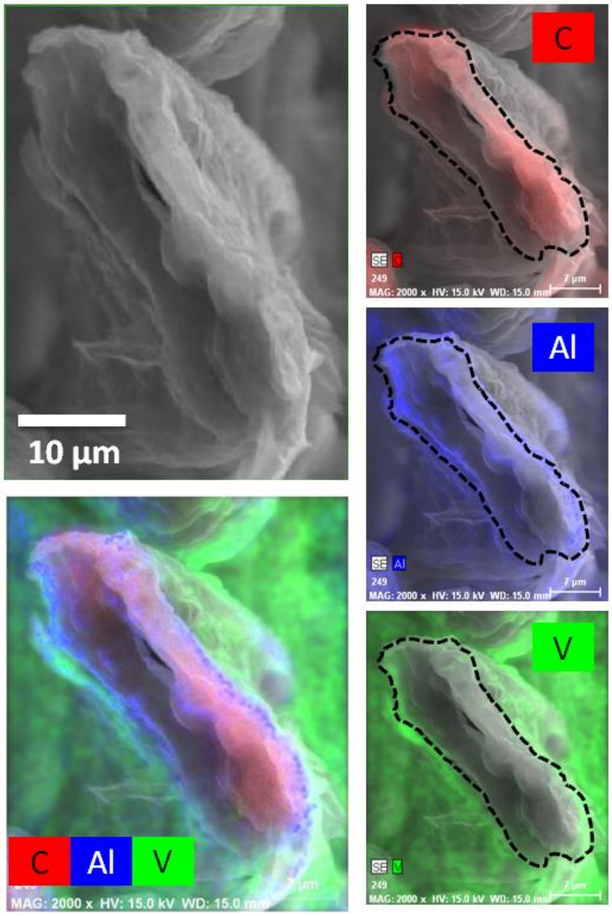

Figure 25. Cross-sectional SEM and corresponding EDS maps of the V_2O_5/CNT/Al_2O_3 blocked cellulose fiber (bottom right panel in Schematic 1), exhibiting well-defined elemental distributions of C, Al, and V. The dashed line indicates the V_2O_5 and CNT/ blocked cellulose fiber interface.

The effect of fiber mesoporosity on the electrochemical performance is investigated by comparing the performance of the as-prepared samples with ones designed to block the mesopores while maintaining macroporosity. Traditional porosity engineering methods, i.e., coating or laminating with polyethylene (PE), polypropylene (PP), PET, wax or other additives will only block the macropores.

Instead, we utilize an ALD coating of Al_2O_3, an electrochemically inert material. ALD is a low temperature growth method that alternates sequentially pulsed precursor doses, creating a self-limiting adsorption/reaction process for each precursor with monolayer precision. This results in superb conformality for demanding nanotopography and high-aspect ratio nanostructures.[15] ALD is therefore employed as a technique to precisely tune pore size in nanomaterials.[125-127]

We ensure that the ALD precursors reach and deposit on the inner surface of the mesopores by increasing the precursor pulse time by a factor of 8 over what is traditionally used for planar film deposition. Figure 25 is an SEM image and EDS map of the cross section of a blocked cellulose fiber after CNT and V_2O_5 functionalization as represented in Schematic 1. The SEM shows the cross-section to be elongated from top left to bottom right. The EDS overlays on the SEM images clearly show a C-Al-V layered structure, indicating that Al_2O_3 deposited on the cellulose fiber surface prior to CNTs and V_2O_5. This structure corresponds to the one illustrated in the bottom right panel of Figure 22.

Figure 26a shows the effect of the ALD Al_2O_3 coating on the pore size distribution of cellulose fibers calculated from Brunauer-Emmett-Teller (BET) measurements. For the pristine cellulose fiber, the majority of pore sizes range from 2-8 nm, the mesoporous regime. The addition of the ALD blocking layer causes a distinct shift in the pore size distribution. The majority of the mesopores disappear from the distribution. The few remaining 2-4 nm pores may be due to very small surface cracks generated by the large temperature changes during the porosimetry measurements. The effect of ALD blocking is also strongly reflected by the BET surface area change – the surface area for the pristine mesoporous cellulose fiber is 11.2 m^2/g while that for the ALD Al_2O_3 coated cellulose fiber is only 0.07 m^2/g.

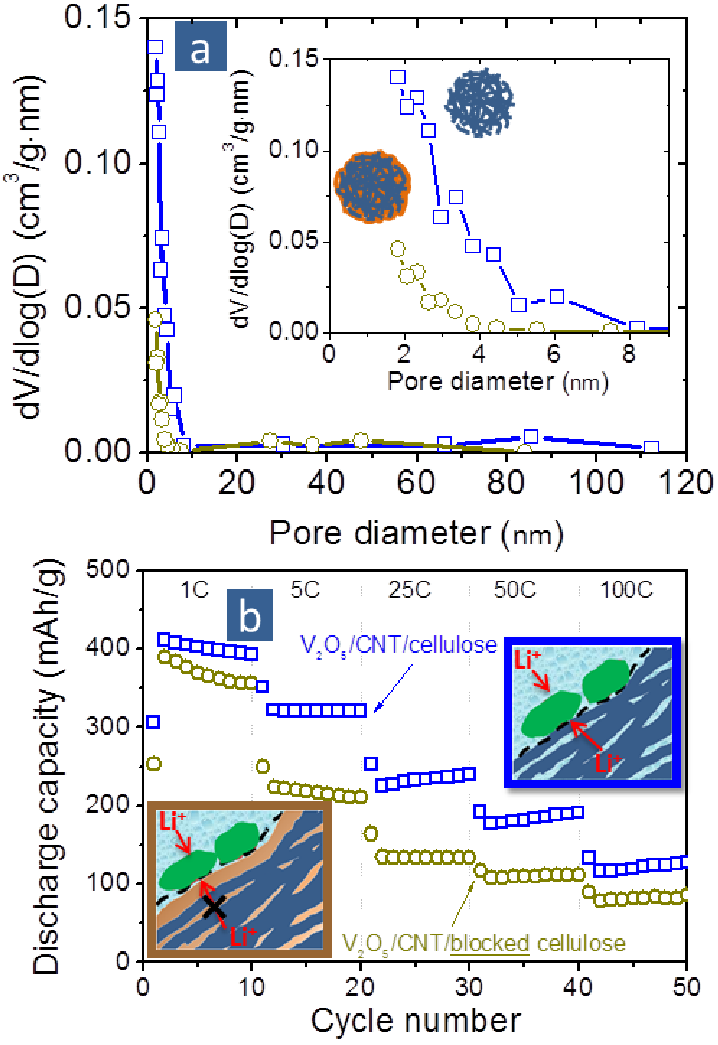

Figure 26. (a) Pore size distribution of the cellulose fiber with (circles) and without (squares) the 20 nm ALD Al_2O_3 coating. (b) Rate performance profiles of the Li-storage paper cathode with (circles) and without (squares) the ALD Al_2O_3 coating.

We examined the rate performance of the composite electrodes using pristine mesoporous and ALD-blocked cellulose fibers as substrates. The data presented in Figure 26b shows that the capacity of the unblocked sample is significantly higher than that of the blocked cellulose, especially at higher rates (5C-100C). For the V_2O_5/CNT/blocked cellulose, the second cycle discharge capacities are 390, 224, 134, 108 and 77 mAh/g for rates of 1C, 5C, 25, 50C, and 100C, respectively. The capacity ratios for using mesoporous cellulose fiber relative to the blocked cellulose fiber are 1.05 at 1C, 1.43 at 5C, 1.68 at 25C, 1.62 at 50C, and 1.50 at 100C (blue square over brown circle in Figure 26b). The minimal capacity difference at 1C is likely due to the fact that the slow rate allows Li^+ to completely transport to the V_2O_5 surface. At higher rates (e.g. 5C-100C), Li^+ intercalation into V_2O_5 benefits from the additional ion transport channels in the mesoporous fibers channels which are blocked by the ALD layer in the control sample. We conclude that ion transport is the dominant factor at 5C-100C, and the mesoporosity inside the cellulose fiber significantly enhances ion transport to the active material to achieve higher capacity values.

4.2.5 Conclusions

In our effort to understand mesoporous structure for fast electrochemical energy storage, we fabricated V_2O_5/CNT/cellulose fiber cathodes which exhibit excellent rate performance. Such composite cathodes derive high electronic conductivity from CNT, short Li^+ diffusion lengths and correspondingly rapid diffusion from nanocrystalline V_2O_5, and fast ion transport from the hierarchical porosity. To quantify the role of mesporosity of the fibers, we compared the results to a control sample in which a 20 nm ALD Al_2O_3 layer was first applied to block electrolyte access to the mesopores. Porosimetry measurements revealed a significant decrease in the accessible mesoporosity and surface area of the celloluse fibers after the ALD coating. The specific capacity of V_2O_5 at 1C was not affected by the ALD blocking layer; only at rates above 5C did the blocking layer cathode experience a ~30% reduction in capacity. From these results we regard ion transport in the electrolyte as the rate-determining mechanism for total achievable capacity. This work clearly indicates that mesopores within a cellulose fiber act as an electrolyte reservoir and provide extra paths for Li^+ transport. The use of porous, electrochemically inert paper as a substrate sacrifices some volume energy and power density, however it provides efficient utilization of active storage materials at high rates. Our high-rate paper-based cathodes can be applied in stationary energy storage technologies to efficiently manage smart grid and as well as energy from renewable sources.

4.3 Nanoporous anodic aluminum oxide (AAO) templated 3D electrodes

4.3.1 Motivation

AAO membranes have been widely used as templates in a variety of nanotechnology applications without the need for expensive lithographical techniques. It is made from the anodization of aluminum, an electro-chemical process that changes the surface chemistry of the metal, via oxidation, to produce an anodic oxide layer. During this process a self-organized, highly ordered array of cylindrical shaped pores can be produced with controllable pore diameters, periodicity and density distribution. The reader is referred to the following review, which gives a full account of AAO processes and the various applications of nanotechnology that use them in the manufacture of nano-materials and devices.[128]

This research aims to take several of AAO's advantages, including high surface area, aligned and ordered pores with large and controllable open volume, mechanical support. We use symmetric AAO templates called "Unikera" that are commercially available from Synkera. These templates are uniquely designed to have same pore diameter from both sides, as compared to the traditional commercial "Whatman" AAO templates which have a branched side with much smaller pore diameter. The symmetric templates allow electrode fabrication from both sides.

The available geometry of the templates shows various pore diameters, pore periods and template thicknesses. Our priority choice is the template with 150 nm diameter with 243 nm pore period, $2 \cdot 10^9/\text{cm}^2$ density, and 50 um thick. The template with 367 nm pore period will allow pore-widening to obtain larger pores than 150 nm if we need thicker electrode materials. The pore-widening strategy has been shown very significant in engineering the nanocapacitors by Dr. Lauren Haspert in our group.[129] These commercial templates will provide unique flexibility and reproducibility in our device designs.

4.3.2 Current collectors – ALD TiN and Ru

Titanium nitride (TiN) has become a standard electrode for both industry and research applications. For energy storage, TiN is used as a current collector because it is stable and inert to Li intercalation.[130] Several processes have been developed to deposit this material using a variety of metal organic and oxidant precursors.[131, 132] The resistivity of TiN films prepared from ALD vary from 50 to 8000 $\mu\Omega \cdot \text{cm}$, depending on Ti precursors, N sources, and processing temperatures.[132]

We employ the Fiji ALD system from TiN deposition, which is capable to perform both thermal and plasma-enhanced ALD (see Appendix). Both ALD process are done at 250°C and give growth rate of about 0.5 Å/cycle, but their conductivity varies significantly. At the thickness of 20 nm, the plasma process produces high quality TiN films with resistivity of 400 $\mu\Omega \cdot \text{cm}$, while the TiN films from thermal process are 2.4×10^5 $\mu\Omega \cdot \text{cm}$. This is probably due to the high impurity of O and C in the films from thermal process.[132] We choose the plasma process for depositing current collector in the AAO template.

The surface morphology of the AAO template before and after the plasma TiN process is shown in Figure 27 a and b. It is noticeable that the pore size deceases but all pores remain completely open after 30 nm TiN deposition. In order to investigate the conformality of the plasma TiN deposition into AAO, we sputtered Au for mechanical support, dissolved the AAO template in 3 M NaOH solution, and then observed free-standing TiN nanotube array in SEM (Figure 27c). These nanotubes are about 600 nm in length, presenting a deposition with aspect ratio of 4:1 (600 nm depth in 150 nm wide pore). This conformality is not idea for our purpose; in the 50

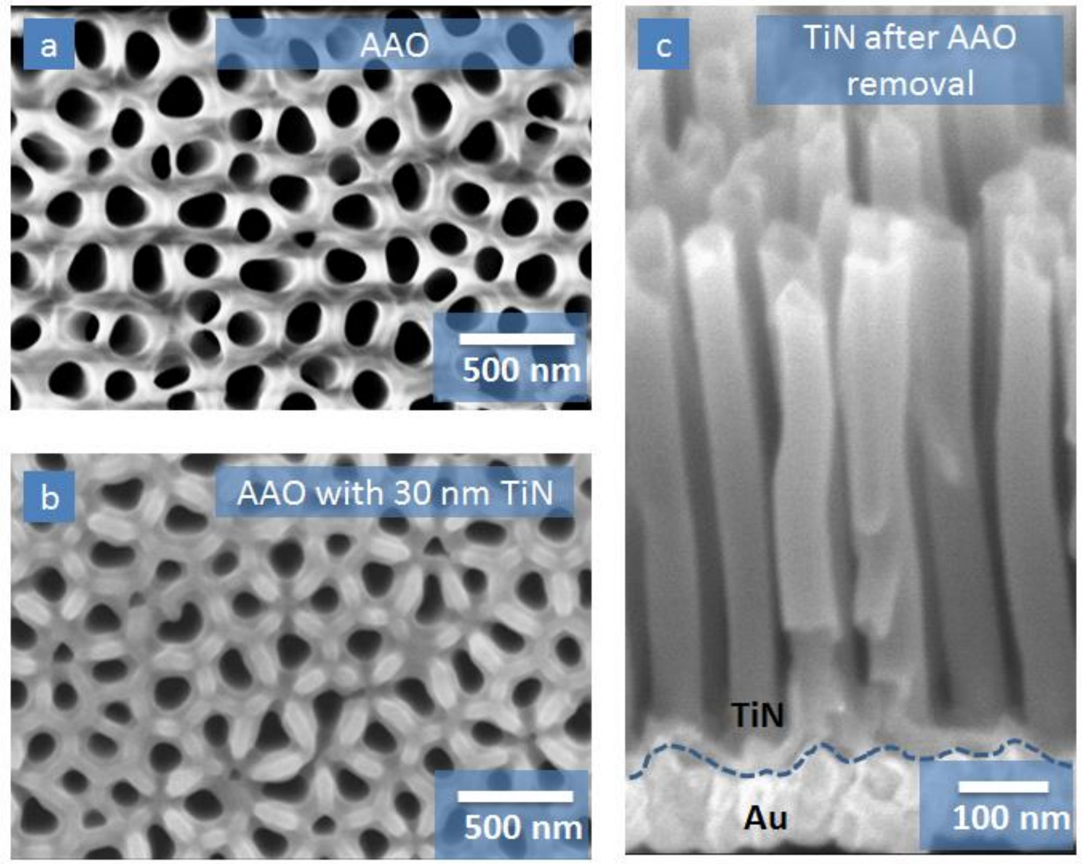

Figure 27: SEM images of AAO template (a) and (b) after 15 nm TiN deposition by plasma-N_2 process. (c) is the cross sectional SEM image of TiN nanotube arrays. The TiN coated AAO was first coated with sputtered Au for mechanical supported and is then dissolved in 3M NaOH sulotion.

µm thick template, we need the current collector to penetrate into at least a few µm deep in order to utilize the inner surface area. Such poor conformality is common for plasma process since the lifetime of N plasma is short, due to collision and diminishment on the nanopore wall.

For electrode materials, ruthenium is of particular interest, because of its high work function (4.7 eV), low bulk resistivity (7 μΩcm), and, for some applications, its conducting oxide phase (RuO_2).[133] These electrodes are used in high-aspectratio random access memory devices (RAM),[134] gate metal in metal–oxide–semiconductor field-effect transistors (MOSFET), a glue layer for CVD-grown and electrodeposited copper films,[135] and gas-sensing nanostructures.[136] Ru has also been shown to force TiO_2 films grown on it into the high-K rutile phase, making it attractive for capacitor applications.[137]

We developed the Ru ALD process with a home-built furnace system (see Appendix), according to our previously reported work on Ru ALD.[133] The process is done at 300 ^{o}C with Cypus and O_2. The growth rate is about 0.4 Å/cycle. The as-deposited Ru film with 12 nm thick shows a resistivity of 25 μΩcm, just a little higher than bulk Ru (10 μΩcm). We also performed deposition of Ru into AAO template and the conformality was studied with two methods. First, we dissolved the AAO template in 3M NaOH, ultrasonicated it in acetone, and then prepared sample for TEM imaging. From Figure 28b, we can observe nanotubes in length from 5-18 µm. These nanotubes also showed continuous wall, which indicate that the Ru has formed continuous films, not just nanoparticles in nucleation stage. This is favored for us to gain a good current collecting effect. We also performed EDS mapping, shown in Figure 28 d,e and f. It is clearly that Ru signal exists mainly in top 15 µm of the 50 µm thick template, in line with what we see in the TEM images. This conformality is preferred because it enables us to fabricate battery in a nanopore – we will have two electrodes from each side (15 µm) and insulating region in the middle (20 µm).

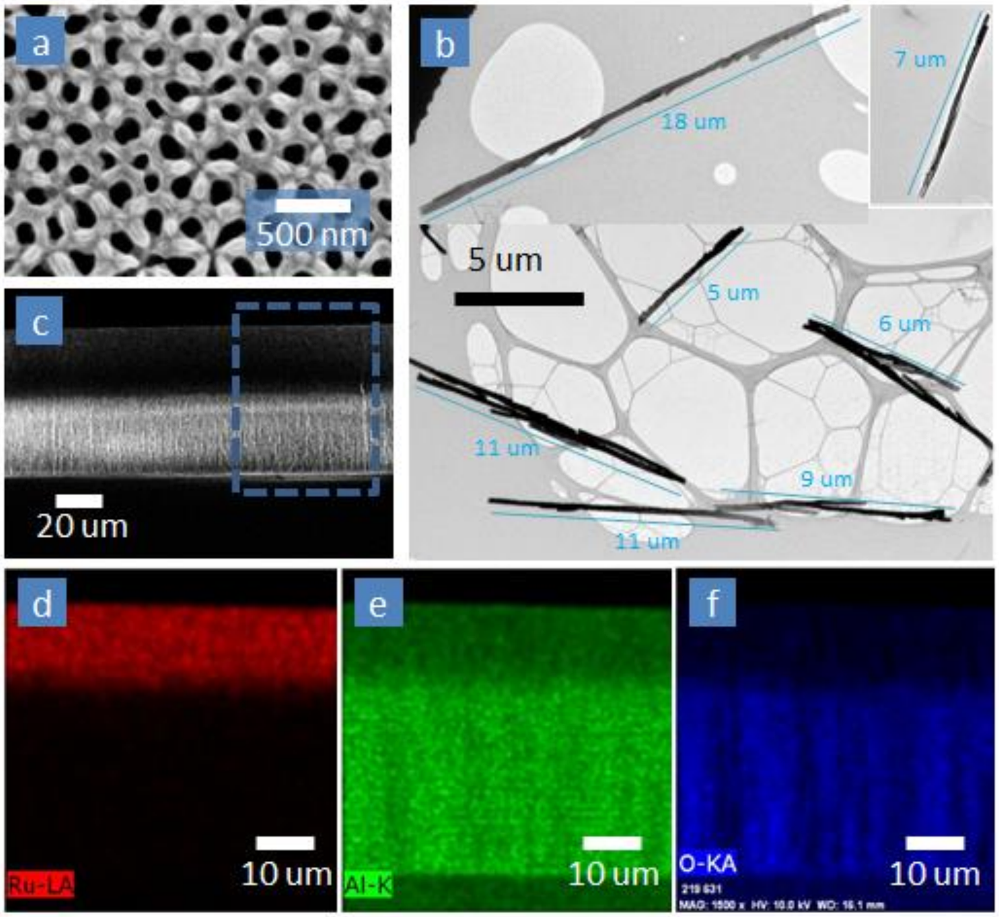

Figure 28: (a) SEM image of AAO surface after deposition of 12 nm Ru metal. (b) TEM images of Ru nanotubes after removal of AAO template. (c) Cross-sectional view of the Ru-coated AAO template. The bright area indicates the insulating part due to electron charging. (d, e, and f) EDS mapping of Ru, Al, and O, corresponding to the dashed line area indicated in c. The mapping shows clearly that Ru is deposited into top 15 µm of the AAO template.

4.3.3 Fabrication and structure characterizations

The experimental flow of fabricating well-aligned nanopore electrode array is shown in Figure 29. We first add a conductive layer for collecting current, or distributing electrons. After that, a Li-storage layer, crystalline V_2O_5 in this case, is deposited. We employ ALD for both layers because high confomality films can utilize the inner surface area of AAO and ALD has unprecedented capability for accurate thickness control. The rationale for the thickness of each layer is as following. The current collector layer should be as thin as possible to leave space for

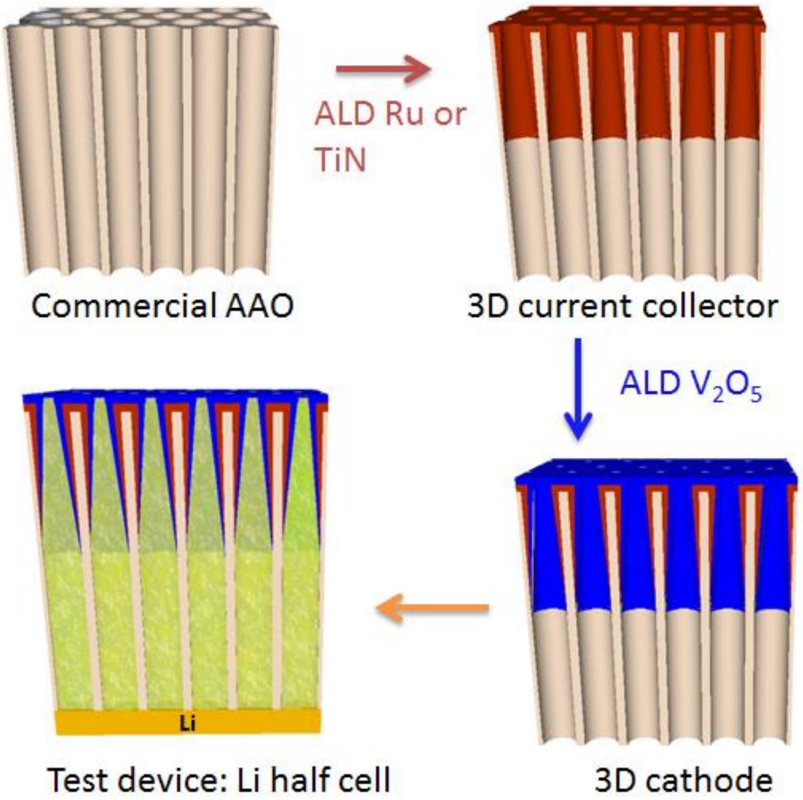

Figure 29. Schematic showing the flow of AAO templated electrode fabrication. Pristine AAO template is first coated with an electric conductive layer and then with Li-storage layer. Both layer are done by ALD with controlled conformality and thickness. The template is assembled in Li half cell for electrochemical tests.

Li-storage layer and electrolyte in the pore, as long as it is thick enough to provide good conductivity. We chose 10-30 nm as the target for current collector layer here. For Li-storage layer, we need to balance the amount of active materials (prefer thick films) and the remaining space for electrolyte (prefer thin films). We choose 20 nm for V_2O_5, leaving 50-90 nm pore for electrolyte. After the fabrication of the 3D electrode, we put the template on a stainless steel disk for mechanical support and assemble them into a lithium coil cell. The thin layer of V_2O_5 is also favorable for electron conduction from stainless steel disk to current collector layer.

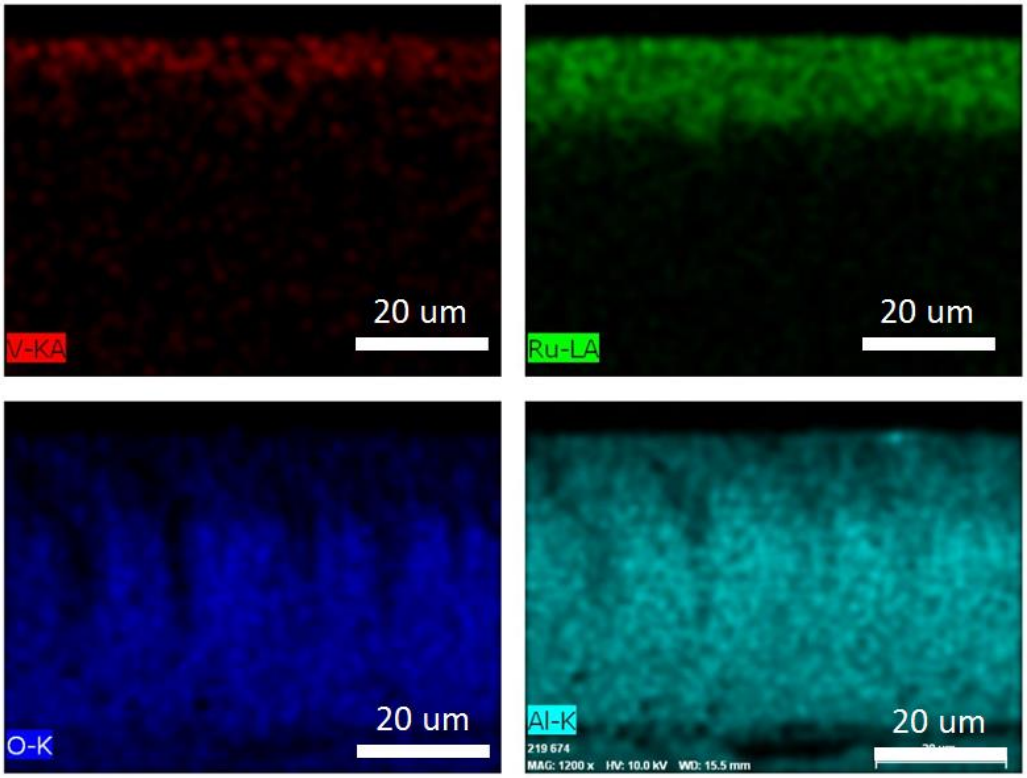

Figure 30. EDS mapping of the cross-section on a V_2O_5/Ru/AAO sample, showing Ru deposition about 15 µm, and V_2O_5 deposition of 5-10 µm.

After the electrode fabrication, we investigate the structure using EDS. Figure 30 shows that V_2O_5 and Ru successfully grow into the AAO templates, with penetration depth of 5-10 µm and 15 µm respectively. V_2O_5 conformality could be further improved by extending the pulse and purge time in the recipe, but we keep the V_2O_5 deposition more shallow than Ru to make sure V_2O_5 can get electrons easily during electrochemical cycling.

4.3.4 Electrochemical performance

The as-made templates were put against a stainless steel disc and compressed in a Li cell. To investigate the effect of current collector, we cycled the cell at current of C/2 based on the mass of V_2O_5. A control experiment without any current collector was also performed. Data presented in Figure 31 a shows that current collector has a huge effect of the capacity of V_2O_5. The sample with Ru current collector (25 µΩ·cm resistivity, 15 µm deep) shows the largest capacity of 184 mAh/g, much higher than 42 mAh/g for the one with TiN current collector (400 µΩ·cm resistivity, 0.6 µm deep). Without any current collector, we only see 4 mAh/g capacity of V_2O_5. This is because the stainless steel disc surface is rough and can only transport electrons to the partial of surface V_2O_5 on the template. With current collector, electrons can transport through the thin layer of V_2O_5, 20 nm in this case, and distribute through the conductive layer beneath. Apparently, a high conformal and low resistive current collector is favored for V_2O_5 to present high capacity.

We notice that the capacity of V_2O_5 with Ru as current collector is even larger than the theoretic value of 147 mAh/g in the voltage range of 4.0-2.6 V. It is necessary to check if the current collector inside the nanopore has some capability for charge storage. We tested the Ru/AAO structure only and find that the stored charge corresponded to 60 mAh/g of V_2O_5. Since Ru metal is inert to lithiation, and the surface native RuO_2 only show some Li storage at voltage below 2V, we attribute the stored charge as the surface double layer capacitance inside the confined nanopores. The contribution of bulk V_2O_5 film is then calculated to be 124 mAh/g.

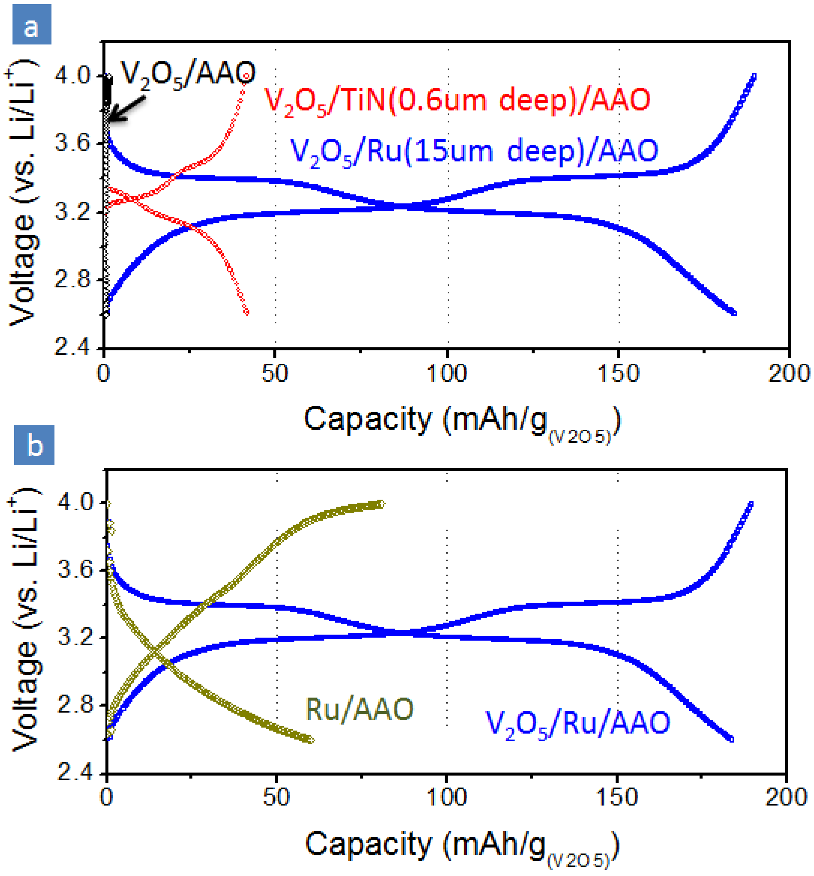

Figure 31: (a) Second charge/discharge curve of the Li cells with cathodes made of V_2O_5/AAO, V_2O_5/TiN/AAO, and V_2O_5/Ru/AAO. Current rate is set at C/2 (74mA/$g_{(V2O5)}$). Conductivity and conformality of current collector is shown to be critical to electrochemical performance. (b) Second charge/discharge curve of the Li cells with cathodes made of Ru/AAO, and V_2O_5/Ru/AAO. The current is the same for both sample, the stored charge is calculated into V_2O_5 capacity by normalizing the mass of V_2O_5.

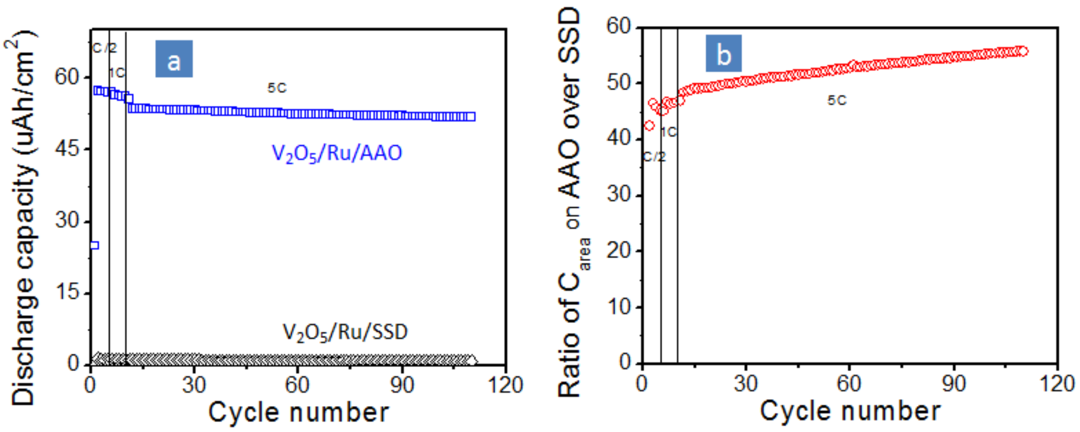

Figure 32: (a) Areal capacity comparison of V_2O_5/Ru/AAO 3D electrode and V_2O_5/Ru/stainless steel disc planar electrode at C/2, 1C and 5C with extended 100 cycles. (b) Ratio of areal capacity of V_2O_5/Ru/AAO 3D electrode over V_2O_5/Ru/stainless steel disc planar electrode at C/2, 1C and 5C with extended 100 cycles.

We also compared the areal capacity of the V_2O_5/Ru/AAO 3D electrode and V_2O_5/Ru/stainless steel disc planar electrode. At C/2, the areal capacity of V_2O_5/Ru/AAO 3D electrode is 57.3 µAh/cm^2, 42.5X of that for planar electrode (1.3 µAh/cm^2). The areal capacity enhancement is even larger at higher rate of 1C and 5C with 44.9 and 46.8 respectively. This means the rate performance of V_2O_5/Ru/AAO 3D electrode is higher than the planar electrode. During 100 cycles at 5C, the enhancement keeps increasing from 46.8 to 55.8, showing a better cycling stability of 3D electrode over planar electrode. Anyway, this areal capacity enhancement (42.5-55.8X) is significantly higher than other designs using 3D micro-channels (20-30X)[80], free standing Al nanorods (10X)[84] and bio-templated nanowire forest (~ 8X).[85] Conceptually, the further enhancement can be achieved by improving the conformality of V_2O_5 since Ru deposition is deeper than V_2O_5 (15 µm vs. 5-10 µm).

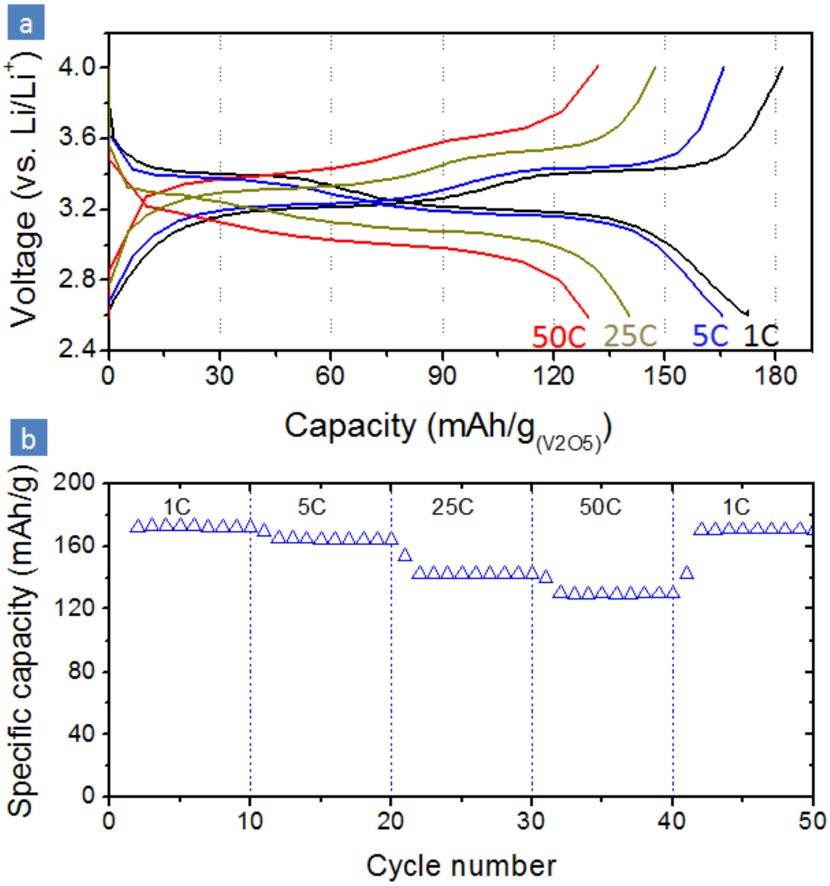

Figure 33: (a) Second charge/discharge curve of the Li cells with cathodes made of V_2O_5/Ru/AAO at 1C, 5C, 25C, and 50C. (b) Rate capability data for V_2O_5/Ru/AAO cathodes in the voltage range for $2Li/V_2O_5$ (4.0-2.1 V) at different C-rates as indicated in the figure.

Since data shown in Figure 32 indicated the rate performance of the V_2O_5/Ru/AAO 3D electrode is even better than that of planar electrode, we further tested the rate performance at higher C rate of 25C and 50C. The second charge/discharge curves are shown in Figure 33 a, where the characteristic plateaus can be observed for all cases, through more obvious for slower rate. The over potential is also larger for higher C rates. The second charge/discharge capacity at each C rate is 173, 165, 142, and 130 mAh/g at 1C, 5C, 25C, and 50C respectively. Again, as we discussed above, that the capacity at 1C and 5C is larger than theoretic value (147 mAh/g) can be explained from the extra double layer capacitance in the confined nanopore geometry. Most interestingly, we can achieve high capacity at high rate of 50C, 88% of theoretic value, in this unique aligned nanopore structure. We attribute the excellent rate performance to high conductive and conformal current collector, thin layer of V_2O_5 for Li diffusion, easy migration of electrolyte in the nanopore.

We also tested the electrochemical stability of the V_2O_5/Ru/AAO electrode with long cycle life of 1000 times at 5C rate, shown in Figure 34. After 1000 cycles, the capacity retained at 127 mAh/g, which is 78% of its initial capacity. The realistic meaning of such electrode is it can retain 78% of its capacity after about 3 years if it is fully discharge and charge every day. The Coulombic efficiency maintained higher than 98.8% for 1000 cycles.

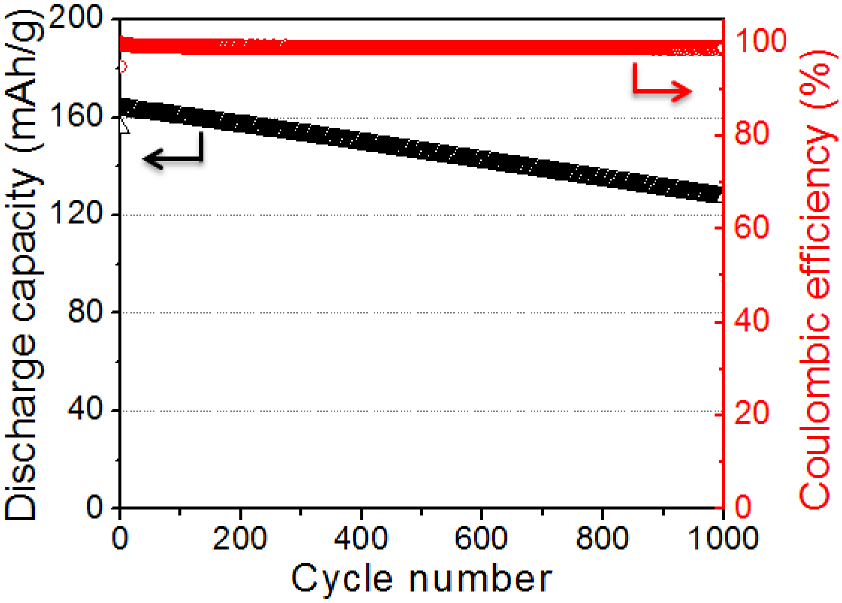

Figure 34: (a) Cycling performance and (b) Coulombic efficiency of V_2O_5/Ru/AAO cathodes at 5C rate.

4.3.5 Conclusions

In this section, the approach of fabricating high density, well-aligned nanopore electrode is described. ALD TiN and Ru are employed for depositing current collector into AAO nanopres, followed by ALD V_2O_5 for Li-storage. The conformality and conductivity are found to be critical for the capacity of V_2O_5. Due to ALD's controlled conformality and the high inner surface area of AAO template, such electrode demonstrates 42.5-55.8X areal capacity than planar electrode, an improvement higher than most of the state-to-art strategies in the literature. The V_2O_5/Ru/AAO electrode also demonstrate ultra-high rate performance with 88% of its theoretic value at 50C rate, and excellent cycliabilty with 78% retention after 1000 cycles.

Chapter 5: Conclusions and outlook

5.1 Summary

The motivation of this dissertation is using ALD to design and fabricate nanostructured electrodes/devices with improved electrochemical energy storage capability, particularly high rate performance. We employ ALD as a deposition method for Li-storage material mainly for two reasons. First, ALD typically grows thin films with precisely controlled thickness, which is desired for high rate Li-storage since Li diffusion takes short time in thin films. Second, ALD has unprecedented conformality, which is also controllable, to utilize high surface area of nanostructured templates.

The first part of this work is the development of ALD processes for V_2O_5, a rationally selected high capacity cathode material. A new and fully optimized process using O_3 as oxidant has been found to produce crystalline films with generally higher capacity, comparing to the amorphous films from the traditional H_2O-based process. The electrochemical performance of ALD films is found to be superior to that of most of other methods in the literature. This part serves as the foundation of the dissertation, and enables the fabrication of novel nanostructured electrode.

In order to achieve high rate performance in electrochemical energy storage devices, three critical issues need to be addressed: electron conduction, Li diffusion, and Li^+ migration. These issues have been investigated in several structures separately listed in Table 2. The Li diffusion has been found to be a limit step in crystal V_2O_5 thin film electrodes for high rate performance, suggesting an up limit of about 60 nm for V_2O_5 films. The conductivity and conformality of current collector largely affects the capacity of V_2O_5 deposited in high density well-aligned AAO templates. The mesopores in the cellulose fiber is found to serve as an electrolyte reservoir and provide extra Li^+ paths for the paper electrode to achieve high rate performance. Thin film electrodes and AAO templated electrodes are good candidates for future microbatteries and the paper electrodes can be potentially used for flexible energy storage devices and stationary energy storage. The MWCNT/V_2O_5 sponge electrodes features low density of scaffold, high conductivity, thin storage films, high porosity, and thus demonstrates 5X higher power density than state-to-art LIBs.

Table 2. Summary of electrodes and their features studied in this dissertation.

Electrodes	**Features**
V_2O_5 thin film electrodes	-Identified the role of Li diffusion -Capacity/theoretic value at 50C: 56% -Application: thin film batteries
AAO-templated nanopore electrodes	-Identified the role of current collector -Capacity/theoretic value at 50C: 88% -Application: microbatteries
Cellulose fiber paper electrodes	-Identified the role of Li^+ migration -Capacity/theoretic value at 50C: 60% -Application: flexible batteries and stationary energy storage
MWCNT/V_2O_5 sponge electrode	-Capacity/theoretic value at 50C: 14% -Application: high power portable Li ion batteries

5.2 Impact and future work

This work demonstrates a new ALD process for V_2O_5 with excellent electrochemical properties. Besides the thin film electrodes, AAO-templated electrode, paper-based electrodes, MWCNT sponge electrodes, this new process has also enabled a couple of other novel studies. Prof. Reza Ghodssi's group from UMD has implanted this new ALD process into the TMV-based hierarchical microbattery electrodes, and Fabry-Perot platform to study electrochemical reaction-induced stress/strain in V_2O_5 films. Prof. Sarah Tolbert's group has used the ALD V_2O_5 coating on porous ITO electrode for high performance pseudocapacitors.

This work has explored the role of electron conduction, Li diffusion, and Li^+ migration in various electrode systems, and contributes to the development of next generation electrochemical energy storage devices.

Some suggestions for future works. First, the ALD V_2O_5 mechanism can be studied in the new ALD system (Fiji from Cambridge Nanotech) with by-product analysis capability. Second, our group is continuing the work to fabricate full battery into the AAO template. Based on the success construction of V_2O_5/Ru/AAO electrode, we will add an anode material on the other side of the template. Si and TiO_2 are the candidates for the anode and will be deposited by CVD and ALD with some process optimizations. Third, it will be interesting to investigate the role of tortuosity in electrode/separators when devices are cycled at high current. An example is to compare the rate performance of a standard electrode when Celguard polymer separator (high tortuosity) or well-ordered AAO template (low tortuosity) is used as separator.

5.3 Resulting publications

The following publications are the direct output from the work of this dissertation.

1. **Xinyi Chen**, Ekaterina Pomerantseva, Keith Gregorczyk, Reza Ghodssi and Gary Rubloff*, *"Cathodic ALD* V_2O_5 *Thin Film for High-rate Electrochemical Energy Storage"*, ***RSC Advances*** 3, 4294 (2013)
2. **Xinyi Chen**, Hongli Zhu, Yu-Chen Chen, Yuanyuan Shang, Anyuan Cao, Liangbing Hu*, and Gary W. Rubloff*, *"MWCNT/*V_2O_5 *Core/Shell Sponge for High Areal Capacity and Power Density Li-Ion Cathodes"* ***ACS Nano***, 6(9), 7948, (2012) (Most read papers, cited by 5 times by March 28, 2013)
3. **Xinyi Chen**, Ekaterina Pomerantseva, Parag Banerjee, Keith Gregorczyk, Konstantinos Gerasopoulos, Reza Ghodssi, and Gary Rubloff*, *"Ozone-based Atomic Layer Deposition of Crystalline* V_2O_5 *Films for High Performance Cathodes in Rechargeable Li-ion Batteries",* ***Chemistry of Materials***, 24(7), 1255 (2012) (Cited by 11 times by March 28, 2013)
4. Ekaterina Pomerantseva, Konstantinos Gerasopoulos, **Xinyi Chen**, Gary Rubloff, and Reza Ghodssi*, *"Electrochemical Performance of the Nanostructured Biotemplated* V_2O_5 *Cathode for Lithium-ion Microbatteries"* ***Journal of Power Source***, 206, 282 (2012)
5. Parag Banerjee, **Xinyi Chen**, Keith Gregorczyk, Laurent Henn-Lecordier, and Gary W. Rubloff,* *"Mixed Mode, Ionic-electronic Diode Using Atomic Layer Deposition of* V_2O_5 *and ZnO Films"* ***Journal of Materials Chemistry,*** 21, 15391 (2011)

The following publication is enabled by the work of this dissertation.

1. Konstantinos Gerasopoulos, Ekaterina Pomerantseva, Matthew McCarthy, Adam Brown, Chunsheng Wang, James Culver, and Reza Ghodssi* "*Hierarchical Three-Dimensional Microbattery Electrodes Combining Bottom-Up Self-Assembly and Top-Down Micromachining"***ACS Nano,** 6(7), 6422 (2012)

The following publications are in preparation and/or under review.

1. **Xinyi Chen** et al. *"Role of Mesoporosity in Cellulose Fiber for Paper-Based Fast Electrochemical Energy Storage",* ***Journal of Materials Chemistry A***, under review.
2. Xiaogang Han, Yunhua Xu, **Xinyi Chen** et al. *"Reactivation of Dissolved Polysulfides in Li-S Batteries Based on Atomic Layer Deposition of Al2O3 in Porous Carbon Cloth",* ***Nano Energy,*** in revision.
3. Keith Gregorczyk, **Xinyi Chen** et al. *"Atomic Layer Deposition Of* RuO_2*: New Process Development and Fabrication of 3D MWCNT/RuO2 Negative LIB Electrodes"*, ready for submission.
4. Iris Rauda, **Xinyi Chen** et al. *"High-Performance Pseudocapacitors Based on Atomic Layer Deposition of* V_2O_5 *onto conductive Nanocrystal-Based ITO Mesoporous Scaffolds"*, draft done.

Appendix: Experimental section

This section describes the details of material preparation and characterization methods and instruments.

1. *Material preparations*

MWCNT sponge synthesis: MWCNT sponges were synthesized by chemical vapor deposition (CVD) using 1,2-diclobenzene as the carbon source and ferrocene as the catalyst. Ferrocene powder was dissolved into 1,2-diclobenzene to make a solution with concentration of 0.06 g/mL. Then the source solution was injected into a 2-inch quartz tube housed in a CVD furnace by a syringe pump at a constant feeding rate of 0.13 mL/min. The carrying gas is a mixture of Ar and H_2, at a flowing rate of 2000 and 300 mL/min, respectively. Quartz slides were used as the growth substrate to deposit nanotubes in the center of furnace at a set reaction temperature of 860 ^{o}C. Typically we set the growth time to be 4 hours to obtain bulk sponge samples with thicknesses of about 8-10 mm. The sponge was then cut into desired size before ALD coating.

Conductive paper preparation: 170 mg native cellulose fiber disintegrated from southern yellow pine is added to 340 ml distilled (DI) water and stirred with IKA RW20 digital at 700 RPM for ~20 mins. A uniform fiber suspension was obtained and vacuum filtered through Buchner funnels with fritted discs, forming a wet sheet within 3 mins. The sheet is dried in an oven at 100 ^{o}C for ~5 mins, producing a sheet of paper with a typical thickness of 280 μm. The whole process is water based and additive free. The CNT ink is prepared by adding 10 mg single wall CNTs (P3 SWCNT from Carbon Solutions) to 10 ml DI water with 1% 4-Dodecylbenzenesulfonic acid (SDBS), followed by an 8 minute sonication and centrifugation. The concentration of the CNT ink is 1 mg/ml. The paper sheet is dipped in the CNT ink for 2-3 min and dried in oven at 100 ^oC for 15 mins. This procedure is repeated three times to achieve a sheet resistance Rs = 30 ohms/sq as measured by a four point probe station. The conductive paper is finally washed with DI water to remove any residual surfactants and dried in a 100 ^oC oven.

ALD V_2O_5: The ALD V_2O_5 coating was done using BENEQ TFS 500 reactor with a 2 mbar base pressure. $VO(OC_3H_7)_3$ was used as the vanadium precursor, which was kept at 45 ^oC with a vapor pressure of 0.29 torr. VTOP pulse is controlled with ALD valves, which first introduce N_2 to the precursor supply vessel through an upstream ALD valve, and then deliver the headspace gas through a downstream ALD valve. Deionized water and ozone were used as the oxidizing agent in ALD V_2O_5 process. A MKS O3MEGA™ ozone delivery subsystem was employed to supply a stable 18 wt% of O_3 from pure O_2 source. The temperature for H_2O-based ALD was set at 120 ^oC and the O_3-based ALD at 170 ^oC. For the thin film electrode study in Chapter 3, all films were grown with 0.5 s VTOP pulse, 1 s N_2 purge, 2 s O_3 pulse and 1 N_2 purge. In the batch for ALD coating on MWCNT, both a Si wafer (with 2 nm native SiO_2) and a stainless steel disk were put in the reaction chamber. The Si wafer was used for thickness measurement. The stainless steel disk was used as the substrate and current collector for control planar V_2O_5 film, which was tested later as the cathode to compare with the sponge cathodes. All films were grown with extended H_2O-VTOP recipe for 1000 cycles, each being 2 s VTOP pulse, 2 s N_2 purge, 4 s H_2O pulse and 4 N_2 purge. The V_2O_5 coating on cellulose fiber was based on the standard O_3-VTOP recipe for planar film for 500 cycles.

ALD Al_2O_3 on cellulose fiber: The Al_2O_3 was deposited on Beneq TSF 500 using trimethyl aluminium [TMA, $Al(CH_3)_3$] and DI water as precursors at 150 ^oC. The pulse time for the TMA and DI water cycles are intentionally extended from the standard 250 ms to 2 s in order to improve the conformality of Al_2O_3 within the mesopores. The thickness of the ALD Al_2O_3 deposited on a Si wafer after 200 cycles is 20 nm.

ALD TiN and Ru: TiN was deposited using the commercial Fiji tool from Cambridge Nanotech. The deposition was done at 250 ^oC with 0.2 s Tetrakis(dimethylamido)titanium [TDMAT] pulse, 5 s Ar purge, 30 s plasma N2 pulse and 5 s Ar purge . ALD Ru was done with a home-made furnace reactor at 300 ^oC. The metal-organic Ru precursor, bis(2,6,6-trimethyl-cyclohexadienyl)ruthenium,

Figure A1: (a) Beneq TSF 500 ALD system for V_2O_5 and Al_2O_3, (b) Cambridge Nanotech Fiji ALD system for TiN, (c) Home-made furnace system for Ru deposition.

$Ru(C_9H_{13})_2$ (or ‘Cyprus’, Air Liquide), was loaded into a Strem electropolished stainless-steel bubbler and maintained at 80°C. Ar was flowed through the bubbler at 100 sccm. Research grade O_2 (99.999%, Praxair) was used as the co-reactant and was flowed at 300 sccm. Timed Swagelok ALD valves controlled the dose for both precursors. One optimized ALD cycle consisted of the following pulse/purge sequence; 5s $Ru(C_9H_{13})_2$ pulse, 5s Ar purge, 5s O_2 pulse, 5s Ar purge.

2. *Material characterizations*

Structural characterizations: XRD was done on a Bruker D8 Advance system with LynxEye PSD detector and Ni β-filter using CuKα radiation (step size 0.02^o in the range of $14^o < 2\theta < 32^o$). The morphology was investigated by a Veeco multimode AFM with nanoscope III controller where Si was used as substrate. SEM was done in Hitachi SU-70 SEM with EDS. TEM was performed with a JEOL 2100F field emission system with EDS. Raman was performed in a Horiba Jobin-Yvon LabRAM HR-VIS MicroRaman system with an internal 632.8nm laser source. Thermogravimetric analysis (TGA) was carried out in a TGA Q500 from TA Instruments. The X-ray Photoelectron Spectroscopy (XPS) surface chemistry analysis was done in a custom integrated ultra-high vacuum system equipped with SPECS surface analysis units and a Veeco ion gun with a 3 cm ion source.

Li Battery Assembly and Testing: The electrochemical properties of the V_2O_5 films were studied in standard coin cells (CR2032). All films used for electrochemical testing were grown directly on stainless steel disks. The mass of the active material was determined by weight measurements with a high precision microbalance (Mettler Toledo, XS105 dualRange, 1 μg resolution) before and after V_2O_5 deposition. Coin cells were assembled in an Ar-filled glove box with Li metal as a counter electrode and 1M $LiPF_6$ solution in ethylene carbonate/diethyl carbonate (EC/DEC, 1:1 by volume) as electrolyte. An Arbin BT-2000 multichannel battery test station was used for galvanostatic life cycle and rate capability experiments. EIS data was collected from a Bio logic VMP3 using the EC-lab software.

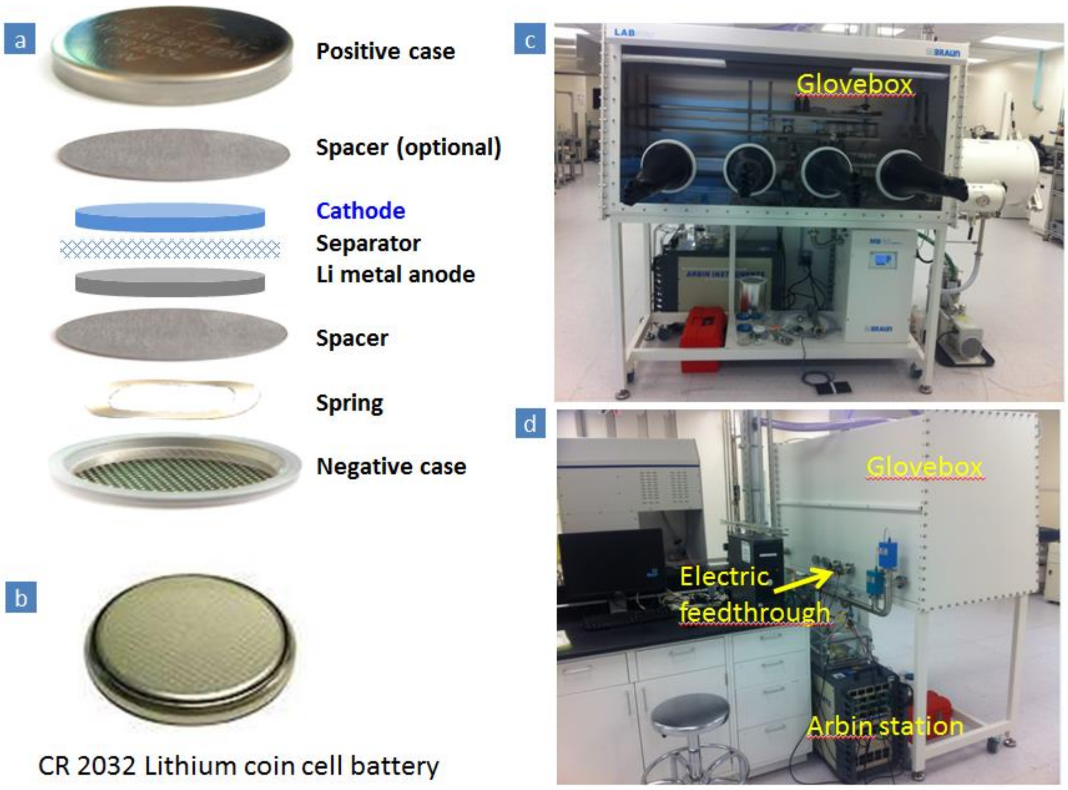

Figure A2: (a) Inner configuration of a coil cell Li battery, (b) Photograph of CR2032 Li coil cell battery, (c) Front view and (d) back view of Ar-filled Mbrown Glovebox for coil cell assembly. Electrode prelithiation was done by constructing coil cell insde glovebox without sealing, which was connected to test station through the electric feedthrough.

References

1. Moriarty, P. Honnery, D. What is the global potential for renewable energy? *Renewable & Sustainable Energy Reviews* **2012**, *16*, 244-252.
2. Goodenough, J. B. Kim, Y. Challenges for Rechargeable Li Batteries. *Chemistry of Materials* **2010**, *22*, 587-603.
3. Tarascon, J. M. Armand, M. Issues and challenges facing rechargeable lithium batteries. *Nature* **2001**, *414*, 359-367.
4. Palacin, M. R. Recent advances in rechargeable battery materials: a chemist's perspective. *Chemical Society Reviews* **2009**, *38*, 2565-2575.
5. Law, M.;Goldberger, J.Yang, P. D. Semiconductor nanowires and nanotubes. *Annual Review of Materials Research* **2004**, *34*, 83-122.
6. Banerjee, P.;Perez, I.;Henn-Lecordier, L.;Lee, S. B.Rubloff, G. W. Nanotubular metal-insulator-metal capacitor arrays for energy storage. *Nature Nanotechnology* **2009**, *4*, 292-296.
7. Liu, R. Lee, S. B. MnO2/Poly(3,4-ethylenedioxythiophene) coaxial nanowires by one-step coelectrodeposition for electrochemical energy storage. *Journal of the American Chemical Society* **2008**, *130*, 2942-2943.
8. Whittingham, M. S. Lithium batteries and cathode materials. *Chemical Reviews* **2004**, *104*, 4271-4301.
9. Wang, Y. Cao, G. Z. Developments in nanostructured cathode materials for high-performance lithium-ion batteries. *Advanced Materials* **2008**, *20*, 2251-2269.
10. George, S. M. Atomic Layer Deposition: An Overview. *Chemical Reviews* **2010**, *110*, 111-131.
11. Suntola, T. Atomic Layer Epitaxy. *Thin Solid Films* **1992**, *216*, 84-89.
12. Leskela, M. Ritala, M. Atomic layer deposition (ALD): from precursors to thin film structures. *Thin Solid Films* **2002**, *409*, 138-146.
13. Gordon, R. G. Review of recent progress in atomic layer deposition (ALD) of materials for micro- and nano-electronics. *Abstracts of Papers of the American Chemical Society* **2004**, *227*, U553-U554.
14. Cleveland, E. R.;Banerjee, P.;Perez, I.;Lee, S. B.Rubloff, G. W. Profile Evolution for Conformal Atomic Layer Deposition over Nanotopography. *Acs Nano* **2010**, *4*, 4637-4644.
15. George, S. M. Atomic Layer Deposition: An Overview. *Chem. Rev.* **2010**, *110*, 111-131.
16. Miikkulainen, V.;Leskela, M.;Ritala, M.Puurunen, R. L. Crystallinity of inorganic films grown by atomic layer deposition: Overview and general trends. *Journal of Applied Physics* **2013**, *113*,
17. Poodt, P.;Cameron, D. C.;Dickey, E.;George, S. M.;Kuznetsov, V.;Parsons, G. N.;Roozeboom, F.;Sundaram, G.Vermeer, A. Spatial atomic layer deposition: A route towards further industrialization of atomic layer deposition. *Journal of Vacuum Science & Technology A* **2012**, *30*,
18. Meng, X. B.;Yang, X. Q.Sun, X. L. Emerging Applications of Atomic Layer Deposition for Lithium-Ion Battery Studies. *Advanced Materials* **2012**, *24*, 3589-3615.
19. Jung, Y. S.;Cavanagh, A. S.;Dillon, A. C.;Groner, M. D.;George, S. M.Lee, S. H. Enhanced Stability of LiCoO2 Cathodes in Lithium-Ion Batteries Using Surface Modification by Atomic Layer Deposition. *Journal of The Electrochemical Society* **2010**, *157*, A75-A81.

20. Panda, S. K.;Yoon, Y.;Jung, H. S.;Yoon, W. S.Shin, H. Nanoscale size effect of titania (anatase) nanotubes with uniform wall thickness as high performance anode for lithium-ion secondary battery. *Journal of Power Sources* **2012**, *204*, 162-167.
21. Cheah, S. K.;Perre, E.;Rooth, M.;Fondell, M.;Harsta, A.;Nyholm, L.;Boman, M.;Gustafsson, T.;Lu, J.;Simon, P.Edstrom, K. Self-Supported Three-Dimensional Nanoelectrodes for Microbattery Applications. *Nano Letters* **2009**, *9*, 3230-3233.
22. Gerasopoulos, K.;Chen, X. L.;Culver, J.;Wang, C. S.Ghodssi, R. Self-assembled Ni/TiO2 nanocomposite anodes synthesized via electroless plating and atomic layer deposition on biological scaffolds. *Chemical Communications* **2010**, *46*, 7349-7351.
23. Li, X. F.;Meng, X. B.;Liu, J.;Geng, D. S.;Zhang, Y.;Banis, M. N.;Li, Y. L.;Yang, J. L.;Li, R. Y.;Sun, X. L.;Cai, M.Verbrugge, M. W. Tin Oxide with Controlled Morphology and Crystallinity by Atomic Layer Deposition onto Graphene Nanosheets for Enhanced Lithium Storage. *Advanced Functional Materials* **2012**, *22*, 1647-1654.
24. Donders, M. E.;Knoops, H. C. M.;Kessels, W. M. M.Notten, P. H. L. Co3O4 as anode material for thin film micro-batteries prepared by remote plasma atomic layer deposition. *Journal of Power Sources* **2012**, *203*, 72-77.
25. Armand, J.-M. Tarascon and M. Issues and challenges facing rechargeable lithium batteries. *Nature* **2001**, *414*, 359-367.
26. J. S. Braithwaite, C. R. A. Catlow, J. D. Gale and J. H. Harding Lithium Intercalation into Vanadium Pentoxide: a Theoretical Study. *Chem. Mater.* **1999**, *11*, 1990-1998.
27. Whittingham, M. Stanley;Song, Yanning;Lutta, Samuel;Zavalij, Peter Y.Chernova, Natasha A. Some transition metal (oxy)phosphates and vanadium oxides for lithium batteries. *Journal of Materials Chemistry* **2005**, *15*, 3362.
28. Candace K. Chan, Hailin Peng, Ray D. Twesten, Konrad Jarausch, Xiao Feng Zhang and Yi Cui Fast, Completely Reversible Li Insertion in Vanadium Pentoxide Nanoribbons. *Nano Letters* **2007**, *7*, 490-495.
29. Yu, Danmei;Chen, Changguo;Xie, Shuhong;Liu, Yanyi;Park, Kwangsuk;Zhou, Xiaoyuan;Zhang, Qifeng;Li, JiangyuCao, Guozhong Mesoporous vanadium pentoxide nanofibers with significantly enhanced Li-ion storage properties by electrospinning. *Energy & Environmental Science* **2011**, *4*, 858.
30. Yan, Jian;Sumboja, Afriyanti;Khoo, EugeneLee, Pooi See V2O5 Loaded on SnO2 Nanowires for High-Rate Li Ion Batteries. *Advanced Materials* **2011**, *23*, 746-750.
31. Liu, Jun;Xia, Hui;Xue, DongfengLi, Lu Double-Shelled Nanocapsules of V2O5-Based Composites as High-Performance Anode and Cathode Materials for Li Ion Batteries. *J. AM. CHEM. SOC.* **2009**, *131*, 12086-12087.
32. Seng, Kuok Hau;Liu, Jun;Guo, Zai Ping;Chen, Zhi Xin;Jia, DianzengLiu, Hua Kun Free-standing V2O5 electrode for flexible lithium ion batteries. *Electrochemistry Communications* **2011**, *13*, 383-386.
33. Parag Banerjee, Xinyi Chen, Keith Gregorczyk, Laurent Henn-Lecordier, and Gary W. Rubloff Mixed mode, ionic-electronic diode using atomic layer deposition of V_2O_5 and ZnO films *Journal of Materials Chemistry* **2011**, *DOI: 10.1039/c1jm12595h*,
34. Musschoot, J.;Deduytsche, D.;Poelman, H.;Haemers, J.;Van Meirhaeghe, R. L.;Van den Berghe, S.Detavernier, C. Comparison of Thermal and Plasma-Enhanced ALD/CVD of Vanadium Pentoxide. *Journal of The Electrochemical Society* **2009**, *156*, P122.
35. George, S.M. Atomic Layer Deposition: An Overview. *Chem. Rev.* **2010**, *110*, 111-131.
36. J. C. Badot, S. Ribes, E. B. Yousfi, V. Vivier, J. P. Pereira-Ramos, N. Baffier, and D. Lincotb Atomic Layer Epitaxy of Vanadium Oxide Thin Films and electrochemical

behavior in presence of lithium ions. *Electrochemical and Solid State Letters* **2000**, *3*, 485-488.

37. Chen, X. Y.;Pomerantseva, E.;Banerjee, P.;Gregorczyk, K.;Ghodssi, R.Rubloff, G. Ozone-Based Atomic Layer Deposition of Crystalline V2O5 Films for High Performance Electrochemical Energy Storage. *Chemistry of Materials* **2012**, *24*, 1255-1261.
38. S. D. Elliott, G. Scarel, C. Wiemer, and M. Fanciulli Ozone-Based Atomic Layer Deposition of Alumina from TMA: Growth, Morphology, and Reaction Mechanism. *Chem. Mater.* **2006**, *18*, 3764-3773.
39. D. Goldstein, J. McCormick, S. George Al2O3 Atomic Layer Deposition with Trimethylaluminum and Ozone Studied by in Situ Transmission FTIR Spectroscopy and Quadrupole Mass Spectrometry. **2008**, *112*,
40. Heil, S. B. S.;Kudlacek, P.;Langereis, E.;Engeln, R.;van de Sanden, M. C. M.Kessels, W. M. M. In situ reaction mechanism studies of plasma-assisted atomic layer deposition of Al[sub 2]O[sub 3]. *Applied Physics Letters* **2006**, *89*, 131505.
41. Rose, Martin;Niinistö, Jaakko;Endler, Ingolf;Bartha, Johann W.;Kücher, PeterRitala, Mikko In Situ Reaction Mechanism Studies on Ozone-Based Atomic Layer Deposition of Al2O3and HfO2. *ACS Applied Materials & Interfaces* **2010**, *2*, 347-350.
42. Pomerantseva, E.;Gerasopoulos, K.;Chen, X. Y.;Rubloff, G.Ghodssi, R. Electrochemical performance of the nanostructured biotemplated V2O5 cathode for lithium-ion batteries. *Journal of Power Sources* **2012**, *206*, 282-287.
43. Whittingham, M. S.;Song, Y. N.;Lutta, S.;Zavalij, P. Y.Chernova, N. A. Some transition metal (oxy)phosphates and vanadium oxides for lithium batteries. *Journal of Materials Chemistry* **2005**, *15*, 3362-3379.
44. Navone, C.;Tintignac, S.;Pereira-Ramos, J. P.;Baddour-Hadjean, R.Salot, R. Electrochemical behaviour of sputtered c-V2O5 and LiCoO2 thin films for solid state lithium microbatteries. *Solid State Ionics* **2011**, *192*, 343-346.
45. Groult, H.;Le Van, K.;Mantoux, A.;Perrigaud, L.Doppelt, P. Study of the Li+ insertion into V2O5 films deposited by CVD onto various substrates. *Journal of Power Sources* **2007**, *174*, 312-320.
46. Andrukaitis, E. Lithium intercalation in electrodeposited vanadium oxide bronzes. *Journal of Power Sources* **2003**, *119*, 205-210.
47. Navone, C.;Baddour-Hadjean, R.;Pereira-Ramos, J. P.Salot, R. A kinetic study of electrochemical lithium insertion into oriented V2O5 thin films prepared by rf sputtering. *Electrochimica Acta* **2008**, *53*, 3329-3336.
48. Vivier, V.;Farcy, J.Pereira-Ramos, J. P. Electrochemical lithium insertion in sol-gel crystalline vanadium pentoxide thin films. *Electrochimica Acta* **1998**, *44,* 831-839.
49. Zhang, J. G.;McGraw, J. M.;Turner, J.Ginley, D. Charging capacity and cycling stability of VOx films prepared by pulsed laser deposition. *Journal of The Electrochemical Society* **1997**, *144*, 1630-1634.
50. Mantoux, A.;Groult, H.;Balnois, E.;Doppelt, P.Gueroudji, L. Vanadium oxide films synthesized by CVD and used as positive electrodes in secondary lithium batteries. *Journal of The Electrochemical Society* **2004**, *151*, A368-A373.
51. Kim, Y. T.;Gopukumar, S.;Kim, K. B.Cho, B. W. Performance of electrostatic spray-deposited vanadium pentoxide in lithium secondary cells. *Journal of Power Sources* **2003**, *117*, 110-117.
52. Kang, B. Ceder, G. Battery materials for ultrafast charging and discharging. *Nature* **2009**, *458*, 190-193.

53. Park, Y. J.;Ryu, K. S.;Kim, K. M.;Park, N. G.;Kang, M. G.Chang, S. H. Electrochemical properties of vanadium oxide thin film deposited by RF sputtering. *Solid State Ionics* **2002**, *154*, 229-235.
54. Liu, Y. Y.;Clark, M.;Zhang, Q. F.;Yu, D. M.;Liu, D. W.;Liu, J.Cao, G. Z. V2O5 Nano-Electrodes with High Power and Energy Densities for Thin Film Li-Ion Batteries. *Advanced Energy Materials* **2011**, *1*, 194-202.
55. Le Van, K.;Groult, H.;Mantoux, A.;Perrigaud, L.;Lantelme, F.;Lindstrom, R.;Badour-Hadjean, R.;Zanna, S.Lincot, D. Amorphous vanadium oxide films synthesised by ALCVD for lithium rechargeable batteries. *Journal of Power Sources* **2006**, *160*, 592-601.
56. Delmas, C.;Cognacauradou, H.;Cocciantelli, J. M.;Menetrier, M.Doumerc, J. P. The Lixv2o5 System - an Overview of the Structure Modifications Induced by the Lithium Intercalation. *Solid State Ionics* **1994**, *69*, 257-264.
57. McDowell, M. T.;Lee, S. W.;Ryu, I.;Wu, H.;Nix, W. D.;Choi, J. W.Cui, Y. Novel Size and Surface Oxide Effects in Silicon Nanowires as Lithium Battery Anodes. *Nano Letters* **2011**, *11*, 4018-4025.
58. McGraw, J. M.;Bahn, C. S.;Parilla, P. A.;Perkins, J. D.;Readey, D. W.Ginley, D. S. Li ion diffusion measurements in V2O5 and Li(Co1-xAlx)O-2 thin-film battery cathodes. *Electrochimica Acta* **1999**, *45*, 187-196.
59. Chen, Xinyi;Zhu, Hongli;Chen, Yu-Chen;Shang, Yuanyuan;Cao, Anyuan;Hu, LiangbingRubloff, Gary W. MWCNT/V2O5 Core/Shell Sponge for High Areal Capacity and Power Density Li-Ion Cathodes. *ACS nano* **2012**, *6*, 7948-7955.
60. Mukherjee, Rahul;Krishnan, Rahul;Lu, Toh-MingKoratkar, Nikhil Nanostructured electrodes for high-power lithium ion batteries. *Nano Energy* **2012**, *1*, 518-533.
61. Chen, Z.; Qin, Y.; Weng, D.; Xiao, Q.; Peng, Y.; Wang, X.; Li, H.; Wei, F.; Lu, Y. Design and Synthesis of Hierarchical Nanowire Composites for Electrochemical Energy Storage. *Adv. Funct. Mater*. **2009**, *19*, 3420-3426.
62. Seng, K. H.; Liu, J.; Guo, Z. P. Chen, Z. X.; Jia, D.; Liu, H. K. Free-standing V_2O_5 Electrode for Flexible Lithium Ion Batteries. *Electrochem. Commun.* **2011**, *13*, 383-386.
63. Sakamoto, J. S.; Dunn, B. Vanadium Oxide-Carbon Nanotube Composite Electrodes for Use in Secondary Lithium Batteries. *J. Electrochem. Soc.* **2002**, *149*, A26-30.
64. Sathiya, M.; Prakash, A. S.; Ramesha, K.; Tarascon, J. M.; Shukla, A. K. V_2O_5-anchored Carbon Nanotubes for Enhanced Electrochemical Energy Storage. *J. Am. Chem. Sco.* **2011**, *133*, 16291-16299.
65. D., Gui X.; Cao A.; Wei J.; Li H.; Jia Y'; Li Z.; Fan L.; Wang K.; Zhu H.; Wu Soft, Highly Conductive Nanotube Sponges and Composites with Controlled Compressibility. *ACS Nano* **2010**, *4,* 2320-2326.
66. Hu, L. Wu, H.; Gao, Y.; Cao, A.; Li, H.; McDough, J.; Xie, X.; Zhou, M.; Cui, Y. Silicon-Carbon Nanotube Coaxial Sponge as Li-ion Anodes with High Areal Capacity. *Adv. Energy Mater.* **2011**, *1*, 523-527.
67. Peng, Q.; Lewis, J. S.; Hoertz, P. G.; Glass, J. T.; Parsons, G. N. Atomic Layer Deposition for Electrochemical Energy Generation and Storage Systems. *J. Vac. Sci. Technol. A* **2012**, *30*, 010803.
68. Knoops, H. C. M.; Donders, M. E.; van de Sanden, M. C. M.; Notten, P. H. L.; Kessels, W. M. M. Atomic Layer Deposition for Nanostructured Li-ion Batteries. *J. Vac. Sci. Technol. A* **2012**, *30*, 010801.
69. Marichy, C.; Bechelany, M.; Pinna, N. Atomic Layer Deposition of Nanostructured Materials for Energy and Environmental Applications. *Adv. Mater.* **2012**, *24*, 1017-1032.

70. Das, R.K.; Liu, B; Reybolds, J.R.; Rinzler, A.G. Engineered Macroporosity in Single-wall Carbon Nanotube Films. *Nano Lett.* **2009**, *9*, 677-683.
71. Zadin, V.; Brandell, D.; Kasemägi, H.; Aabloo, A.; Thomas, J. O. Finite Element Modelling of Ion Transport in the Electrolyte of A 3D-microbattery. *Solid State Ionics* **2011**, *192*, 279-283.
72. Meng, X.; Ionescu, M.; Banis, M. N.; Zhong, Y.; Liu, H.; Zhang, Y.; Sun, S.; Li, R.; Sun, X. Heterostructural Coaxial Nanotubes of CNT@Fe_2O_3 via Atomic Layer Deposition: Effects of Surface Functionalization and Nitrogen-doping. *J. Nanopart. Res.* **2010**, *13*, 1207-1218.
73. Farmer, D. B.; Gordon, R. G. Atomic Layer Deposition on Suspended Single-walled Carbon Naotubes via Gas-phase Noncovalent Functionalization. *Nano Lett.* **2006**, *6*, 699-703.
74. Chen, X.; Pomerantseva, E.; Banerjee, P.; Gregorczyk, K.; Ghodssi, R.; Rubloff, G. Ozone-based Atomic Layer Deposition of Crystalline V_2O_5 Films for High Performance Electrochemical Energy Storage. *Chem. Mater.* **2012**, *24*, 1255-1261.
75. Perez, I.; Robertson, E.; Banerjee, P.; Henn-Lecordier, L.; Son, S. J.; Lee, S. B.; Rubloff, G. W. TEM-based Metrology for HfO_2 Layers and Nanotubes Formed in Anodic Aluminum Oxide Nanopore Structures. *Small* **2008**, *4*, 1223-1232.
76. Banerjee, P.; Chen, X.; Gregorczyk, K.; Henn-Lecordier, L.; Rubloff, G. W. Mixed Mode, Ionic-electronic Diode Using Atomic Layer Deposition of V_2O_5 and ZnO Films. *J. Mater. Chem.* **2011**, *21*, 15391-15397.
77. Elam, J.W.; Routkevitch, D.; Mardilovich, P.P.; George, S.M. Conformal Coating on Ultrahigh-aspect-ratio Nanopores of Anodic Alumina by Atomic Layer Deposition. *Chem. Mater.* **2003**, *15*, 3507-3517.
78. Whittingham, M. S.; Song, Y.; Lutta, S.; Zavalij, P. Y.; Chernova, N. A. Some Transition Metal (oxy)phosphates and Vanadium Oxides for Lithium Batteries. *J. Mater. Chem.* **2005**, *15*, 3362-3379.
79. Zhang, Z.; Dewan, C.; Kothari, S.; Mitra, S.; Teeters, D. Carbon Nanotube Synthesis, Characteristics, and Microbattery Applications. *Mater. Sci. Eng. B* **2005**, *116*, 363-368.
80. Golodnitsky, D.; Nathan, M.; Yufit, V.; Strauss, E.; Freedman, K.; Burstein, L.; Gladkich, A.; Peled, E. Progress in Three-dimensional (3D) Li-ion Microbatteries. *Solid State Ionics* **2006**, *177*, 2811-2819.
81. Le Van, K.; Groult, H.; Mantoux, A.; Perrigaud, L.; Lantelme, F.; Lindström, R.; Badour-Hadjean, R.; Zanna, S.; Lincot, D. Amorphous Vanadium Oxide Films Synthesised by ALCVD for Lithium Rechargeable Batteries. *J. Power Sources* **2006**, *160*, 592-601.
82. Nagasubramanian, G.; Doughty, D. H. Electrical Characterization of All-solid-state Thin Film Batteries. *J. Power Sources* **2004**, *136*, 395-400.
83. Oudenhoven, J. F. M.; Baggetto, L.; Notten, P. H. L. All-Solid-State Lithium-Ion Microbatteries: A Review of Various Three-Dimensional Concepts. *Adv. Energy Mater.* **2011**, *1*, 10-33.
84. Cheah, S. K.; Perre, E.; Rooth, M.; Fondell, M.; Harsta, A.; Nyholm, L.; Boman, M.; Gustafsson, T.; Lu, J.; Simon, P.; Edstrom, K. Self-Supported Three-Dimensional Nanoelectrodes for Microbattery Applications. *Nano Lett.* **2009**, *9*, 3230-3233.
85. Pomerantseva, E.; Gerasopoulos, K.; Chen, X.; Rubloff, G. W.; Ghodssi, R. Electrochemical Performance of the Nanostructured Biotemplated V_2O_5 Cathode for Lithium-ion Batteries. *J. Power Sources* **2012**, *206*, 282-287.
86. Yan, J.; Sumboja, A.; Khoo, E.; Lee, P. S. V_2O_5 Loaded on SnO_2 Nanowires for High-rate Li Ion Batteries. *Adv. Mater.* **2011**, *23*, 746-750.

87. Kang, B.; Ceder, G. Battery Materials for Ultrafast Charging and Discharging. *Nature* **2009**, *458*, 190-193.

88. Beninati, Sabina;Damen, LiberoMastragostino, Marina Fast sol–gel synthesis of LiFePO4/C for high power lithium-ion batteries for hybrid electric vehicle application. *J. Power Sources* **2009**, *194*, 1094-1098.

89. Carrilho, E.;Martinez, A. W.Whitesides, G. M. Understanding Wax Printing: A Simple Micropatterning Process for Paper-Based Microfluidics. *Anal. Chem.* **2009**, *81*, 7091-7095.

90. Martinez, A. W.;Phillips, S. T.Whitesides, G. M. Three-dimensional microfluidic devices fabricated in layered paper and tape. *P. Natl. Acad. Sci.* **2008**, *105*, 19606-19611.

91. Eder, F.;Klauk, H.;Halik, M.;Zschieschang, U.;Schmid, G.Dehm, C. Organic electronics on paper. *Appl. Phys. Lett.* **2004**, *84*, 2673-2675.

92. Martins, R.;Ferreira, I.Fortunato, E. Electronics with and on paper. *Phys. Status Solidi* **2011**, *5*, 332-335.

93. Tobjork, D. Osterbacka, R. Paper Electronics. *Adv. Mater.* **2011**, *23*, 1935-1961.

94. Cha, S. I.;Kim, Y.;Hwang, K. H.;Shin, Y. J.;Seo, S. H.Lee, D. Y. Dye-sensitized solar cells on glass paper: TCO-free highly bendable dye-sensitized solar cells inspired by the traditional Korean door structure. *Energy Environ. Sci.* **2012**, *5*, 6071-6075.

95. Fan, K.;Peng, T. Y.;Chen, J. N.;Zhang, X. H.Li, R. J. Low-cost, quasi-solid-state and TCO-free highly bendable dye-sensitized cells on paper substrate. *J Mater. Chem.* **2012**, *22*, 16121-16126.

96. Roy, S.;Bajpai, R.;Jena, A. K.;Kumar, P.;Kulshrestha, N.Misra, D. S. Plasma modified flexible bucky paper as an efficient counter electrode in dye sensitized solar cells. *Energy Environ. Sci.* **2012**, *5*, 7001-7006.

97. Wang, B. Kerr, L. L. Dye sensitized solar cells on paper substrates. *Sol. Energy Mater. Sol. Cells* **2011**, *95*, 2531-2535.

98. Barr, M. C.;Rowehl, J. A.;Lunt, R. R.;Xu, J. J.;Wang, A. N.;Boyce, C. M.;Im, S. G.;Bulovic, V.Gleason, K. K. Direct Monolithic Integration of Organic Photovoltaic Circuits on Unmodified Paper. *Adv. Mater.* **2011**, *23*, 3500-3505.

99. Hubler, A.;Trnovec, B.;Zillger, T.;Ali, M.;Wetzold, N.;Mingebach, M.;Wagenpfahl, A.;Deibel, C.Dyakonov, V. Printed Paper Photovoltaic Cells. *Adv. Energy Mater.* **2011**, *1*, 1018-1022.

100. Hu, L. B.;Choi, J. W.;Yang, Y.;Jeong, S.;La Mantia, F.;Cui, L. F.Cui, Y. Highly conductive paper for energy-storage devices. *P. Natl. Acad. Sci.* **2009**, *106*, 21490-21494.

101. Nyholm, L.;Nystrom, G.;Mihranyan, A.Stromme, M. Toward Flexible Polymer and Paper-Based Energy Storage Devices. *Adv. Mater.* **2011**, *23*, 3751-3769.

102. Pushparaj, V. L.;Shaijumon, M. M.;Kumar, A.;Murugesan, S.;Ci, L.;Vajtai, R.;Linhardt, R. J.;Nalamasu, O.Ajayan, P. M. Flexible energy storage devices based on nanocomposite paper. *P. Natl. Acad. Sci.* **2007**, *104*, 13574-13577.

103. Moon, R. J.;Martini, A.;Nairn, J.;Simonsen, J.Youngblood, J. Cellulose nanomaterials review: structure, properties and nanocomposites. *Chem. Soc. Rev.* **2011**, *40*, 3941-3994.

104. Polarz, S.;Smarsly, B.Schattka, J. H. Hierachical porous carbon structures from cellulose acetate fibers. *Chem. Mater.* **2002**, *14*, 2940-2945.

105. Fortunato, E.;Correia, N.;Barquinha, P.;Pereira, L.;Goncalves, G.Martins, R. High-performance flexible hybrid field-effect transistors based on cellulose fiber paper. *Ieee Electr. Device Lett.* **2008**, *29*, 988-990.

106. Souza, F. G.;Oliveira, G. E.;Anzai, T.;Richa, P.;Cosme, T.;Nele, M.;Rodrigues, C. H. M.;Soares, B. G.Pinto, J. C. A Sensor for Acid Concentration Based on Cellulose Paper Sheets Modified with Polyaniline Nanoparticles. *Macromol. Mater. Eng.* **2009**, *294*, 739-748.
107. Huang, Jia;Zhu, Hongli;Chen, Yuchen;Preston, Colin;Rohrbach, Kathleen;Cumings, JohnHu, Liangbing Highly Transparent and Flexible Nanopaper Transistors. *Acs Nano* **2013**,
108. Chun, S. J.;Choi, E. S.;Lee, E. H.;Kim, J. H.Lee, S. Y. Eco-friendly cellulose nanofiber paper-derived separator membranes featuring tunable nanoporous network channels for lithium-ion batteries. *J. Mater. Chem.* **2012**, *22*, 16618-16626.
109. Hu, L. B.;Wu, H.;La Mantia, F.;Yang, Y. A.Cui, Y. Thin, Flexible Secondary Li-Ion Paper Batteries. *Acs Nano* **2010**, *4*, 5843-5848.
110. Nystrom, G.;Razaq, A.;Stromme, M.;Nyholm, L.Mihranyan, A. Ultrafast All-Polymer Paper-Based Batteries. *Nano Lett.* **2009**, *9*, 3635-3639.
111. Jabbour, L.;Destro, M.;Gerbaldi, C.;Chaussy, D.;Penazzi, N.Beneventi, D. Aqueous processing of cellulose based paper-anodes for flexible Li-ion batteries. *J Mater. Chem.* **2012**, *22*, 3227-3233.
112. Rouquerol, J.;Avnir, D.;Fairbridge, C. W.;Everett, D. H.;Haynes, J. H.;Pernicone, N.;Ramsay, J. D. F.;Sing, K. S. W.Unger, K. K. Recommendations for the Characterization of Porous Solids. *Pure Appl. Chem.* **1994**, *66*, 1739-1758.
113. Chen, X. Y.;Pomerantseva, E.;Banerjee, P.;Gregorczyk, K.;Ghodssi, R.Rubloff, G. Ozone-Based Atomic Layer Deposition of Crystalline V2O5 Films for High Performance Electrochemical Energy Storage. *Chem. Mater.* **2012**, *24*, 1255-1261.
114. Liu, Y.;Zheng, H.;Liu, X. H.;Huang, S.;Zhu, T.;Wang, J. W.;Kushima, A.;Hudak, N. S.;Huang, X.;Zhang, S. L.;Mao, S. X.;Qian, X. F.;Li, J.Huang, J. Y. Lithiation-Induced Embrittlement of Multiwalled Carbon Nanotubes. *Acs Nano* **2011**, *5*, 7245-7253.
115. Whittingham, M. S.;Song, Y. N.;Lutta, S.;Zavalij, P. Y.Chernova, N. A. Some transition metal (oxy)phosphates and vanadium oxides for lithium batteries. *J. Mater. Chem.* **2005**, *15*, 3362-3379.
116. Sathiya, M.;Prakash, A. S.;Ramesha, K.;Tarascon, J. M.Shukla, A. K. V2O5-Anchored Carbon Nanotubes for Enhanced Electrochemical Energy Storage. *J. Am. Chem. Soc.* **2011**, *133*, 16291-16299.
117. Wang, S. Q.;Li, S. R.;Sun, Y.;Feng, X. Y.Chen, C. H. Three-dimensional porous V2O5 cathode with ultra high rate capability. *Energy Environ. Sci.* **2011**, *4*, 2854-2857.
118. Liu, Y. Y.;Clark, M.;Zhang, Q. F.;Yu, D. M.;Liu, D. W.;Liu, J.Cao, G. Z. V2O5 Nano-Electrodes with High Power and Energy Densities for Thin Film Li-Ion Batteries. *Adv. Energy Mater.* **2011**, *1*, 194-202.
119. Yan, J. A.;Sumboja, A.;Khoo, E.Lee, P. S. V2O5 Loaded on SnO2 Nanowires for High-Rate Li Ion Batteries. *Adv. Mater.* **2011**, *23*, 746-+.
120. McGraw, J. M.;Bahn, C. S.;Parilla, P. A.;Perkins, J. D.;Readey, D. W.Ginley, D. S. Li ion diffusion measurements in V2O5 and Li(Co1-xAlx)O-2 thin-film battery cathodes. *Electrochim. Acta* **1999**, *45*, 187-196.
121. Zadin, V.;Brandell, D.;Kasemagi, H.;Aabloo, A.Thomas, J. O. Finite element modelling of ion transport in the electrolyte of a 3D-microbattery. *Solid State Ionics* **2011**, *192*, 279-283.
122. Das, R. N.;Liu, B.;Reynolds, J. R.Rinzler, A. G. Engineered Macroporosity in Single-Wall Carbon Nanotube Films. *Nano Lett.* **2009**, *9*, 677-683.

123. Chae, W. S.;Van Gough, D.;Ham, S. K.;Robinson, D. B.Braun, P. V. Effect of Ordered Intermediate Porosity on Ion Transport in Hierarchically Nanoporous Electrodes. *Acs Appl. Mater. Interfaces* **2012**, *4*, 3973-3979.
124. Choi, B. G.;Yang, M.;Hong, W. H.;Choi, J. W.Huh, Y. S. 3D Macroporous Graphene Frameworks for Supercapacitors with High Energy and Power Densities. *Acs Nano* **2012**, *6*, 4020-4028.
125. Dendooven, J.;Goris, B.;Devloo-Casier, K.;Levrau, E.;Biermans, E.;Baklanov, M. R.;Ludwig, K. F.;Van der Voort, P.;Bals, S.Detavernier, C. Tuning the Pore Size of Ink-Bottle Mesopores by Atomic Layer Deposition. *Chem. Mater.* **2012**, *24*, 1992-1994.
126. Detavernier, C.;Dendooven, J.;Sree, S. P.;Ludwig, K. F.Martens, J. A. Tailoring nanoporous materials by atomic layer deposition. *Chem. Soc. Rev.* **2011**, *40*, 5242-5253.
127. Li, F. B.;Li, L.;Liao, X. Z.Wang, Y. Precise pore size tuning and surface modifications of polymeric membranes using the atomic layer deposition technique. *J Membrane Sci.* **2011**, *385*, 1-9.
128. Poinern, G. E. J.;Ali, N.Fawcett, D. Progress in Nano-Engineered Anodic Aluminum Oxide Membrane Development. *Materials* **2011**, *4*, 487-526.
129. Haspert, L. C.;Lee, S. B.Rubloff, G. W. Nanoengineering Strategies for Metal-Insulator-Metal Electrostatic Nanocapacitors. *Acs Nano* **2012**, *6*, 3528-3536.
130. Sherrill, S. A.;Duay, J.;Gui, Z.;Banerjee, P.;Rubloff, G. W.Lee, S. B. MnO2/TiN heterogeneous nanostructure design for electrochemical energy storage. *Physical Chemistry Chemical Physics* **2011**, *13*, 15221-15226.
131. Musschoot, J.;Xie, Q.;Deduytsche, D.;Van den Berghe, S.;Van Meirhaeghe, R. L.Detavernier, C. Atomic layer deposition of titanium nitride from TDMAT precursor. *Microelectronic Engineering* **2009**, *86*, 72-77.
132. Kim, H. Atomic layer deposition of metal and nitride thin films: Current research efforts and applications for semiconductor device processing. *Journal of Vacuum Science & Technology B* **2003**, *21*, 2231-2261.
133. Gregorczyk, K.;Henn-Lecordier, L.;Gatineau, J.;Dussarrat, C.Rubloff, G. Atomic Layer Deposition of Ruthenium Using the Novel Precursor bis(2,6,6-trimethyl-cyclohexadienyl)ruthenium. *Chemistry of Materials* **2011**, *23*, 2650-2656.
134. Heinrich, B. Magnetic nanostructures. From physical principles to spintronics. *Canadian Journal of Physics* **2000**, *78*, 161-199.
135. Kwon, O. K.;Kim, J. H.;Park, H. S.Kang, S. W. Atomic layer deposition of ruthenium thin films for copper glue layer. *Journal of the Electrochemical Society* **2004**, *151*, G109-G112.
136. Kim, W. H.;Park, S. J.;Son, J. Y.Kim, H. Ru nanostructure fabrication using an anodic aluminum oxide nanotemplate and highly conformal Ru atomic layer deposition. *Nanotechnology* **2008**, *19*,
137. Kim, S. K.;Choi, G. J.;Lee, S. Y.;Seo, M.;Lee, S. W.;Han, J. H.;Ahn, H. S.;Han, S.Hwang, C. S. Al-doped TiO2 films with ultralow leakage currents for next generation DRAM capacitors. *Advanced Materials* **2008**, *20*, 1429.